Discovering the role of the antioxidant enzyme SOD1 in the progression of Kras- and Braf-driven lung cancers

Timea Papp

Department of Biology

McGill University, Montreal

March 2025

A thesis submitted to McGill University in partial fulfillment of the requirements of the degree of Masters of Science

Table of Contents

List of Figures and Tables

Contribution of Authors

I would like to thank Dr. David Dankort for advising experimental directions and providing editorial help in preparing my thesis.

The experimental work represented in this thesis was conducted entirely by myself (Timea Papp). The writing comprising this thesis is likewise entirely my own.

English Abstract

Lung cancer is the deadliest cancer, more so than breast, prostate, and colorectal cancers combined. Despite continued research efforts, the 5-year survival rate has stagnated for the past 2 decades, remaining below a dismal 20%.

Due to heightened metabolisms, cancer cells accumulate toxic waste products called reactive oxygen species (ROS) at supraphysiological levels. To counter this, they also upregulate expression of Superoxide dismutase (Sod1), an antioxidant enzyme capable of neutralizing ROS. Sod1 has also been implicated in broader oxidative stress signaling, nutrient sensing, and ribosome biogenesis. Despite the clear metabolic importance of Sod1, its role in lung cancer has yet to be fully established.

This role is investigated here using Genetically Engineered Mouse Models (GEMMs) with inducible KRAS or BRAF mutations, allowing comparison of tumor models with wild-type and ablated Sod1. Preliminary results using this model suggest that Sod1 may be a critical inhibitor of cancer, as its absence causes dramatic disease progression and lifespan reduction. Increases in both tumor count and burden were evident upon Sod1 loss in both oncogene models. Quantifying key markers of ROS-induced damage suggests that ROS levels are oncogene-dependent, with DNA oxidation and protein nitration reliably elevated in Sod1-null Kras tumors, but not in Sod1-null Braf tumors. Preliminary evidence of differential involvement of immune infiltrate between the Kras and Braf oncogene models suggests a possible avenue for future investigation.

French Abstract

Le cancer du poumon est le cancer le plus mortel, plus que les cancers du sein, de la prostate et colorectal réunis. Malgré les efforts continus de la recherche, le taux de survie de 5 ans d'une

victime du cancer du poumon a stagné au cours des deux dernières décennies, restant inférieur à 20%.

En raison de leur métabolisme accru, les cellules cancéreuses accumulent des déchets toxiques appelés “reactive oxygen species” (ROS) à des niveaux supraphysiologiques. Pour contrer ce phénomène, elles augmentent également l'expression de la Superoxyde dismutase 1 (Sod1), une enzyme antioxydante capable de neutraliser les ROS. La Sod1 a également été impliquée dans la signalisation du stress oxydatif, la détection des nutriments et la biogenèse des ribosomes. Malgré l'importance métabolique évidente de la Sod1, son rôle dans le cancer du poumon n'a pas encore été entièrement établi.

Ce rôle est étudié ici en utilisant des modèles de souris génétiquement modifiées (GEMM) avec des mutations KRAS ou BRAF inductibles, ce qui permet de comparer les modèles de tumeurs avec la Sod1 de type sauvage et ablaté. Les résultats préliminaires obtenus à l'aide de ce modèle suggèrent que la Sod1 pourrait être un inhibiteur essentiel du cancer, car son absence entraîne une progression spectaculaire de la maladie et une réduction de la durée de vie. La perte de la Sod1 dans les deux modèles d'oncogène a entraîné une augmentation du nombre de tumeurs et de la charge tumorale. La quantification des marqueurs clés des dommages induits par les ROS suggère que les niveaux de ROS dépendent de l'oncogène, l'oxydation de l'ADN et la nitration des protéines étant augmentées de manière fiable dans les tumeurs Kras sans Sod1, mais pas dans les tumeurs Braf sans Sod1. Des preuves préliminaires de l'implication différentielle de l'infiltrat immunitaire entre les modèles d'oncogènes Kras et Braf suggèrent une voie possible pour de futures recherches.

Acknowledgements

I would like to thank my supervisor David Dankort for his support over the duration of my Master's research. It was his enthusiastic welcome that first solidified my choice to join his lab, and it was his continued love for science and conversation that helped inspire the direction of this work. Whether it be a discussion of mouse backcrosses, Gibson cloning, stock market volatility, or the perplexing abundance of fruit always stocked in his office, I could always count on his sage advice. I would also like to thank the members of my Supervisory Committee, Dr. Nam Moon and Dr. Siegfried Hekimi, for their astute observations and valuable input.

To Mary and Maria, who have brought brightness and brevity to even the most endless of days, I am thoroughly grateful. I cannot imagine having spent these years, nor shared this office, with anyone else. Though we were surely one of the smaller groups this building had to offer, I truly believe we were luckier for it.

To my family, who somehow never left my side: we all knew when I came to McGill for my undergraduate years that I would be in Montreal for a while, but I would be surprised if anyone predicted it would be quite this long. I have been so grateful for your love and support, both near and far, and will forever cherish the time spent in my second and third homes. You were the opportunities of a lifetime, and if I were to do it all again, I would not change a single thing.

This writing is dedicated to ZD, who had the courage to take a chance on himself,
and made it possible for me to do the same.

Introduction

The realm of redox biology has long been one shrouded in mystery. Originally aggregated into a catchall group of toxic metabolic byproducts, reactive oxygen species (ROS) have since been recognized as critical actors in numerous signal transduction pathways. The revelation of this dual nature, a seemingly-paradoxical combination of damage and signaling, raised more questions than it answered. What are the key players in ROS creation? In detoxification? What feedback systems balance ROS production and elimination? Is this balance altered in disease states, and, if so, is the imbalance a cause or symptom of the underlying pathology?

The field of redox study has since begun to understand how healthy tissues tackle this issue. Numerous enzymes have been identified as ROS producers; some so-called 'professional' ROS creators generate redox bursts for signaling purposes, and additional enzymes generate ROS as a byproduct of some other core function. ROS detoxifiers, including Superoxide dismutase (SOD), Glutathione peroxidase (GPX), and Peroxiredoxin (PRX) family enzymes, have also been recognized as secondary signaling agents. Downregulation of these enzymes supports sustained ROS bursts, and upregulation supports acute detoxification. Of course, the use of reactive molecules like ROS for signaling purposes introduces a sort of homeostatic gamble; how much damage is to be tolerated before prioritizing detoxification?

It is not surprising that the answer to this question boils down to an unsatisfying "It depends". In most healthy tissues, absent intensive bouts of growth, ROS are maintained at basal levels that keep both damage and signaling low. In some pathological conditions—most notably, cancer—increased ROS levels are sustained to favor growth and division over cellular integrity. Responding to this revelation, the search for cancer treatments related to ROS regulation has become a burgeoning field in its own right (C. Zhang et al., 2021).

The first line of defense against superoxide, a ROS member produced during routine cellular respiration, is Superoxide dismutase 1 (Sod1): a metalloprotease that catalyzes the breakdown of superoxide into H_2O_2 and water. As superoxide is highly reactive, its detoxification is essential to avoid cellular damage. The H_2O_2 byproduct is also involved in many signaling processes, including key proliferative pathways. This places the Sod1 enzyme at a critical interface of ROS damage versus signaling, and implicates it specifically in cancer, a pathology characterized by both redox imbalance and hyperproliferation. This connection is borne out by the literature (Che et al., 2016; Eleutherio et al., 2021; Glasauer et al., 2014; X. Li et al., 2019; S. Liu et al., 2020a; Papa, Manfredi, et al., 2014; Reddi & Culotta, 2013; Somwar et al., 2011; X. Wang et al., 2021; Xu et al., 2022).

The goal of this research is to determine the role of Sod1 in non-small cell lung cancer (NSCLC), with a focus on activating mutations in the critical oncogenes Kras and Braf. Prior work has determined that the $Kras^{G12D}$ and $Braf^{V600E}$ mutations, both found in NSCLC, generate tumors that respond differently to Sod1 loss (Dutchak and Dankort, unpublished). This suggests the two oncogenes generate tumors with distinct redox profiles, and thus distinct patterns of ROS detoxification. As both oncogenes are involved in the shared MAPK/ERK pathway, such differences present an especially intriguing opportunity for study.

A more complete picture of the oncogene-Sod1 relationship is established via three levels of analysis. First, disease severity and progression are assessed using survival data in mouse models of $Kras^{G12D}$ and $Braf^{V600E}$-driven NSCLC. Second, the resulting tumors are analyzed via immunostaining to characterize the ROS landscape and other tumor metrics. Finally, tumor cells are cultured to assess an *in vitro* impact of Sod1 loss in the context of these models.

Critically, this work will remain within the parameters of oncogene activation and Sod1 ablation, without any additional mutations present. Previous research of the Kras-Sod1 interaction in NSCLC mouse models also involved ablation of p53, a potent tumor suppressor and ROS regulator mutated in almost half of LUAD (H. Li et al., 2023; X. Wang et al., 2021). p53 loss has two main effects: 1) dramatically accelerating tumor progression, and 2) facilitating the creation of cell lines, which are not viable *in vitro* without p53 deletion (Shai et al., 2015).

Given the well-established role of p53 in signaling oxidant reduction and responding to DNA damage, p53 ablation alongside Sod1 loss further compromises cells' ability to respond effectively to oxidative stress (T. Chen et al., 2024; B. Liu et al., 2008; Salmeen et al., 2010; Seo et al., 2002; Shi & Dansen, 2020; Watanabe et al., 2021). The role of p53 as a redox modulator in disease is also supported by the literature, with p53 significantly altering cellular responses to oxidative stress in Kras-driven cancers (Kealey et al., 2022). Investigating a model with p53 retention is thus the next step in providing a comprehensive understanding of how Sod1 participates in tumor initiation and progression.

Chapter 1: Literature Review

1.1 Reactive Oxygen Species

1.1.1 Aerobic biochemistry

Earth's early atmosphere was in many ways inhospitable to the vast panoply of life currently roaming the planet. Indeed, such an atmosphere could not support the multicellular variety now abundant for one key reason: a lack of oxygen. Though the oxygenation of the atmosphere made aerobic life possible, a novel variety of oxygen-containing reactive molecules presented a novel biological challenge. How could aerobes utilize oxygen for metabolism—to the point of complete dependence on oxygen for survival—while also preventing the toxic accumulation of reactive byproducts?

This evolutionary conflict has been brewing ever since. During the course of routine function and survival, cells generate and accumulate ROS as byproducts of foundational cellular processes. The term 'ROS' encompasses oxygen-containing molecules more reactive than O_2 (which, in technical parlance, is itself considered a radical due to its outermost electrons being both parallel spinning and unpaired) (Halliwell & Gutteridge, 2015). ROS thus include not only radicals such as superoxide ($O_2^{\bullet -}$), but also nonradical species like hydrogen peroxide (H_2O_2). Oxygen species such as water (H_2O), which are less reactive than O_2, are not ROS.

Radical ROS generation can occur in a number of ways. Non-radical, stable species can become radicals upon electron loss, electron acquisition, or an uneven covalent bond cleavage resulting in an unpaired electron. Such radical species are now inherently unstable, primed to reattain stability by donating an electron to—or stealing an electron from—a nearby atom. In this way, radicals propagate damage, inducing the formation of new radicals to return themselves to

more stable energetic states. ROS creation can be both enzymatic (e.g. mitochondrial respiration) and non-enzymatic (e.g. UV radiation, environmental pollution), with ROS behaving as both oxidants and reductants (Lobo et al., 2010). Whereas low levels of ROS are intrinsic to aerobic life, sustained ROS elevation can promote a state of oxidative stress, which must then be mitigated to avoid irreparable damage. Prolonged supraphysiological oxidative stress can overwhelm a cell's protective capacities, resulting in quiescence or apoptosis.

1.1.2 Dual Capabilities of ROS

If considering only the volatile and destructive nature of ROS, it is easy to assume that the optimal cellular state would be one of vanishingly low ROS. Perhaps unsurprisingly, this assumption oversimplifies the capabilities of ROS, omitting their critical roles in intracellular signal transduction (Finkel, 2011; Sundaresan et al., 1995; Woo et al., 2010).

Within this context, the reactivities—and thus toxicities—of different ROS become relevant. So-called 'primary ROS' are direct byproducts of cellular reactions, often involved in signaling and generally causing low levels of toxicity (e.g. H_2O_2). In contrast, 'secondary ROS' are formed when primary ROS react with each other or with transition metals. This forms strongly radical and highly toxic species that propagate uncontrolled damage and are no longer practical signaling agents (e.g. hydroxyl radical, peroxynitrite) (Wei et al., 2023). Though primary ROS are not intrinsically damaging, their persistence in high concentrations inevitably propagates secondary species, often to deleterious effect. A nuanced working model integrates both ROS identity and concentration: low levels of primary ROS stimulate cell proliferation and survival, moderate levels generate secondary ROS and prompt expression of stress-responsive genes, and high levels cause macromolecular damage including DNA mutagenesis, triggering senescence or apoptosis (Cairns et al., 2011).

Physiological ROS Signaling

The importance of ROS can be inferred by the existence of 'professional' ROS-generating enzyme families. For example, production of H_2O_2 by the NOX enzyme DUOX2 is required for the initial steps of thyroid hormone synthesis (Knaus, 2021). DUOX2 mutations resulting in impaired H_2O_2 production cause congenital hypothyroidism, an endocrine disease with symptoms including cognitive impairment and altered growth (Knaus, 2021; S. Liu et al., 2016).

Redox status is also critical for immune function, with cell internal ROS signaling being a critical effector for activation and differentiation of T cells, B cells, macrophages, and dendritic cells (Berman-Riu et al., 2024; Peng et al., 2021; Sheng et al., 2010; Shu et al., 2023; Yarosz & Chang, 2018; H. Zhang et al., 2019; Y. Zhang, Choksi, et al., 2013). For example, T cell receptor stimulation initiates mitochondrial superoxide production within 2-4 minutes. The resulting spike of H_2O_2 signaling aids in stimulating the MAPK pathway and encouraging proliferation of the activated T cell, bolstering the population primed for pathogen response (Gülow et al., 2024). ROS levels in the extracellular milieu can also modulate the enrichment of various effector T cell populations, with high ROS favoring Th2 cells and low ROS favoring Th1 and Th17 differentiation. This skewing of T cell populations generates a cytokine profile adapted to combatting the encountered pathogen, demonstrating the vital role of ROS in mediating the immune response (Valencia & Kochevar, 2008).

This assessment of signaling ROS, while by no means exhaustive, sheds light on how redox signaling in individual cells can go on to effect broader organismal processes.

Pathological ROS Signaling

Keeping in mind the complexity of the pro- and anti-oxidant landscape, a distinction may be drawn between ROS in normal cells versus in their transformed counterparts. In many ways,

dysregulation is a hallmark of cancer cells, with one standout feature being an increased tolerance for impaired redox signaling. Though classically intertwined with terms like 'stress', 'mutation', and 'toxicity', ROS also play a pivotal role in promoting the chronic inflammation and prolonged proliferation associated with cancer. ROS are involved in modulating HIF1α, NF-KB, and p53 signaling, and stimulating pro-inflammatory cytokine production (Aggarwal et al., 2019). ROS generated by tumor cells recruit immune cells, which generate and release additional ROS into the tumor microenvironment (TME). A positive feedback loop ensues, as ROS oxidize key members of mitogenic signaling pathways—including PTEN, PTP1B, and MAPK phosphatases—activating proliferative programs which generate more ROS.

TME remodeling is also affected by ROS, with RAC1-generated ROS being involved MMP-2 secretion, which promotes angiogenesis, wound repair, and inflammation to support tumor growth (Y. Wang et al., 2021). ROS have also been implicated in the epithelial-mesenchymal transition (EMT), with superoxide being required for restructuring the actin cytoskeleton for cell polarization and migration (Moldovan et al., 1999; Y. Wang et al., 2021). The astonishing survival of tumor cells experiencing intense redox imbalance suggests that oncogenic transformation may increase tolerance for elevated ROS, or—more fascinating still—that transformation may require ROS elevation.

1.1.3 Superoxide: A keystone of the ROS family

Superoxide generation in the cells of obligate aerobes is inevitable, as electrons leaking from the mitochondria combine with readily-available oxygen. Whereas other enzymatic sources of ROS might be situationally up- or down-regulated, a continual basal requirement for ATP results in persistent superoxide generation, which must be kept in balance to maintain homeostasis.

Superoxide breakdown occurs non-enzymatically at very low rates, with the vast majority of cellular superoxide detoxified by SOD enzymes which catalyze the simultaneous oxidation and reduction of superoxide (dismutation) to form H_2O_2 and molecular oxygen. Although H_2O_2 is less reactive than superoxide, it can itself react with superoxide to form the hydroxyl radical (OH•), an indiscriminate oxidant targeting a wide variety of proteins, lipids, and nucleic acids (de Almeida et al., 2022). In the presence of chloride, H_2O_2 can also be converted by myeloperoxidases into hypochlorous acid (HOCl), which toxifies the phagosomes of bactericidal immune cells (Bedard & Krause, 2007; de Almeida et al., 2022; Q. Jiang et al., 1997).

Acute and sustained superoxide imbalance can also cause systemic organismal pathology. For example, superoxide readily reacts with nitric oxide (NO), a reactive nitrogen specie (RNS) that promotes vasodilation to regulate blood pressure (Ahmad et al., 2018). This reaction has two main results: 1) generation of the strong oxidant and secondary ROS peroxynitrite (ONOO-), and 2) depressed NO levels. To balance this system, peroxynitrite must be detoxified to prevent damage, and NO levels must be replenished to maintain blood pressure. Dysregulated superoxide can result in sustained NO depletion, eventually causing systemic cardiovascular effects such as hypertension (Node et al., 1997; Rathaus & Bernheim, 2002).

1.1.4 Enzymatic sources of superoxide

Mitochondria

The most plentiful source of superoxide is mitochondrial respiration, where rogue electrons leak out of the electron transport chain (ETC) and interact with available oxygen (Zhao et al., 2019). This forms superoxide in both the intermembrane space and the mitochondrial matrix across the inner mitochondrial membrane (IMM) (Nolfi-Donegan et al., 2020).

Interestingly, the ROS generated by the mitochondria are also involved in maintaining mitochondrial membrane potential (MMP), the charge differential across the IMM that powers ATP synthesis. The relative stability or weakness of the MMP determines the magnitude of respiration-associated ROS production (Zorova et al., 2018). While MMP elevation supports rapid ATP generation, ROS production also increases exponentially, endangering both mitochondrial and cellular health (Zorova et al., 2018). In contrast, sustained MMP reduction impairs ATP generation, increasing the risk of a converse state of *reductive* stress (Ge et al., 2024).

A class of ROS-responsive elements called mitochondrial uncoupling proteins (UCPs) help maintain the ATP/ROS balance by modulating MMP. When MMP is chronically elevated, UCPs leak protons back into the mitochondrial matrix to reduce MMP and prevent ROS overproduction (Echtay et al., 2002). In a process dubbed 'mild uncoupling', these UCPs can be activated by both superoxide and 4-hydroxynonenal (4HNE), a product of superoxide-mediated lipid peroxidation (Skulachev, 1996). Thus, mitochondrial ROS buildup generates a negative feedback loop that lowers mitochondrial membrane potential and reduces ROS (Aguirre & Cadenas, 2010; Starkov, 1997).

The vast majority of mitochondrial superoxide in the intermembrane space is scavenged by Sod1; the resulting H_2O_2 diffuses out of the outer mitochondrial membrane and into the cytosol for signaling purposes (Fischer et al., 2011; Palma et al., 2020; Sturtz et al., 2001; Yu et al., 2024). The manganese-bound Sod2 (MnSod) is structurally distinct from Sod1, yet functions analogously to detoxify superoxide within the mitochondrial matrix. The breakdown of superoxide to diffusible H_2O_2 is critical in this compartment, as negatively-charged superoxide requires active ion transport to cross membranes (Palma et al., 2020). The matrix also harbors GPXs, PRXs, and catalases, which scavenge excess H_2O_2 (Nolfi-Donegan et al., 2020).

NADPH oxidases

ROS are also produced by the NADPH oxidase (NOX) family of electron-shuttling transmembrane enzymes first discovered in phagocytes. The primary function of NOX family members is the transfer of an electron from cytoplasmic NADPH to membrane-external oxygen, reducing it to superoxide (Bedard & Krause, 2007). Phagocytes utilize this system to prepare oxidant-filled intracellular granules. Upon bacterial insult, these fuse with the plasma membrane and release their cytotoxic components in a phenomenon termed 'respiratory burst' (Ambruso et al., 2004; Babior et al., 1973; Bedard & Krause, 2007; Hohn & Lehrer, 1975; Thomas, 2017). NOX family members are thus critical participants in immune function. Interestingly, such professional oxidants are not relegated to phagocytes alone, but generate signaling ROS ubiquitously in all tissues (Thomas, 2017).

Xanthine oxidoreductase

A third avenue of superoxide production is the action of xanthine oxidoreductase (XOR), an enzyme involved in purine metabolism by oxidizing hypoxanthine to xanthine, and xanthine to uric acid (Shibuya et al., 2021). XOR is expressed in two interconvertible forms, including a dehydrogenase (xanthine dehydrogenase, XDH) and oxidase (xanthine oxidase, XO) (Battelli et al., 2016; Berry & Hare, 2004). XO delivers electrons to diatomic oxygen, forming either superoxide or H_2O_2 depending on environmental pH, oxygen concentration, etc. XOR can also react with nitrites like nitric oxide, which competes with xanthine at its binding site to form reactive nitrogen species including peroxynitrite (Battelli et al., 2016). XOR gene expression is upregulated by a number of factors, including proinflammatory cytokines (e.g. IL-1, IL-6, TNFα), cortisol, and hypoxia, among others, furthering the inflammatory state (Berry & Hare, 2004; Gibbings et al., 2011; Wright et al., 2004). Indeed, targeting XOR for inhibition has been

suggested as a possible therapeutic for chronic inflammatory disorders of the lung, including COPD (Gibbings et al., 2011; Komaki et al., 2005).

Notably, XOR is also involved in the pathology of ischemia-reperfusion injury. ATP degradation during ischemia yields hypoxanthine; increased oxygen availability following reperfusion promotes its conversion to xanthine by XOR, generating superoxide as a byproduct (Cowled & Fitridge, 2011). These elevated concentrations of superoxide are responsible for some of the hallmarks of reperfusion injury, including OH-mediated peroxidation of membrane lipids, and heightened release of arachidonic acid, the precursor of proinflammatory eicosanoids including prostaglandins and leukotrienes (X. Liu et al., 2018). These eicosanoids can have varied effects, but generally cause vasoconstriction, increased blood pressure, and endothelial damage increasing the permeability of microvasculature (Ferrari & Andrade, 2015). Adverse systemic effects can include pulmonary edema and an increase in immune cells in the lungs (Cowled & Fitridge, 2011). Again, this example demonstrates the compounding effects of superoxide overproduction, which results in systemic impairment when insufficiently combatted.

1.1.5 Extracellular sources of ROS

It has long been understood that environmental factors play a role in cellular health, with more recent findings underscoring the environment as a relevant source of oxidative stressors. These environmental ROS sources include, but are not limited to, tobacco smoke, industrial waste and pollution, urban pollutants such as automobile emissions, xenobiotic agents such as bacteria, and dietary contributions to mitochondrial dysfunction (Miazek et al., 2022).

UV radiation

Solar ultraviolet radiation, in the forms of UVA, UVB, and UVC, is a critical source of high-energy excitation and ROS formation (Miazek et al., 2022). While moderate UV exposure is

beneficial (e.g. vitamin D synthesis via UVA and UVB exposure), excessive exposure can lead to sunburn, collagen breakdown leading to premature photoaging of the skin, and DNA damage including carcinogenic mutation (de Jager et al., 2017). UV radiation also effects ROS-processing enzymes, an interesting example being the UVB-dependent ROS production via catalase, an enzyme generally known for its antioxidant effects in the breakdown of H_2O_2 (Adderley et al., 2019; Heck et al., 2003). Chronic UV exposure can increase the activity of NOX family enzymes, with produce ROS that signal prostaglandin synthesis; the subsequent inflammation characterizes sunburns. This pathway also links environmental and enzymatic sources of ROS (Valencia & Kochevar, 2008).

Though direct effects are relegated to sun-exposed tissues, the inflammatory environment fostered by UV damage can cause a state of oxidative stress which can promote systemic inflammation mediated by cytokine and chemokine signaling (Ansary et al., 2021; Beak et al., 2004; Valencia & Kochevar, 2008).

Pollutants and cigarette smoke

Cigarette smoke, suspected for decades to be a prevalent carcinogen, is also a common source of ROS. With the tobacco plant itself composed of at least 4200 chemicals—including heavy metals and radioactive components—and up to 8700 chemical components found in tobacco smoke, cigarettes are a source of large numbers of volatile compounds (Rodgman & Perfetti, 2008). While ROS concentrations in tobacco itself are negligible, ROS, including superoxide, have been detected in post combustion aqueous extracts of cigarette tar (M.-F. Huang et al., 2005).

One potent example of a compound with biological impact is para-benzoquinone (pBQ), which is found in large quantities in mainstream cigarette smoke (Mitra & Mandal, 2018). pBQ is enzymatically reduced by a number of pathways (including NOX, XOR, etc.), generating a

transient radical that reacts readily with oxygen to produce superoxide, and regenerate pBQ (Siraki et al., 2004). pBQ has also been implicated in mitochondrial dysfunction (Henry & Wallace, 1995) via pathological alterations of MMP heightening superoxide production across the IMM (Siraki et al., 2004).

Ultra-processed diet

Ultra-processed foods (UPFs) comprised of simple sugars, taste-enhancing additives, and preservatives now make up over two-thirds of adolescents' diets, representing a veritable food revolution since as recently as 1980 (Bahrampour et al., 2022). These foods are simultaneously low in nutrients and high in calories, reducing their impact on satiety, and reinforcing paradoxical states of overconsumption and malnutrition (Bahrampour et al., 2022). Sustained UPF overconsumption can have systemic hormone-mediated metabolic effects that promote the continuation of such eating habits (Ludwig et al., 1999). Though the obesogenic consequences of the modern diet have been long apparent, it is becoming clearer that even those within a normal weight range—via sustained UPF intake—can experience the same metabolic imbalances as those who are obese (Martínez Leo et al., 2021). An astonishing 93% of US adults demonstrate some degree of metabolic syndrome, a pathological constellation of obesity, hypertension, insulin resistance, and chronic inflammation (Harlan et al., 2023; O'Hearn et al., 2022; Y. Zong et al., 2024).

Such metabolic effects are also cellularly evident. The composition of the gut microbiota, for instance, is intrinsically tied to dietary habits, with gut dysbiosis caused by—and a cause of—high ROS and dysregulated inflammatory responses (Frazier et al., 2011). Sustained elevation of blood glucose, often compounded by the insulin resistance typical of metabolic syndrome, can result in endothelial dysfunction and elevated intracellular glucose (Rodríguez et al., 2023). Ready

availability intracellular glucose can overwhelm the mitochondria, saturating—and inevitably slowing—their metabolic capabilities. This causes a concomitant reduction in ATP generation, and increase in mitochondrial ROS, a state termed 'mitochondrial dysfunction' (Coppola et al., 2023). Sustained increases in ROS can also damage mtDNA, contributing further to mitochondrial abnormalities and oxidative stress (Bhatti et al., 2017).

Mitochondrial dysfunction has also been implicated in a number of disease states, including polycystic ovary syndrome (PCOS). Even short-term (3 month) dietary intervention with the low-carbohydrate ketogenic diet can significantly improve mitochondrial function, reducing ROS generation, reestablishing hormone balance, restoring insulin sensitivity (Khalid et al., 2023) and improving fertility (Tsushima et al., 2024). Mitochondrial dysfunction and excessive ROS generation have also been linked to altered neuroplasticity and neurotransmitter homeostasis, connecting poor metabolic health to mood disorder syndromes such as depression (H. Chen et al., 2024). Pilot research has also suggested that a ketogenic diet may have both metabolic and psychiatric benefits in individuals with schizophrenia (Sethi et al., 2024). Case studies with such individuals have even linked a long-term ketogenic diet with complete remission of psychiatric symptoms, including cessation of antipsychotic medications (Sarnyai & Palmer, 2020). This suggests that the impact of ROS generation, even from seemingly-benign dietary sources, should not be overlooked.

Chemotherapy

Anticancer chemotherapies have been designed to exploit cytotoxic redox imbalances, with one major group of chemotherapeutic agents promoting cellular ROS production, and a second inhibiting antioxidant enzyme function (Kohan et al., 2020). These agents hyper-elevate ROS, pushing oxidant levels beyond the threshold for growth promotion, into the range commonly

resulting in cell death (Yang et al., 2018). Whereas healthy cells adapt well to heightened ROS, the hypermetabolism of transformed cells makes them particularly susceptible to exogenous ROS insults; as such, chemotherapeutics are able to provide selective anticancer effects, with limited comparative damage to healthy tissues (Marioli-Sapsakou & Kourti, 2021).

1.2 SOD1: detoxifier in chief

1.2.1 Sod1 Structure and Biochemical function

SODs are a family of metalloenzyme antioxidants with the capacity to detoxify superoxide via dismutation. One of the major SOD subtypes, comprising MnSODs and FeSODs, diverged from a single original prokaryotic gene; MnSOD is evident in all kingdoms of life, and FeSOD in chloroplasts and eubacteria. The second major form, Cu/ZnSOD, is encoded by a distinct gene, and has been described in both prokaryotes and eukaryotes (Lynch & Kuramitsu, 2000). *E. coli* express intracellular Mn-SodA and Fe-SodB, and extracellular Cu/Zn-SodC, which combats host-derived ROS (Broxton & Culotta, 2016). Relevant to human study are the cytoplasmic/nuclear/IMM Cu/ZnSOD (SOD1), the mitochondrial MnSOD (SOD2), and the extracellular Cu/ZnSOD (SOD3) (Zelko et al., 2002).

Of these three, the most prevalent is SOD1, which is encoded on the human chromosome 21 (mouse chromosome 16) (Eleutherio et al., 2021; Zelko et al., 2002). During the dismutation reaction, negatively-charged superoxide is attracted to the positively-charged catalytic core of SOD1; even long-range electrostatic attraction is sufficient to direct superoxide off the walls of the channel and into the active site itself, where it docks among the Cu^{2+} and Zn^{2+} ions (Getzoff et

al., 1983). Once superoxide is bound, alternating oxidation and reduction of the copper cations yields H_2O_2 and O_2 (Eleutherio et al., 2021).

SOD1 functions as a dimer, with each monomer binding to a copper and zinc ion (Bafana et al., 2011). This binding is very stable, allowing enzymatic function in both acidic and basic conditions (pH 5-9.5), and in harsh denaturing environments (e.g. 8-10M urea solutions, 10% SDS). The fully-metalated Sod1 dimer is also exceptionally thermostable, with a melting point of 85-95°C (Trist et al., 2021). This capacity to function even in extreme environments makes SOD1 a potent detoxifier even in the abnormal conditions of the TME, including hypoxia, low pH, and nutrient deprivation (Anderson & Simon, 2020; Cairns et al., 2011).

Beyond superoxide dismutation, Sod1 has also been implicated in ribosome biogenesis via regulation of pre-rRNA processing; this nucleolar function appears to be the main role of Sod1 in Kras-driven lung cancer cells, with nuclear-only expression sufficient to restore growth potential of mutants with abolished Sod1 expression ($Sod1^{-/-}$ genotype, or Sod1-null cells) (X. Wang et al., 2021). Despite being chiefly a cytoplasmic and nuclear protein, Sod1 is also exported extracellularly in a number of cell types (Gosset et al., 2022).

1.2.2 Sod1-Linked Diseases

Amyotrophic lateral sclerosis (ALS)

The most widely-studied Sod1-related human disease is amyotrophic lateral sclerosis, more commonly known by its acronym ALS (Berdyński et al., 2022). ALS is a degenerative disease, distinct from other muscle-weakening conditions in the involvement of both upper- and lower-motor neurons (Simon et al., 2014). Patients present with symptoms of muscle weakness or impaired motor function; progressive muscle atrophy eventually leads to respiratory paralysis and death (Benatar et al., 2024; Simon et al., 2014).

Patient data suggests that of over 40 genes implicated in ALS, *SOD1* is the most frequently mutated (SOD1-ALS). Mutated Sod1 protein has two major effects: 1) loss of enzymatic function impairs superoxide clearance, and 2) misfolded mutant monomers form insoluble aggregates, which then catalyze prion-like corruption of wild-type (WT) Sod1. The former creates a state of neuronal oxidative stress, which is then aggravated by the latter (Motataianu et al., 2022). This effect is exacerbated in neurons specifically, where Sod1 makes up an enormous 1-2% of total protein (Pardo et al., 1995).

SOD1-ALS tissues show increased oxidative damage, with markers such as protein nitration, lipid peroxidation, and guanine oxidation all elevated in patient serum (Park & Yang, 2021). Interestingly, however, some SOD1-ALS mutants retain WT or higher levels of functional SOD1 expression, while retaining the phenotype of progressive motor neuron degeneration, implicating SOD1 aggregates as the major cause of disease (Williamson & Cleveland, 1999).

Studies in murine cell lines find that cells export both SOD1-containing vesicles and unenclosed SOD1-aggregates, which naïve cells selectively import by via micropinocytosis. This is a reasonable mechanism by which mutant SOD1 spreads between cells, and thus throughout the organism (Cruz-Garcia et al., 2017; Grad et al., 2014). Though the mechanism by which they cause toxicity is unknown, SOD1 aggregates are of clear importance; $Sod1^{-/-}$ mice—despite completely lacking Sod1 expression—do not develop ALS, nor manifest any ALS-specific symptoms (Berdyński et al., 2022; Gosset et al., 2022).

Aging

Animal studies of aging, especially in mouse models, have implicated antioxidants as key protectors of both organismal health and lifespan. Though most resist categorizing aging as a disease, fully Sod1-null animals display signs of intense premature and pathological aging, making

them an interesting lens through which to investigate both cellular effects and potential phenotypic rescues.

These mice harbor high levels of oxidative damage and frequent DNA double strand breaks, as well as heightened expression of cellular senescence markers p16 and p21, suggesting premature cellular senescence and decreased regenerative capacity (Campisi & d'Adda di Fagagna, 2007; Y. Zhang et al., 2017). Tissues of young $Sod^{-/-}$ mice express pro-inflammatory cytokines (e.g. IL-6 and IL-1β) at levels approaching those of old WT Sod mice (Y. Zhang et al., 2017), recapitulating the systemic inflammatory state often associated with advanced age (Noblanc et al., 2020). Amazingly, dietary restriction in these same mice restores cytokine levels to match young WT counterparts (Y. Zhang et al., 2017), and extends lifespan to match WT controls (Y. Zhang, Ikeno, et al., 2013), suggesting again the importance of diet for oxidative balance at the organismal level (S. Jiang et al., 2021). $Sod^{-/-}$ mice also display accelerated muscle denervation, decreased β-cell volume leading to glucose intolerance, reduced fertility in both sexes, premature hair, bone, and hearing loss, skin thinning, and delayed and impaired wound healing (Iuchi et al., 2010; Keithley et al., 2005; Kostrominova, 2010; Matzuk et al., 1998; McFadden et al., 1999; Morikawa et al., 2013; Murakami et al., 2009; Muscogiuri et al., 2013; Selvaratnam & Robaire, 2016).

Cancer

Whereas Sod1 mutation or loss can be a causative agent of disease, the role of Sod1 in cancer is more complicated. The intersection of Sod1 and cancer lies in metabolic dysregulation, with the hastened amplification of oncogenic cells stressing systems involved in energy production, and generating overwhelming levels of ROS. This puts cancer in the same vein as metabolic disorders like obesity, diabetes, atherosclerosis, and other cardiovascular diseases characterized by redox

imbalance (Le Lay et al., 2014; Rani et al., 2016). Though increased ROS can induce malignancies via oncogenic mutation, high levels of ROS are also byproducts of cancerous growth. Indeed, increased ROS is integral to the three main signaling hallmarks of cancer: glycolytic shift, survival, and proliferation (Sullivan & Chandel, 2014). Attenuation of *in vitro* cancer cells (Glasauer et al., 2014) and reduction of *in vivo* tumor burden (X. Wang et al., 2021) has been associated with Sod1 inhibition or genetic knockout. Interestingly, $Sod^{-/-}$ alone is insufficient to drive oncogenesis (Che et al., 2016).

1.2.3 Sod1 regulation

Sod1 is constitutively expressed, allowing cells to cope with general sources of oxidative stress, but a number of ROS-creating stimuli (e.g. UV radiation) can increase its transcription. *Sod1* transcription can also increase in response to nitric oxide, hydrogen peroxide, arachidonic acid, and various exogenous chemicals (Zelko et al., 2002).

Nutrient signaling

One way of modulating ROS levels is by modulating Sod1, a method utilized by the mTORC1 signaling pathway which acts as a sensor of nutrient availability.

When nutrients are readily available, mTORC1 phosphorylates SOD1 at serine 39 (Tsang et al., 2018). This deposits a negative charge at the mouth of the positively charged catalytic site, inhibiting the entrance of superoxide and inactivating the enzyme's catalytic activity. Superoxide levels skyrocket, the redox signaling of which feeds into the Raf/MEK/ERK pathway (e.g. by inhibiting EGFR or PDGF dephosphorylation (Knebel et al., 1996)), amplifying proliferative signals and favoring growth (Hrycay & Bandiera, 2015; McCubrey et al., 2007). In healthy tissue, mTORC1 is inhibited once nutrients become scarce, releasing SOD1 from inhibition and detoxifying ROS (Tsang et al., 2018). In the case of tumors, abnormal mTORC signaling promotes

Sod1 inhibition, and therefore proliferation and metastasis, despite limited nutrient availability and high ROS levels (Cognet & Muir, 2024; Lobel et al., 2023; Vaziri-Gohar et al., 2022). This is likely one reason why Sod1 expression is increased in cancer cells.

Oxidative stress

Sod1 is also responsive to the Nrf2 pathway (Milani et al., 2011). Under conditions of oxidative stress, the transcription factor Nrf2 is released from inhibition and enters the nucleus. There, it binds to antioxidant response element (ARE) sequences, activating a number of genes involved in inflammatory reduction, cellular repair, and antioxidant defense, including catalase, glutathione peroxidases, and peroxiredoxins (Luchkova et al., 2024; Yu et al., 2024). Hyper-stimulation and constitutive activation of Nrf2 is common upon oncogenic transformation, including oncogenic Kras, Braf, and Myc (DeNicola et al., 2011), preventing apoptosis and bolstering proliferation. Mutations in Nrf2 inhibitor KEAP1 have been noted in up to 20% of lung adenocarcinoma (LUAD), leading to permanent Nrf2 activation (Friedmann Angeli & Meierjohann, 2021). Kras mutation has also been found to increase Nrf2 gene transcription, protecting tumors from oxidative stress and promoting chemoresistance (Tao et al., 2014).

1.3 Lung Cancer

Lung cancer, deadlier than breast, prostate, and colorectal cancers combined, is the number one cause of cancer-related death globally (Molina et al., 2008). Cases can be broken into two categories: small cell lung cancer (SCLC; 15% of cases) and non-small cell lung cancer (NSCLC; 85% of cases) (Leonetti et al., 2018). 60% of NSCLCs are lung adenocarcinomas (LUAD), of

which 75% can be attributed to mutation in the MAPK/ERK signal transduction pathway (henceforth, the MAPK pathway) (W. Wang et al., 2022).

The MAPK pathway transmits critical signals regulating cell growth and division (Braicu et al., 2019). Extracellular ligands (e.g. growth factors) bind to receptor tyrosine kinases (RTKs) spanning the cell membrane. Ligand-bound RTKs dimerize and autophosphorylate intracellular tyrosine residues. They can then bind growth factor receptor-binding protein 2 (Grb2) and Son of Sevenless 1 (SOS1), forming the RTK/Grb2/SOS1 complex. This concentrates SOS1—a nucleotide exchange factor—at the cell membrane, where it can activate membrane-associated Ras to Ras-GTP (Braicu et al., 2019; Guo et al., 2020).

Ras-GTP activates Raf, which activates MEK1/2, which activates ERK1/2 via phosphorylation. Phosphorylated ERK (pERK) translocates to the nucleus and activates transcription factors associated with growth-promoting alterations in gene expression (Lake et al., 2016). The pathway autoregulates via pERK-mediated inhibition of SOS, Raf, and MEK. Ras is also inactivated via stimulation of its intrinsic GTPase activity.

1.3.1 Disturbance of canonical pathways via constitutively-active mutation

$Kras^{G12D}$

Three Ras genes are responsible for the production of three main isoforms of the small GTPase: Kras (with splice variants Kras4A and Kras4B (Whitley et al., 2024)), Nras, and Hras (Hobbs et al., 2016). 27% of cancers harbor missense gain of function mutations in Ras genes, with Kras responsible for 86% of Ras-mutated cancer cases (Adderley et al., 2019), followed by Nras (11%) and Hras (4%) (Hobbs et al., 2016). Within Kras, 98% of oncogenic mutations are found at codons G12, G13, and Q61 (L. Huang et al., 2021), with characteristic alterations at those sites depending

on the cancer type. Patients with Kras-mutant lung cancers have lower overall survival than those with Kras-WT lung cancers (43% vs. 61% 2-year survival) (Osta et al., 2019; Xie et al., 2021).

The most frequently-mutated Kras codon in lung cancer is G12, with $Kras^{G12D}$ the most common mutation in Kras-mutant NSCLC (33%), specifically among never-smokers (46%) (Tang et al., 2024; Wahl et al., 2021). Recent data suggest that transcript abundance of both Kras4A and Kras4B is significantly increased in LUAD; Kras-mutant tumors show significantly increased expression of both Kras4A and Kras4B compared to LUAD with WT Kras (Whitley et al., 2024).

The $Kras^{G12D}$ protein retains its capacity for SOS1-mediated activation, but lacks its intrinsic GTPase activity, locking the protein in its active conformation. Kras oncogenic transformation stimulates not only the MAPK/ERK pathway, encouraging growth and division, but also PI3K/AKT, promoting survival (Glaviano et al., 2023). $Kras^{G12D}$ has also been associated with elevated tumor mutational burden and immune suppression (G. Gao et al., 2020).

$Braf^{V600E}$

RAF, a Ras-activated member of the MAPK/ERK signaling pathway, also has three isoforms (ARAF, BRAF, and CRAF), with BRAF being the most potent activator of MEK (Śmiech et al., 2020) and most commonly involved in oncogenesis (Desideri et al., 2015). Upon activation by RAS, RAF forms either homo- or hetero-dimers which allosterically activate each other (Desideri et al., 2015).

The $Braf^{V600E}$ mutation is responsible for conferring oncogenicity in approximately 90% of Braf mutated cancers (Leonetti et al., 2018). $Braf^{V600E}$ falls within the category of Class I Braf mutations, which allow Braf to function as a monomer (Class II mutants dimerize and signal independent of Ras activation; Class III mutants have low or undetectable kinase activity, but can

herterodimerize with cytosolic Craf to form active Ras-independent heterodimers) (Garnett et al., 2005; Sahin & Klostergaard, 2021; Śmiech et al., 2020).

The V600E mutation grants two novel properties to the BRAF protein: an approximately 500-fold increase in kinase activity, and an uncoupling from both Ras activation and dimerization (Leonetti et al., 2018). $Braf^{V600E}$ is responsible for over 50% of melanomas, the majority of thyroid cancers, about 10% of colorectal cancers, and 3-5% of NSCLC (Dankner et al., 2018). NSCLC patient population data suggests that $Braf^{V600E}$ mutations, more common with never-smokers, correlate with poorer prognoses than non-V600E mutations (Leonetti et al., 2018). In mouse models, $Braf^{V600E}$ mutation alone is sufficient to promote lung adenomas; adenocarcinomas become common with concomitant mutation of p53 or other tumor suppressor genes (Dankort et al., 2007).

Dual mutation in Kras and Braf

Despite the prevalence of MAPK pathway mutations in cancer, mutations in different members of the pathway appear to be mutually-exclusive. Whereas mutational combinations such as Kras/p53 may collaborate across pathways and enhance oncogenicity, mutations hyper-activating the same pathway can cause oncogenic stress and senescence induction (El Tekle et al., 2021). Whereas either $Kras^{G12D}$ or $Braf^{V600E}$ mutation alone is sufficient to drive tumor growth in mouse models, dual Kras/Braf mutation initiates fewer tumors than Braf mutation alone, suggesting a selective disadvantage to the dual mutation (Cisowski et al., 2016). While dual $Kras^{G12D}$/$Braf^{V600E}$ tumors have been noted *in vivo* (Cisowski et al., 2016), true dual mutant cell lines *in vitro* have severe growth defects. This suggests that double-mutant tumors may represent mosaic populations of single-mutant cells rather than true dual mutants. Immunostaining and cell culture experiments from similar dual-oncogene experiments support this conclusion (Unni et al., 2015).

Kras/EGFR in LUAD, Braf/Kras in colorectal adenocarcinoma (COAD), and Braf/Nras in skin cutaneous melanoma (SKCM, (Petti et al., 2006; Sensi et al., 2006)) also appear mutually-exclusive, suggesting bi-oncogenic mutation within the EGFR-Ras-Raf signaling pathway overwhelms downstream effectors (Unni et al., 2015). The effectiveness of MEK inhibitors in treating both Braf- and Kras-driven tumors is one of the pharmacological benefits conferred by this shared set of downstream effectors (Ji et al., 2007).

1.3.2 Tumor metabolic reprogramming, altered gene expression, and ROS

Impossible to overlook when contextualizing the role of ROS in cancer is the intense metabolic reprogramming of tumor cells. Small, newly-initiated tumors enjoy a comfortable environment with ample bloodflow providing both nutrients and oxygen via diffusion. As growth proceeds rapidly, accumulating ROS drive proliferation and survival pathways. Tumor cells also undergo a dramatic metabolic reprogramming, favoring glycolysis over oxidative phosphorylation (OXPHOS) for quick—but inefficient—ATP production ($C_6H_{12}O_6 + 2P_i + 2ADP + 2NAD^+ \rightarrow 2C_6H_3O_3 + 2H_2O + 2ATP + 2NADH$). This glycolytic shift is eponymously termed the Warburg effect (Warburg et al., 1927), and is thought to support elevated growth rates while also providing necessary metabolic intermediates for nucleic acid, protein, and lipid biosynthesis via the tricarboxylic acid (TCA) cycle.

The predictable result of this shift is dramatically increased glucose consumption, initiating nutrient competition between tumor cells and lymphocytes in the TME (García-Jiménez & Goding, 2019). Tumor cells prevail *in vitro*, reducing T-cell health and impairing their tumor-clearing function (Chang et al., 2015). Tumors also quickly outgrow oxygen-providing capabilities of existing vasculature and become hypoxic. Hypoxia triggers a suite of metabolic changes, many related to the stabilization and nuclear translocation of HIF1α. These include: 1) enhanced

transcription of glycolysis genes whose promoters contain hypoxia response elements (HREs) (Semenza, 2020), 2) downregulation of pyruvate dehydrogenase (PDH) preventing the conversion of pyruvate to acetyl coenzyme A (acetyl-CoA) and downregulating OXPHOS, 3) upregulation of LDH to convert pyruvate to lactate, which regenerates NAD+ for glycolysis (Z. Chen et al., 2023; Locasale & Cantley, 2011).

To combat intracellular acidification due to excess lactate, cells increase lactate export, thus acidifying the TME. This low-pH environment can alter the gene expression of recruited immune cells, biasing macrophage populations toward the pro-inflammatory M1 phenotype, and hampering anti-tumor immune responses by impairing T-cell activation (Zhou et al., 2022). Pro-inflammatory cytokines (e.g. TNF, PDGF, VEGF, IL-1, and IL-6) increase ROS production by activating NADPH oxidases (Yu et al., 2024). They also recruit additional immune cells, promoting not only chronic inflammation, but a persistent state of oxidative stress augmented by continual cellular damage (Yu et al., 2024).

HIF1α stabilization also increases VEGF expression. This promotes local angiogenesis to provide the oxygen necessary to support tumor growth (Bae et al., 2024; Zimna & Kurpisz, 2015). Though the resulting blood vessels are preferable to the avascular alternative, they are often dysfunctional, lacking the optimized construction of native vessels. The constant production of random vessel networks which fail to meet oxygen demand results in a persistent state of tissue remodeling, hypoxia, and oxidative stress (Hosonuma & Yoshimura, 2023; Noguera-Troise et al., 2006).

Mitochondrial importance

Though the Warburg effect stresses the upregulation of glycolysis for ATP generation in cancer cells, the continued importance of the mitochondria cannot be overlooked. Some cancers rely on

OXPHOS for ATP production, upregulating mitochondrial biogenesis (W.-X. Zong et al., 2016). Mitochondrial respiration is linked to not only metastatic potential, but the generation of intermediate metabolites necessary for macromolecule biosynthesis via the TCA cycle (Martínez-Reyes & Chandel, 2021). These intermediate metabolites, including acetyl-CoA, succinate, and fumarate, are themselves involved in ROS synthesis, indirectly promoting tumor growth (Martínez-Reyes & Chandel, 2020). The TCA cycle is also a source of NADH, the substrate for NOX family enzymes (Eniafe & Jiang, 2021).

Cancer-associated fibroblasts

ROS also directs the local tissue remodeling supporting tumor growth. Chronic oxidative stress promotes the differentiation of myofibroblasts, cancer-associated fibroblasts (CAFs) that promote an inflammatory state of wound healing (Weinberg et al., 2019). ROS signaling also affects the development of PDGF-β fibroblasts, which support cell cycle entry and enable EMT by increasing cell motility (Salmeen et al., 2010; Weinberg et al., 2019). CAFs can aid in immune evasion; ROS production reprograms monocytes to myeloid-derived suppressor cells, which suppress the proliferation of CD8+ T cells in NSCLC models (Xiang et al., 2020). As a group, CAFs contribute heavily to TME remodeling through deposition of collagen, secretion of pro-tumorigenic factors, and immune evasion (Xiang et al., 2020).

Tumor progression

Thus, tumor progression is thought to proceed as follows:

Oncogene activation initiates cell transformation and hyperproliferation. Increased ATP requirements demand high OXPHOS, generating ROS. As cells deplete local nutrients, they favor glycolysis for rapid ATP production and synthesis of intermediate metabolites. This abnormal metabolic program is aggravated further by acidity, hypoxia, and ROS production in the TME.

These conditions necessitate novel transcriptional profiles—including upregulation of detoxifiers like Sod1—to ensure tumor survival. Ironically, such protective mechanisms often promote prolonged states of oxidative stress, inflammation, tissue remodeling, and immune evasion, which aggravate, rather than alleviate, disease severity.

1.3.3 Sod1 in LUAD

Current investigations of Sod1 in LUAD underscore its indispensable role in maintaining redox balance. Gene expression studies find that selective inhibition of Sod1 modifies the expression of over 80 genes. The MAPK, AKT, and p53 pathways are all affected (X. Li et al., 2019). *In vitro,* Sod1 knockdown prevents the growth of Kras mutant NSCLC cell lines and induces cell death (Che et al., 2016; Glasauer et al., 2014; Somwar et al., 2011).

Recent *in vivo* studies bolster these claims. A $Kras^{G12D}$; $p53^{-/-}$ NSCLC mouse model with an inducible Sod1 null allele ($Sod1^{Lox}$, or $Sod1^{L/L}$ when homozygous), elucidated that Sod1 loss is advantageous at early stages of tumor development, but eventually becomes detrimental, reducing tumor burden as compared to Sod1 WT mice. This also correlates with the stage of tumor development, with the growth of low grade adenomas heightened, and the growth of high grade adenocarcinomas reduced by Sod1 loss. Interestingly, levels of apoptosis and DNA damage did not significantly differ between $Sod1^{-/-}$ and $Sod1^{+/+}$ groups. (X. Wang et al., 2021)

Culturing tumor cells derived from the same mice ($Kras^{G12D}$; $Sod1^{L/L}$; $p53^{-/-}$; $CreER^{/+}$) demonstrates that Sod1 is indispensable for cell growth *in vitro*. Rather than enjoying a proliferative advantage, $Sod1^{L/L}$ cells (upon 4OHT activation of Cre expression) become quiescent. The results appear to recapitulate *in vivo* results from high grade adenocarcinomas, from which the cell lines were derived (X. Wang et al., 2021).

Chapter 2: Materials and Methods

2.1 Creation and collection of mouse samples

2.1.1 Mouse Strains

Mouse strains included four Cre-activated alleles: $Braf^{V600E}$ (B6.129P2(Cg)-*Braf*^{tm1Mmcm}/J), $Kras^{G12D}$ (B6.129S4-*Kras*^{tm4Tyj}/J), Sod1 deletion (Generated by D. Dankort), and p53 null (B6.129P2-*Trp53*^{tm1Brn}/J). All mice were maintained in a mixed C57BL/6 and FVB/N background.

Experimental mice harbored Braf or Kras Cre-inducible oncogenic alleles ($Braf^{CA}$ and $Kras^{LSL}$, respectively); upon Cre recombination, $Braf^{V600E}$ and $Kras^{G12D}$ oncogenic mutations are activated. Heterozygotes are designated $Braf^{CA/+}$ **(Figure 2.1a)** and $Kras^{LSL/+}$ **(Figure 2.1b)**, respectively. These strains were crossed to heterozygous mice harboring a Cre-inducible allele ablating Sod1 expression ($Sod1^{LoxP}$), producing both wild-type ($Sod1^{+/+}$) and homozygous mutant ($Sod1^{L/L}$) littermates **(Figure 2.1c)**. The Braf and Sod1 alleles both produce functional wild-type protein prior to Cre recombination, and can thus be maintained in a homozygous background. The $Kras^{LSL}$ allele is embryonic lethal when homozygous, as functional protein is only produced after Cre recombination; as such, it was maintained in a heterozygous background.

$Braf^{CA/+}$; $Sod1^{L/L}$ and $Kras^{LSL/+}$; $Sod1^{L/L}$ mice were also crossed with a Cre-inducible p53-null allele ($p53^{LoxP}$, $p53^{L/L}$ when homozygous) to generate $Braf^{CA/+}$; $Sod1^{L/L}$; $p53^{L/L}$ and $Kras^{LSL/+}$; $Sod1^{L/L}$; $p53^{L/L}$ tumors to provide cells viable for *in vitro* culture **(Figure 2.1d)**.

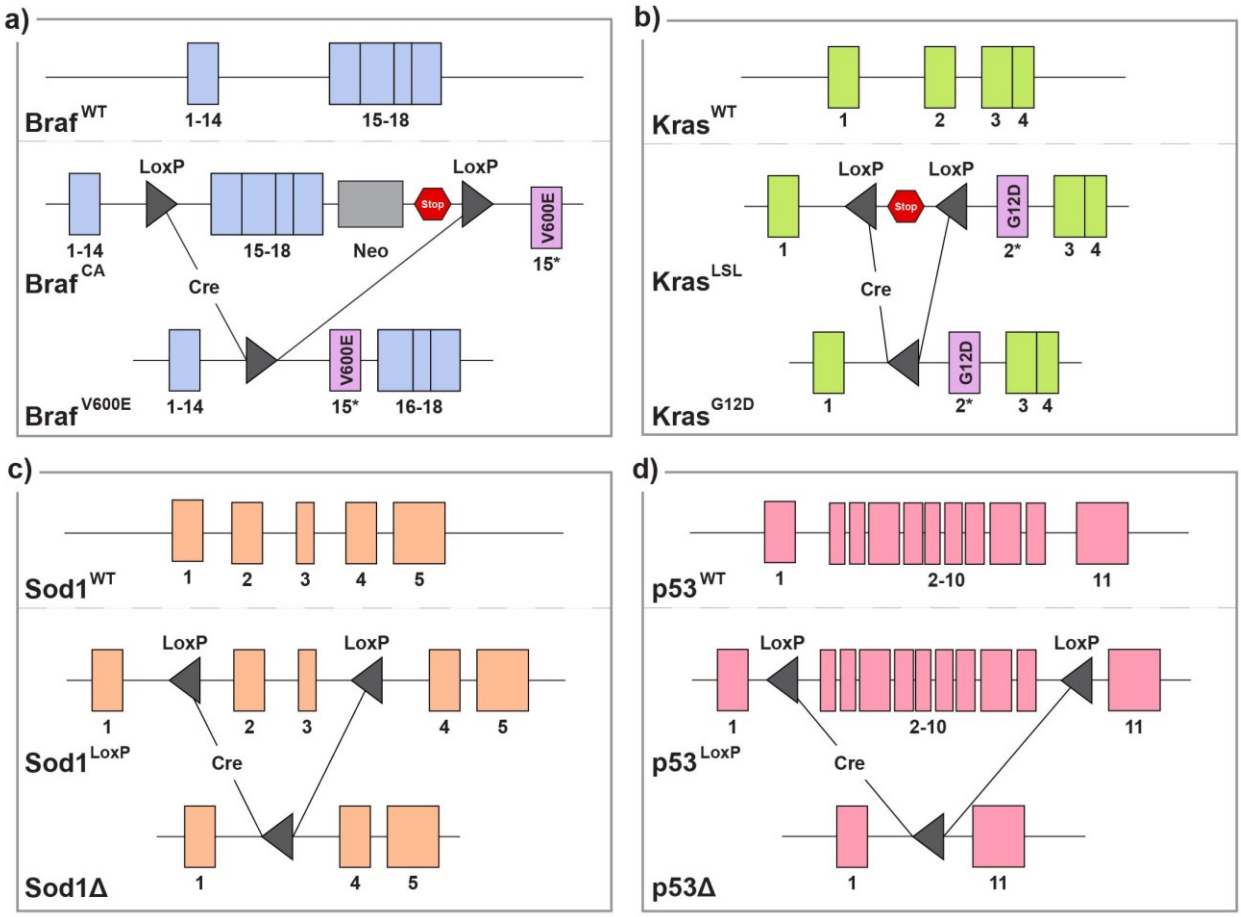

Figure 2.1- Diagram of allele constructs before and after Cre recombination

(a) Braf^{WT}, Braf^{CA}, and Braf^{V600E} allele constructs. Inserted into the endogenous Braf^{WT} locus is a construct containing 1) terminal exons 15-18 of the Braf gene and a neomycin stop cassette flanked by LoxP sites, and 2) mutated exon 15. This Braf^{CA} locus produces wild-type Braf at endogenous levels prior to recombination of the LoxP sites. Upon Cre recombination, Braf^{V600E} is expressed at endogenous levels. **(b)** Kras^{WT}, Kras^{LSL}, and Kras^{G12D} allele constructs. A so-called Lox-Stop-Lox (LSL) cassette, comprised of two LoxP sites flanking a transcriptional stop cassette, is inserted into the mutant Kras allele containing the well-characterized G12D substitution (Kras^{LSL}). Cre recombination removes the stop cassette, expressing Kras^{G12D} at endogenous levels. **(c)** The mutant Sod1^{LoxP} construct contains LoxP sites flanking exons 2-3. Prior to Cre recombination, the allele generates WT Sod1 at endogenous levels. Cre recombination excises exons 2-3, generating the Sod1Δ allele (Sod1-null or Sod1$^{-/-}$ when homozygous), and ablating Sod1 expression. **(d)** The mutant p53^{LoxP} construct contains LoxP sites flanking exons 2-10. Prior to Cre recombination, the allele generates functional p53 at endogenous levels. Cre recombination excises exons 2-10, ablating p53 expression and generating the p53Δ allele (p53-null or p53$^{-/-}$ when homozygous).

Mouse genotyping

Mouse tail tissue (~3mm length) was boiled in 75µL genotyping buffer (25mM NaOH, 0.2mM EDTA) for 30 minutes before being neutralized with an equal quantity of neutralization buffer (40mM Tris, pH 5.5) to expose DNA for polymerase chain reaction (PCR) genotyping (Truett et al., 2000). 35µL PCR reactions (120µM dNTPs, 400µM spermidine, 0.12µM forward and reverse primer mix, 0.2µL Taq DNA polymerase (FroggaBio, MB101-0500), and 1µL of tail DNA) were prepared (Thermocycler protocol is detailed in **Table 1**; primer sequences for mouse genotyping are specified in **Table 2**). PCR products were analyzed via gel electrophoresis; 2.5% 1:1 low-melt and standard agarose (BioShop, AGA101; FroggaBio, A87-500G) gel was prepared in 100mL TAE. Electrophoresis proceeded at 180V for 15-30 minutes, and the gel was imaged incrementally with the Axygen Gel Documentation System (Axygen, GDBL-1000) until distinct bands are apparent. Mixing primers facilitates detection of WT and Cre-activated alleles within the same lane of the gel, generating two bands per lane in heterozygous $Braf^{WT}/Braf^{CA}$, $Kras^{WT}/Kras^{LSL}$, $Sod1^{WT}/Sod1^{LoxP}$, and $p53^{WT}/p53^{LoxP}$ animals.

Adenoviral infection

Mice were infected at 8 weeks of age with $5x10^6$ PFU Cre-encoding adenovirus (AdCre, produced by D. Dankort, sourced from ViraQuest Inc.) prepared in a solution of Eagle's minimal essential medium (EMEM: Sigma-Aldrich, M0268-1L) and 40mM $CaCl_2$ (ACP, C0360-500G) to form a suspension of AdCre and calcium phosphate (CaPi) precipitate [4mM $CaCl_2$ used previously] (Fasbender et al., 1998). The mixture was flicked to combine and incubated at room temperature for 30 minutes. The precipitate was viable for intranasal administration for a further 90 minutes before significant decreases in efficiency.

Mice were anesthetized with 5% isoflurane in an oxygen-supplied induction chamber, and infected intranasally with 45µL of viral suspension while held in a prone position. Once the solution was inhaled, mice were monitored closely until recovered from anesthesia (1-2 minutes).

2.1.2 Lung tissue collection

Surgical anesthesia was induced in experimental mice via tribromoethanol (TBE, trade name Avertin®) administration. Powdered TBE (2,2,2-Tribromoethanol; Sigma-Aldrich, T48402-5G) was reconstituted in 10mL Tertiary amyl alcohol (Sigma-Aldrich, 152463-250ML); working TBE solution was prepared with 600µL of stock and 14.4mL Tris-EDTA diluent (Table 5), for a final concentration of 0.07M TBE. To anesthetize mice prior to surgery, 0.8-1.0mL of working TBE solution was administered via subcutaneous injection with a 1mL syringe and 26G needle (BD, 309659; BD, 305111).

Once anesthetized, mice were prepared for surgery by affixing the limbs to a Styrofoam board with surgical pins. A subcutaneous vertical incision up the ventral surface exposed the peritoneal wall, ribcage, and neck. The peritoneal muscle was removed to expose the diaphragm, to which the lungs were closely adhered. Once the diaphragm was punctured, the lungs shrunk away, allowing ribcage removal without damaging lung tissue. The heart was perfused with 10mL of 1x PBS (**Table 5**) via injection into the right ventricle. This flushed the pulmonary arteries, removing red blood cells that autoflouresce in immunofluorescence (IF) experiments. The heart was then removed. The neck fat pad was pulled away to uncover the neck muscles, which were torn back to reveal the trachea. The sternum was cut vertically to allow the removal of the trachea and lungs, which were easily disconnected from the thoracic viscera.

The lungs were perfused with 1x PBS through the trachea. Some large tumors were visible at this stage (**Figure 2.2a**, dashed line). The lungs were then likewise perfused with 10mL 10%

Neutral buffered formalin (VWR, 16004-126) and collected in a 50mL conical tube (FroggaBio, TB50-500) to be gently shaken overnight at 4°C. They were then processed in ethanol solutions of increasing concentrations (30%, 50%, 70% EtOH in ddH_2O) for 1hr each. Lung tissue underwent additional processing and was embedded in paraffin blocks at the Life Sciences Histology Core Facility (McGill University) to complete preparation of formalin-fixed, paraffin embedded (FFPE) samples. 5µm serial microtome sections were mounted on Superfrost Plus microscope slides (ThermoFisher, 22-037-246) and dried on a 37°C slide warmer overnight to improve tissue adherence.

Kaplan-Meier Survival curve analysis

Experimental endpoint data for each mouse was collected upon lung tissue retrieval. The number of days between AdCre infection and endpoint were noted; deaths unrelated to experimental endpoints were censored. Endpoint data was compiled in Excel and transferred to Prism to populate Kaplan-Meier survival curves. Survival curves were assessed via Log-rank analysis to generate appropriate P values.

2.2 Immunostaining and Analysis

2.2.1 Hematoxylin and Eosin staining

Hematoxylin and eosin (H&E) staining was accomplished with a regressive staining protocol performed by an automatic slide staining machine. FFPE sections were deparaffinized and rehydrated via three successive 2-minute washes in xylene (BioBasic, XC9800) and decreasing concentrations of ethanol (2 minutes each: three washes of 100% EtOH, two of 95% EtOH in ddH_2O, one of 70% EtOH, and two of ddH_2O). Slides were overstained (3 minutes) with 50%

hematoxylin (Fisher, 23-245678) before being rinsed in running water for 1 minute. Areas of nonspecific hematoxylin staining were eliminated via acid alcohol (1% HCl (ACP, H6100-500ML) in 70% EtOH; 1 minute), and the hematoxylin-stained nuclei were blued in Scott's tap water (0.04M $NaHCO_3$, 0.17M $MgSO_4$ in dH_2O; 1 minute) with rinses in running water between steps. Eosin staining was accomplished via 25% alcoholic eosin (Sigma, HT110180) diluted in 70% EtOH (45 seconds). Slides were then dehydrated with increasing concentrations of EtOH (2 minutes each: 95%, 100%, 100%) and three 2-minute washes of xylene, and coverslipped with Acrytol mounting medium (Leica, 3801720).

2.2.2 Immunohistochemical staining

Lung sections were deparaffinized and rehydrated with an automatic slide staining machine (as above). Antigen retrieval was performed in 10mM Sodium citrate buffer (pH6) (ACP, S2990-500g) for 10 minutes in a pressure cooker. Slides were arranged in a humidity chamber for incubation steps. Tissue sections were outlined with hydrophobic Pap Pen (Cedarlane MU12-A) and blocked in 2% BSA (BioShop, ALB001.250) in PBS for 30 minutes at room temperature. Primary antibody was diluted in 2% BSA in PBS (antibody dilutions found in **Table 3**) and the slides incubated overnight at 4°C followed by 1 hour at room temperature. Slides were then washed (2 minutes each: 1x PBS, 1x PBS-T, 1x PBS-T; Table 5) and blocked with 0.3% H_2O_2 (ACP, H7000) for 20 minutes. Secondary antibody was diluted 1:500 in 2% BSA in PBS and incubated for 45 minutes at room temperature. 15 minutes into the secondary incubation, the ABC complex reagents (Vector, PK-6100) were mixed in 5mL 1x PBS-T and incubated in the bottle for the remaining 30 minutes. Following secondary antibody incubation, slides were washed (2 minutes each: ddH2O, 1x PBS-T, 1x PBS-T) and incubated in ABC complex mix for 30 minutes at room temperature. Slides were washed again (2 minutes each: ddH2O, 1x PBS, 1x PBS).

The Biotium 20X DAB substrate kit (Biotium, 30015) was used to visualize immunostained regions. Immediately before use, one part 20X peroxide buffer and one part 20X DAB were mixed in eighteen parts 1x PBS to yield about 150µL per tissue section (the actual amount used varied based on the size of the tissue section). Slides were incubated in DAB mix for 15 minutes, after which the solution was washed off in dH_2O.

Slides were counterstained regressively with 50% Hematoxylin for 3 minutes, followed by acid alcohol and blueing steps, with alternating washes in running water (as above). Tissue sections were dehydrated in ethanol and xylene and coverslipped with acrytol (as above).

Immunohistochemistry image processing

FFPE samples were sectioned and IHC stained for ROS markers. Brightfield images were taken with the Leica DM4000 B microscope with identical exposure times (434.8µs) at 200X magnification. Raw brightfield images were imported into Photoshop and white balanced. White balancing based on a single pixel skewed the color temperature of the image; to avoid this, a small region of non-tissue 'white' pixels was selected and averaged, and this average color used to white balance the image *(Lasso select (non-tissue pixels) >> Filter >> Blur >> Average; Layer >> New Adjustment Layer >> Curves >> White point dropper (select within non-tissue pixels))*. As each image was subject to slight unavoidable variations in color temperature, the reference region of non-tissue 'white' pixels was selected manually for each image.

Composite images (merged panoramas of 50X zoom images) were created in Photoshop *(File >> Automate >> Photomerge)*. Each image was automatically imported into Photoshop as its own layer; these were then merged for simplicity *(with all layers selected: Layer >> Merge layers)*. The white balance was adjusted (as above). To determine the tumor count, each tumor was outlined *(Lasso select (individual tumor); Layer >> New >> Layer via Copy; With the new*

layer selected: Edit >> Stroke >> 7px, Inside, Opacity 60%). Once all tumors were outlined, the tumor layers are merged. The composite image with outlined tumors **(Figure 2.2b-i)** was imported into ImageJ for automated analyses of tumor count and area.

ImageJ tumor count, area, and percent tumor burden analyses

After all tumors were circled as above in Photoshop, a set of images were saved from each file and imported into ImageJ. For mice of $Sod1^{L/L}$ genotype, it became relevant to measure the areas of Sod1-null and Sod1-retaining 'escapee' tumors separately (Escapees, Sod1-retaining tumors within $Sod1^{L/L}$ lobes, are later discussed in detail). This was accomplished by creating two variant images, one with the Sod1-null tumors outlined, and the other with the escapee tumors outlined. Each of these images was processed as follows:

The lasso tool was used to outline the entire lobe section, which was copied to a new layer *(Layer >> New >> Layer via Copy)*. With this layer selected, a threshold was set to generate a black silhouette of the whole lobe *(Image >> Adjustments >> Threshold... >> Slider to 255)*. If the lobe did not appear completely black, this was corrected *(Filter >> Noise >> Dust and Scratches... >> Radius 10 pixels)*. Selecting the layer containing the tumors, the Green and Blue color channels under the Advanced Blending menu were deselected, isolating the Red channel. The tumors appear red, and the green outlines darker red. Other methods were also tested, but they often failed to recognize the boundaries of adjacent tumors, lowering tumor count and increasing tumor size. This method, however, could accurately distinguish tumors, even when tightly clustered.

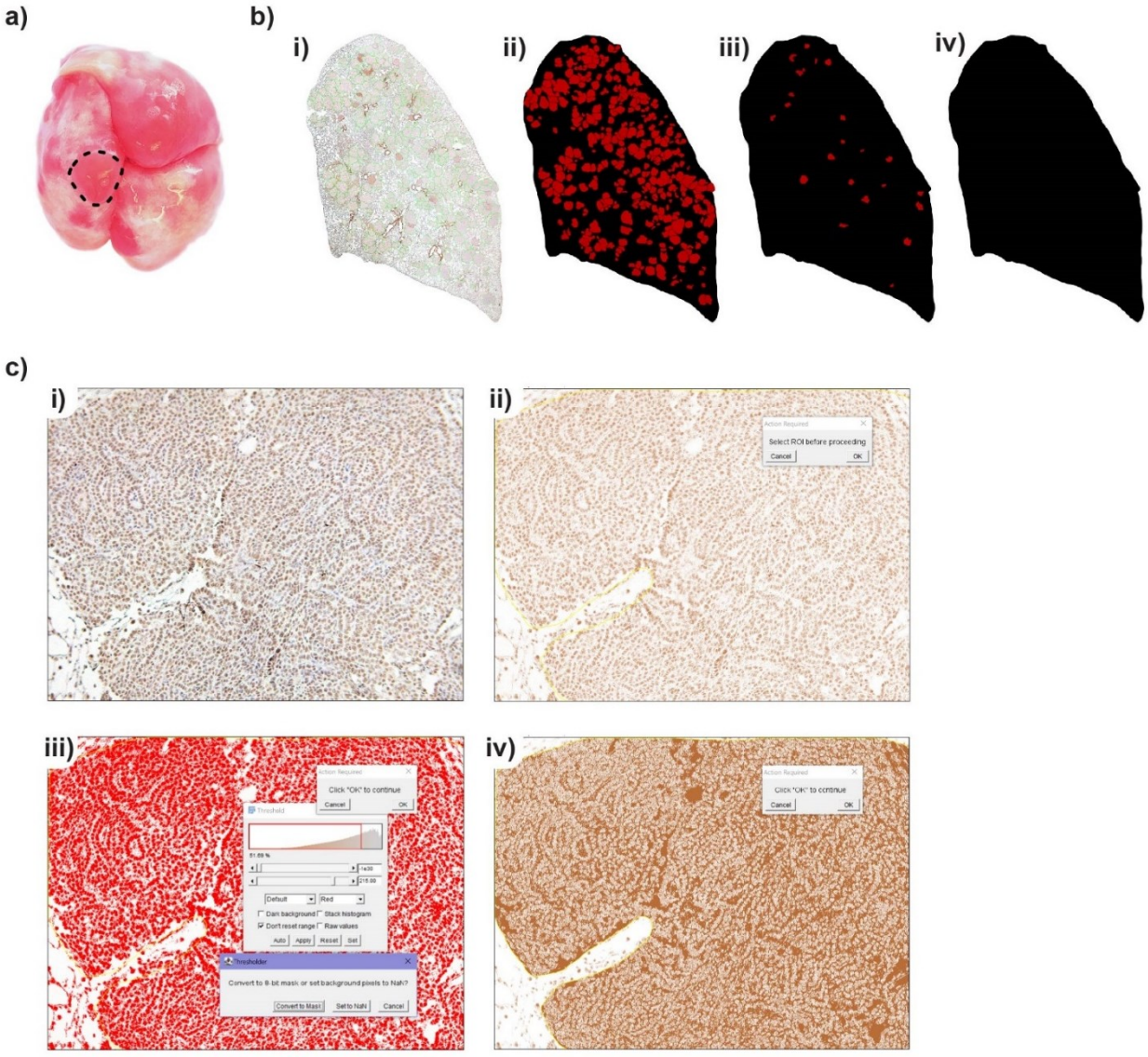

Figure 2.2- Representative ImageJ processing of immunohistochemistry image data

(a) Representative Braf$^{CA/+}$; Sod1$^{L/L}$ lung, freshly dissected and perfused with PBS to inflate. Visible tumor outlined with dashed line; printed roughly to scale. **(b)** Representative images of ImageJ processing to generate tumor count and area measures. *(i)* Tumors were individually circled in green in Photoshop; *(ii)* The lobe silhouette was generated, and the red channel of the Sod1-null tumor layer was isolated; *(iii)* Sod1 escapee tumor layers were merged and the red channel isolated; *(iv)* the lobe silhouette was saved individually. **(c)** Representative screenshots detailing ImageJ processing of IHC ROS marker positivity. *(i)* A tumor image was imported into ImageJ; *(ii)* The tumor was circled to generate an ROI; *(iii)* a threshold, limits [0, 215], was applied to the ROI and the background pixels set to 'NaN'; *(iv)* the remaining pixels were included in the final measurements.

With the red tumors and black lobe visible, the image was saved as a PNG file with a distinct name to be recognized in ImageJ automated processing **(Figure 2.2b-ii)**. The escapee tumor group was processed likewise, and saved as a new file **(Figure 2.2b-iii)**. The silhouette alone, with tumor layers hidden, was also processed and saved **(Figure 2.2b-iv)**.

Once all three files were saved, they were opened in ImageJ. A macro was run to produce one output measurement per image: 1) the area of each individual Sod1-null tumor, 2) the area of each individual escapee tumor, and 3) the area of the entire lobe. The macro recognized the bright red tumors, generated a clean binary image, and then measured the individual area of each tumor:

Image >> Adjust >>
Color Threshold [Hue 0-255, Saturation 255-255, Brightness 125-255]

Process >> Binary >> Convert to Mask; Process >> Binary >> Fill holes;
Process >> Noise >> Despeckle

Analyze >> Set Measurements >> Area

Analyze >> Analyze Particles [Size: 999-Infinity; Show: Outlines;
Display Results, Clear Results, Add to Manager]

The lobe image was processed similarly to yield its area in square pixels. Percent tumor burden was calculated for each lung section by dividing the sum of the tumor areas by the area of the lobe. Graphs were compiled in Prism, and two-tailed unpaired t-tests used for statistical analyses.

ImageJ analyses of ROS markers

FFPE samples, sectioned and IHC stained for ROS markers, were imaged at 200X magnification, white balanced in Photoshop, and imported into ImageJ (as above)**.** Relative positivity of ROS markers was analyzed via macro:

First, the hematoxylin and DAB stained image **(Figure 2.2c-i)** was parsed into three channels via the ImageJ plugin *Color Deconvolution2 (downloadable here; Image >> Color >> Color*

Deconvolution2). The second channel, containing the brown DAB stain, was retained for analysis **(Figure 2.2c-ii)**. The first channel, containing the hematoxylin stain, and the third channel, a byproduct of the deconvolution process, were both closed.

The DAB channel was converted to a 32-bit image to preserve pixel intensities *(Image >> Type >> 32-bit)*. The tumor was selected via the freehand selection tool, excluding areas of normal lung tissue or intense immune infiltrate to generate a region of interest (ROI). Measurement parameters were set to obtain the area of the selection and the mean grey value (MGV) of the stained pixels *(Analyze >> Set Measurements... >> [Area, Mean Gray Value, Standard deviation, Integrated density, Area fraction], Display label)*, and measurements taken *(Analyze >> Measure)*.

Next, a threshold was applied to the image to isolate only the DAB-stained pixels and eliminate non-tissue pixels *(Image >> Adjust >> Threshold... >> Bounds [0, 215])* **(Figure 2.2c-iii)**. The threshold bounds [0, 215] were selected to span the range of DAB staining and exclude non-tissue regions of the image with little to no stain. These threshold bounds were applied to all images, and the background pixels were converted to NaN ('Not a Number'; this excludes non-thresholded pixels in measures of image area and pixel intensity, **Figure 2.2c-iv**). Measurements were taken as before. This second area measurement should be smaller than the first, as the pixels outside the threshold bounds are now excluded. All images were processed likewise, and the measurements collected in an Excel file for further analysis.

In Excel, relative ROS positivity was computed with a simple formula including the area and relative darkness of the pixels in the threshold, and the area of the entire ROI (including pixels outside the threshold): $\frac{Area(Threshold)*[255-MGV(Threshold)]}{Area(Entire\ ROI)}$. Graphs were compiled in Prism, and two-tailed unpaired t-tests used for statistical analyses.

ImageJ analyses of ROS markers in escapee split images

An analogous process, including image collection, white balancing, color deconvoluting, threshold setting, measurement collection, and ROS intensity calculation was utilized for escapees in $Sod1^{L/L}$ lungs sections. Sod1 immunohistochemical staining revealed that both Sod1-null and escapee tumor regions could be visualized in a single 200X magnification image, referred to as 'split images'. Serial sections were then stained for ROS markers, and the same split images located and imaged. This analysis eliminates experimental variation, as both Sod1-positive and Sod1-null regions are side-by-side in the same region of the same slide.

To analyze ROS intensity across all markers, Sod1 staining was used to locate split images. Sod1-null and escapee ROIs were saved as unique selections in ImageJ, and area and MGV measurements taken for each. ROS markers were assessed by applying the same ROIs to each IHC image and taking the same measurements. For each split image, the intensity measurement of the Sod1-null ROI was normalized to that of the escapee, and results expressed as a percentage of marker positivity in Sod1-null regions.

2.2.3 Immunofluorescence staining

FFPE sections were deparaffinized and underwent antigens retrieval (as above). Tissue sections were then washed (2 minutes each: ddH_2O, 1x TBS, 1x TBS (**Table 5**)) and permeabilized in 0.5% TritonX-100 (BioShop, TRX777) for 15 minutes at room temperature. Blocking with 0.3M glycine (BioBasic, GB0235) proceeded for 20 minutes, followed by three 2-minute washes in 1x TBS. Slides then underwent a second blocking step, incubating in 2% BSA in PBS for 30 minutes. Primary antibody was diluted in 2% BSA in PBS (antibody dilutions listed in **Table 3**) and incubated on the slides overnight at 4°C.

Primary antibody was removed via three 2-minute washes in 1x TBS. Fluorophore-conjugated secondary antibody (Alexa Fluor® 555 AffiniPure™ Donkey Anti-Rabbit IgG (H+L); Jackson ImmunoResearch Inc, 711-565-152) was diluted 1:250, and DAPI (Sigma, D9542) 1:1000, in 2% BSA in PBS. This solution was applied to the slides and incubated for 90 minutes at room temperature. Slides underwent three 2-minute washes in 1x TBS, and coverslips were adhered with Prolong Gold Antifade reagent (Invitrogen, P36934); after 1 hour, clear nail polish was painted around the coverslip to secure. Slides were imaged within one week of staining to preserve maximal signal intensity.

Immunofluorescence image processing

Immunofluorescence images were taken with the Leica DM4000 B microscope at consistent exposure times for each fluorophore. The resulting images were processed in Photoshop to generate multicolored composites. The green channel from the DAPI image was isolated (nuclei are less clearly delineated in the blue channel), as was the red Sod1 channel (Alexa 555 secondary antibody). The DAPI signal was pseudocolored blue, and the Sod1 signal pseudocolored green for easy viewing. The two signal channels were then layered to generate a composite image.

2.3 *In vitro* Tumor cell culture and Analysis

2.3.1 BPSod and KPSod cell creation and collection

$Braf^{CA/+}$; $Sod1^{L/L}$; $p53^{L/L}$ (BPSod) and $Kras^{LSL/+}$; $Sod1^{L/L}$; $p53^{L/L}$ (KPSod) mice underwent AdCre infection at 8 weeks of age to initiate the development of Braf/Kras mutant, Sod1-null, p53-null tumors. Tumors grew for 10-12 weeks and lung tissue collected as earlier described, omitting the formalin treatment. The lungs were instead perfused with an enzyme mix (Miltenyi Biotec

Lung Dissociation Kit, 130-095-927) and incubated in a 5mL conical tube (Ultident, 48-C2545) for 30 minutes at 37°C, shaking. The tissue was roughly minced with surgical scissors and incubated for an additional 30 minutes. Clumps of tumor cells were dissociated further by pipetting up and down, and larger pieces of tissue removed by filtering through 70 and 40µm cell strainers (Fisher, 08-771-1; -2). The filtrate was centrifuged at 1500 RPM for 10 minutes, after which the enzyme mix was removed and the cell pellet resuspended in low serum DMEM (2% FBS (Gibco, 12483020), 1% penicillin/streptomycin (Wisent, 450-201 ZL), 100µg/mL kanamycin (BioBasic, KB0286)). Cells were plated in 10cm cell culture dishes (Fisher, 12-556-002). The cell culture media was changed two days later to low serum RPMI (Wisent, 350-000 CS) (2% FBS, 1% penicillin/streptomycin, 100µg/mL kanamycin) to promote the growth of epithelial cells **(Figure 2.3a)**. Differential trypsinization (Wisent, 325-045 EL) reduced fibroblast levels, while the more adherent epithelial cells remained. Once epithelial cells dominated the population, they were cultured in high serum DMEM (10% FBS) to promote rapid growth.

2.3.2 BPSod and KPSod cell line cloning

Cells were plated at a low concentration (~50-100 cells per 10cm dish) and grown until clonal colonies formed (10-14 days). Media was removed and replaced with PBS. 18-24 clonal colonies were collected with a P200 pipette and dispensed into a 24-well plate prepared with 50µL trypsin per well. The plate was incubated at 37°C for 5 minutes before media was added to neutralize the trypsin. Once clones grew to fill the well, they were plated to larger wells as necessary.

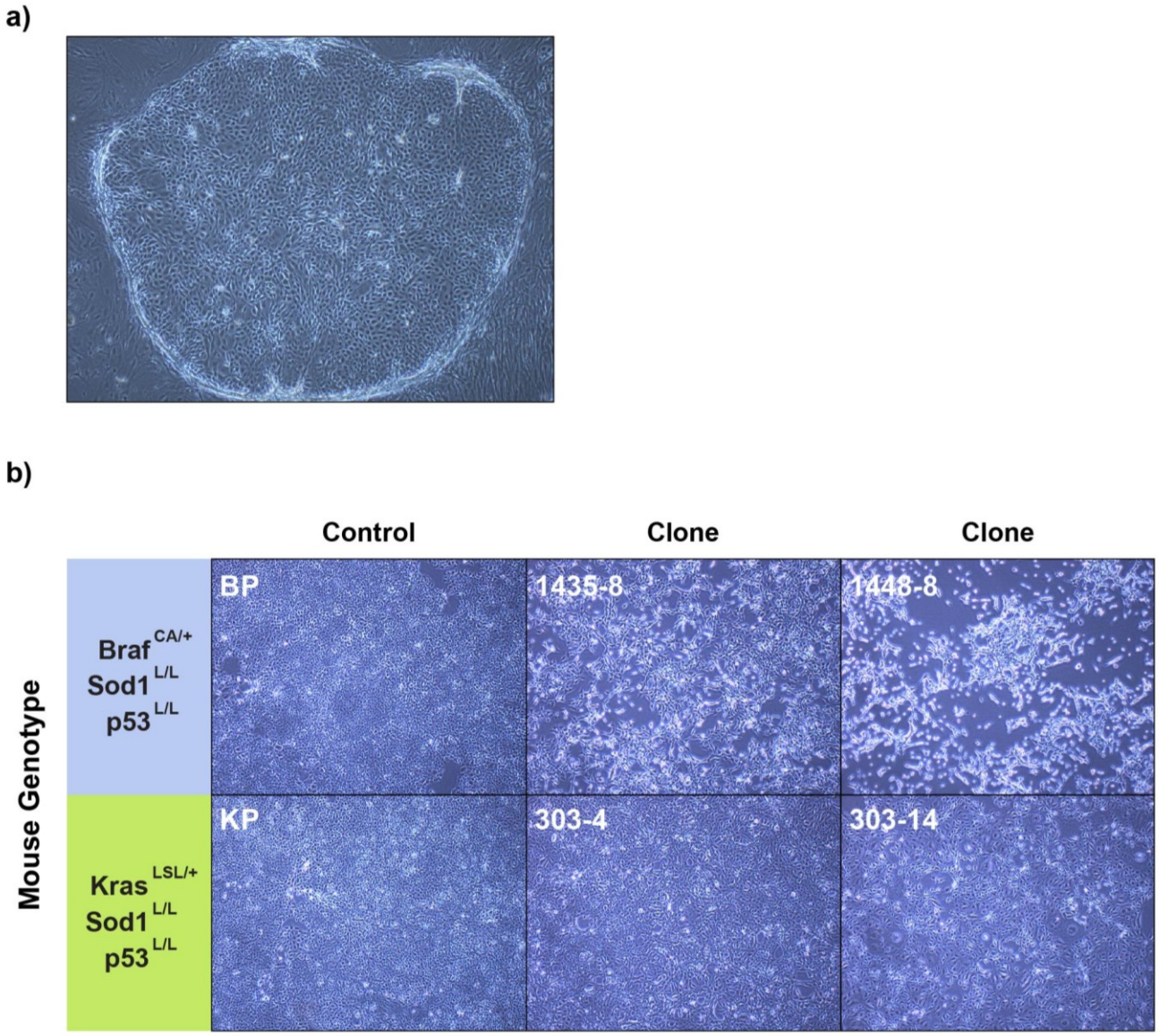

Figure 2.3- BPSod and KPSod Cell line creation and culturing

(a) Representative image of a colony of epithelial cells surrounded by non-epithelial cells. 40X magnification. (**b)** Control BP and KP cells and two clones per oncogene group. 40X magnification. Numerical designations for clones include both the mouse of origin and the clone used to generate the cell line.

Cell clone DNA isolation

Clones were cultured to confluence in a 10cm dish, trypsinized, washed with PBS and pelleted. They were boiled in 75µL genotyping buffer (25mM NaOH, 0.2mM EDTA) for 30 minutes before being neutralized with 75µL neutralization buffer (40mM Tris, pH 5.5) and centrifuged to re-pellet cell fragments (1500 RPM, 5 minutes). The DNA-containing supernatant was used for PCR genotyping. For genotyping the Cre-recombined $Kras^{LSL}$ allele, DNA was isolated with the Wizard Genomic DNA Purification Kit (Promega, A1120) to achieve clearer visualization of closely-spaced bands.

Cell clone PCR genotyping

18 BPSod and 18 KPSod clones were genotyped to confirm tumor origin. Genotyping proceeded as with mouse tail samples, with PCR genotyping performed as before for $Braf^{WT}/Braf^{CA}$, $Kras^{WT}/Kras^{LSL}$, $Sod1^{WT}/Sod1^{LoxP}$, and $p53^{WT}/p53^{LoxP}$ alleles, as well as Cre-recombined $Kras^{G12D}$, Sod1Δ, and p53Δ. Cre-recombined $Braf^{V600E}$ is also detected by the $Braf^{CA}$ primer, with the slightly higher upper DNA band reflecting the deletion of the floxed region. Primer sequences are specified in **Table 2** as primers used for cell genotyping. PCR samples were run on 2% agarose gels at 116V for 40-60 minutes, or until distinct bands were visible.

Four clones, two BPSod and two KPSod, with strong bands for the Sod1Δ allele were selected for further analyses. Cell lines were named numerically to specify the mouse of origin and the selected clone; the BPSod clones were designated 1435-8 and 1448-8, and the KPSod clones 303-4 and 303-14 to **(Figure 2.3b)**.

2.3.3 BPSod and KPSod cell growth curves

BPSod clones 1435-8 and 1448-8, KPSod clones 303-4 and 303-14, and BP/KP controls were plated at a density of $3x10^4$ cells per well (one well per clone) in five 6-well plates. One day post-

plating (D0), the wells of one plate were washed with PBS and incubated with zinc formalin fixative overnight. This was repeated on days 1, 3, 5, and 7 to generate a growth curve per cell line.

Once cells were fixed, the plates were washed thoroughly to remove any trace fixative and dried overnight in a biosafety cabinet supporting air circulation. The next day, the cells were incubated in a 0.1% crystal violet solution on a shaker at room temperature. After 30 minutes, the cells had absorbed the dye and the crystal violet solution was aspirated away. The plates were washed thoroughly in a water bath and dried again overnight.

The next day, the wells were incubated with 10% acetic acid, shaking, until all bound dye was eluted from the cells. To quantify dye, 100µL from each well was transferred to a 96-well plate in triplicate, using 10% acetic acid as a blank control. The plate was scanned in a 96-well plate reader to determine the optical density of each well at 590nm, a proxy for cell density. The blanks were averaged and subtracted from the experimental values. The triplicate sets were averaged to generate each datapoint, and the datapoints were plotted in Prism. Two-tailed unpaired t-tests were used for statistical analyses.

2.3.4 Cell lysis for Western Blotting

Cells were cultured in three 10cm dishes per clone (BPSod clones 1435-8 and 1448-8, KPSod clones 303-4 and 303-14, and BP/KP controls; total of 18 plates) until confluent. The cells were trypsinized, neutralized with 10% FBS DMEM, and pelleted via centrifugation (1500 RPM for 5 minutes). The pellets were washed in 1mL cold PBS and spun again to repellet. The pellet was resuspended in 200µL PLCγ lysis buffer **(Table 5)** and incubated at 4°C on an end-over-end rotator for 30 minutes. The lysate was centrifuged at 15000 RPM for 15 minutes to pellet cell fragments,

and the protein-laden supernatant was collected and transferred to clean microtubes for western blotting.

BCA assay to normalize protein concentration

Standards were prepared from dilutions of BSA in the same buffer used for cell lysis (PLCγ), generating a 7-concentration range from 50-4000 µg/mL. PLCγ lysis buffer was used as a blank.

Protein lysates were diluted 1:5 in lysis buffer to bring the protein concentration within detection range of the BCA assay. 10µL of each diluted cell lysate was combined with 90µL of Pierce BCA Protein Assay Kit reagent mix (Fisher, 23227) in a 96-well plate. All samples and standards were included in triplicate. The plate was incubated at 37°C for 30 minutes to develop the colorimetric assay, after which absorbance measurements were taken at 562nm in a plate reader. Triplicate values were averaged and compared to the standard measures to determine the protein concentration of each sample and calculate the dilution ratios required to normalize all samples to equivalent protein concentrations.

Cell lysate dilution and Western Blot sample preparation

All protein stocks were normalized to 0.5µg/µL total protein to load 10µg of protein per 20µL of sample loaded into the gel. Internal controls were generated by serially diluting this stock. The first 1:1 dilution with PLCγ lysis buffer generated a 5µg sample, which was then diluted 1:1, etc. until 4 dilutions were generated. To generate Western Blot samples, 3 parts lysate dilution and 1 part 4X Laemmli buffer **(Table 5)** were combined and boiled for 5 minutes at 100°C.

2.3.5 Western Blotting

Polyacrylamide gels were prepared by pouring a layer of 4% stacking gel over a 15% separating gel **(Table 5)** and inserting a 10-well comb. Gels polymerized at room temperature for

30 minutes. Each well was loaded with 20µL of sample while submerged in SDS running buffer **(Table 5)**. 5µL of BLUelf Prestained Protein Ladder (GeneDireX, PM008-0500) ran alongside samples to monitor protein migration (15µL 2x SDS loading buffer **(Table 5)** is included with each ladder to bring the total volume to 20µL). Electrophoresis proceeded at 80V until the dye front reached the separating gel, at which point voltage was increased to 150V and electrophoresis continued until the dye front ran off the bottom of the gel.

PVDF membranes (BoRad, 1620177) were activated in methanol for 1-5 minutes, then immersed in transfer buffer **(Table 5)**. Thick western blotting filter papers (BioRad, 1703932) were also soaked in transfer buffer. Each gel was assembled into a 'transfer sandwich', a stack of blotting paper, PVDF membrane, gel, and blotting paper, and arranged on a Trans-Blot SD Semi-Dry Transfer Cell (BioRad 1703848). Bubbles between layers were removed by compressing each sandwich with a roller, and protein bands were transferred to the PVDF membranes via semidry transfer (15V for 40 minutes). Following transfer, each membrane was cut just beneath the green protein marker (~25 kDa) to allow for separate antibody incubation: anti-Sod1 antibody on the lower portion (~16 kDa) and anti-α-tubulin antibody on the upper portion as a loading control (~55 kDa). The membranes were floated in 100% EtOH for 1 minute and rinsed in 1x TBS-T **(Table 5)** before being incubated in 5% milk in TBS-T for 1 hour at room temperature. They were then incubated with primary antibody diluted in 5% milk in TBS-T overnight at 4°C, shaking (antibody dilutions available in **Table 3**). Membranes were washed thrice in 1x TBS-T for 10 minutes each. HRP-conjugated secondary antibody was diluted 1:2,000 in TBS-T and incubated for 1 hour at room temperature; this antibody was removed via three final 2-minute washes in 1x TBS-T.

Membranes were incubated in ECL solution (Sigma, GERPN2209) for 2 minutes, and placed between sheets of plastic in an autoradiography cassette. 2-minute exposures were obtained using

western blotting film optimized for chemiluminescence (Diamed, DIAFILM810). Developed western blot films were digitized with a standard flatbed photo scanner. Scans were taken at 600 dpi and saved as TIFF files.

Western Blot Analysis

TIFF files of scanned western blots were imported into ImageJ. An ROI was created by enclosing the largest protein band with the rectangle tool and saving the selection *(File >> Save as >> Selection)*. Measurements were set to determine the MGV of each band *(Analyze >> Set Measurements... >> Mean Gray Value)* and measurements were taken by positioning the same ROI around each protein band *(Analyze >> Measure)*. 'Blank' measurements were also collected by positioning the ROI in an area of empty space either above or below each protein band. This generates 32 measurements per dilution set (4 Sod1 dilutions, 4 Sod1 blanks, 4 α-tubulin dilutions, and 4 α-tubulin blanks for the clone of interest). This process was repeated for each respective BP/KP control. Once all measurements are taken, values are transferred to an Excel file for analysis.

The values generated by ImageJ corresponded to the average darkness of each ROI (from 0-255), with lower values corresponding to darker ROIs, and higher values corresponding to lighter ROIs. To make the results more intuitive, this was inverted by subtracting each value from 255. The respective blanks were then subtracted from each band measurement to eliminate background signal. Final results were compiled by taking the ratio of Sod1 band intensity to tubulin band intensity for each dilution and averaging these values per gel. Graphs were compiled in Prism, and two-tailed unpaired t-tests used for statistical analyses.

Chapter 3: Results

3.1 Survival

Sod1 impacts survival in oncogenic Kras^{G12D}, but not Braf^{V600E}, tumor models

Given the importance of ROS balance in maintaining cell proliferation, the relationship of Sod1 to tumor growth and organismal health was of great interest. As such, *Sod1* deletion was paired with well-characterized Braf^{V600E} and Kras^{G12D} oncogenic mutations to investigate the effects of antioxidant loss on the resulting tumors.

Six genotypes of experimental mice were infected with AdCre at 8 weeks of age: Braf$^{CA/+}$; Sod1$^{+/+}$, Braf$^{CA/+}$; Sod1$^{L/+}$, Braf$^{CA/+}$; Sod1$^{L/L}$, Kras$^{LSL/+}$; Sod1$^{+/+}$, Kras$^{LSL/+}$; Sod1$^{L/+}$, and Kras$^{LSL/+}$; Sod1$^{L/L}$ genotypes. One cohort (Braf, n=25; Kras, n=15) was euthanized at 8 weeks post-infection, prior to the advent of adverse health effects, to ensure successful tumor initiation; H&E-stained sections of lung tissue confirmed that small tumors were already present **(Figure 3.1a, b)**. To observe more advanced disease progression, endpoints for the remaining experimental animals were based on significant signs of health deterioration, including rapid shallow breathing, poor body condition and weight loss, hunched posture, and diminished activity. Endpoint bodyweight approximated 16g for females, and 20g for males. Median endpoints ranged from 17-34 weeks post-infection across all four genotypes (17.0, 18.1, 30.6, and 22.0 weeks, respectively) **(Figure 3.1c)**.

Within the Braf group **(Figure 3.1d)**, median post-infection lifespans were 127.0 days, 139.5 days, and 119.0 days for Sod1$^{L/L}$, Sod1$^{L/+}$, and Sod1$^{+/+}$ groups, respectively. The survival curves revealed no significant difference between the Sod1$^{+/+}$ and Sod1$^{L/L}$ groups (mean difference of 6.3% [8 days], Log-rank curve analysis p=0.096); the Sod1$^{L/+}$ group did not differ significantly

from either group (p=0.12, p=0.80, respectively). Overall, this suggests that Sod1 expression status has no significant effect on post-infection lifespan in mice with Braf-driven lung tumors.

Within the Kras group **(Figure 3.1e)**, median post-infection lifespans were 168.0, 191.0, and 239.0 days for $Sod1^{L/L}$, $Sod1^{L/+}$, and $Sod1^{+/+}$ groups, respectively. Survival curve analyses revealed a significant difference in the survival of $Sod1^{+/+}$ versus $Sod1^{L/L}$ groups (mean difference of 29.7% [71 days], Log-rank curve analysis p=0.02), whereas neither differed significantly from the $Sod1^{L/+}$ group (p=0.08, p=0.66, respectively). Overall, Sod1 ablation correlated with significant lifespan reduction in mice with Kras-driven lung tumors.

Comparing the two oncogene groups, mice with Braf-initiated tumors died significantly sooner than those with Kras-initiated tumors. Nearly 100% of individuals with Braf-initiated tumors reached their endpoint around 200 days post-infection, whereas individuals with Kras-driven tumors require an additional 100+ days to produce such results. This disparity is a previously-noted byproduct of the allele constructs and method of tumor induction used in this experimental procedure (Dutchak and Dankort, unpublished).

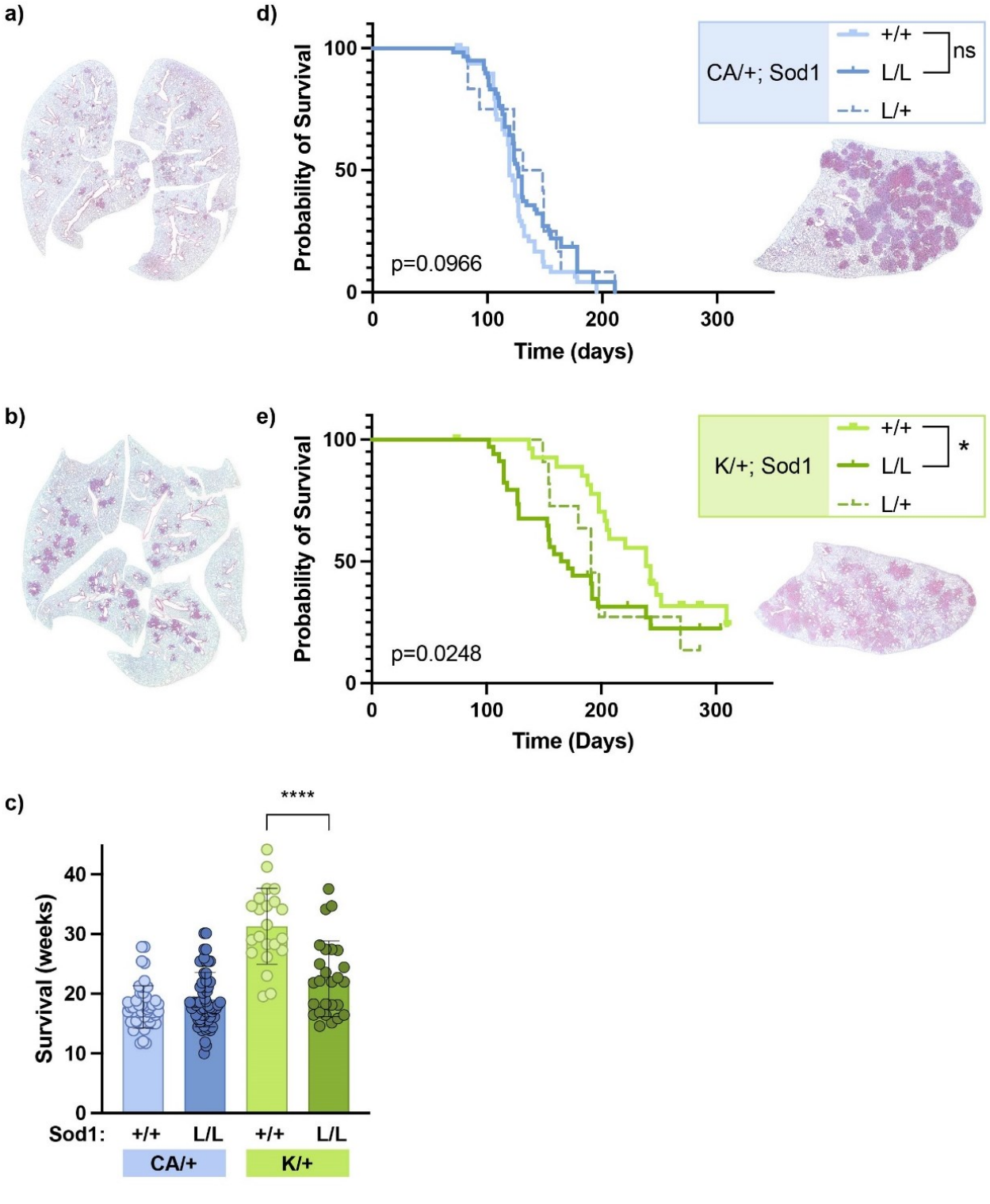
a)
b)
c)
d)
e)
Probability of Survival
100
50
0
0
100
200
300
Time (days)
p=0.0966
CA/+; Sod1
+/+
L/L
L/+
ns
Time (Days)
p=0.0248
K/+; Sod1
*
****
Survival (weeks)
40
30
20
10
0
Sod1:
+/+
L/L
+/+
L/L
CA/+
K/+

Figure 3.1- Kaplan-Meier Analysis of SOD1 loss in Oncogenic Braf- and Kras-Driven Lung Cancer Models.

Small tumors are visible in representative H&E-stained lung sections from **(a)** $Braf^{CA/+}$; $Sod1^{L/L}$ and **(b)** $Kras^{LSL/+}$; $Sod1^{L/L}$ mice, 8 weeks post-AdCre tumor induction. **(c)** Survival duration (in weeks) following tumor induction across four genotypes. Mean with standard deviation plotted. **(d)** Kaplan-Meier survival curve for mice with Braf-driven lung tumors, comparing $Sod1^{+/+}$, $Sod1^{L/+}$, and $Sod1^{L/L}$ genotypes. Representative tumor burden H&E image included. **(e)** Kaplan-Meier survival curve for mice with Kras-driven lung tumors, comparing $Sod1^{+/+}$, $Sod1^{L/+}$, and $Sod1^{L/L}$ genotypes. Representative tumor burden H&E image included. P-values were computed via Log-rank analysis. Representative tumor burden image included.
[(ns, $P>0.05$); (∗, $P\leq0.05$); (∗∗, $P\leq0.01$); (∗∗∗, $P\leq0.001$)]

3.2 Tumor Metrics

Sod1 expression significantly affects tumor count, size, and burden in both oncogene models

Aiming to elucidate the effect of Sod1 loss on both Braf and Kras tumors, FFPE samples were sectioned and H&E-stained to assess lung tumor count, area, and burden. AdCre infection of a wild-type mouse confirmed an absence of tumors when neither the $Braf^{CA}$ nor $Kras^{LSL}$ alleles were present. Airway cross sections, comprised of cuboidal Alveolar Type 2 (AT2) epithelial cells, are easily distinguished from the long, thin Alveolar Type 1 (AT1) cells performing the gas-exchange function of the lungs **(Figure S1a)**.

At 8 weeks post-initiation, the mean tumor count in $Braf^{CA/+}$; $Sod1^{+/+}$ versus $Sod1^{L/L}$ lung sections did not significantly differ (mean count 150 vs. 136, respectively, p=0.55) **(Figure 3.2a)**. At the same timepoint, however, there were over 4 times more tumors in $Kras^{LSL/+}$; $Sod1^{L/L}$ lungs as compared to $Sod1^{+/+}$ counterparts (mean count 63.25 vs. 14.67, respectively; p=0.03), suggesting that Sod1 loss facilitates initiation of $Kras^{G12D}$-driven tumors. Tumor count was also significantly increased in the $Kras^{LSL/+}$; $Sod1^{L/L}$ endpoint samples relative to the $Sod1^{+/+}$ group, though this increase was no longer as pronounced as it was at 8 weeks (1.8-fold difference, p=0.002) **(Figure 3.2b)**. Endpoint Braf tumor counts showed no significant difference between $Sod1^{+/+}$ and $Sod1^{L/L}$ samples.

At 8 weeks post-initiation, tumors in $Sod1^{+/+}$ lungs were significantly larger in area than $Sod1^{L/L}$ counterparts across both genotypes (Braf: 1.6-fold increase, p<0.0001; Kras: 1.5-fold increase, p=0.003) **(Figure 3.2c)**. $Kras^{LSL/+}$; $Sod1^{+/+}$ tumors remaining larger than their $Sod1^{L/L}$ counterparts at endpoint (1.2-fold increase, p=0.0005); endpoint $Braf^{CA/+}$; $Sod1^{L/L}$ tumor growth instead outpaced that of $Sod1^{+/+}$ tumors (1.2-fold increase, p<0.0001) **(Figure 3.2d)**. Overall,

Sod1 expression promoted increased tumor growth in early Braf and Kras samples. This increased growth was retained in endpoint Kras tumors, but abolished in endpoint Braf tumors.

Measures of tumor burden at the early 8-week timepoint **(Figure 3.2e)** showed that $Kras^{LSL/+}$; $Sod1^{L/L}$ mice have significantly increased tumor burden as compared to their $Sod1^{+/+}$ counterparts (2.6-fold increase, p=0.006); no significant difference was apparent between $Braf^{CA/+}$; $Sod1^{+/+}$ and $Sod1^{L/L}$ mice (p=0.76). Endpoint samples differed; Sod1 loss significantly increased endpoint tumor burden in both Braf (1.4-fold increase, p=0.04) and Kras (1.5-fold increase, p=0.03) samples **(Figure 3.2f)**.

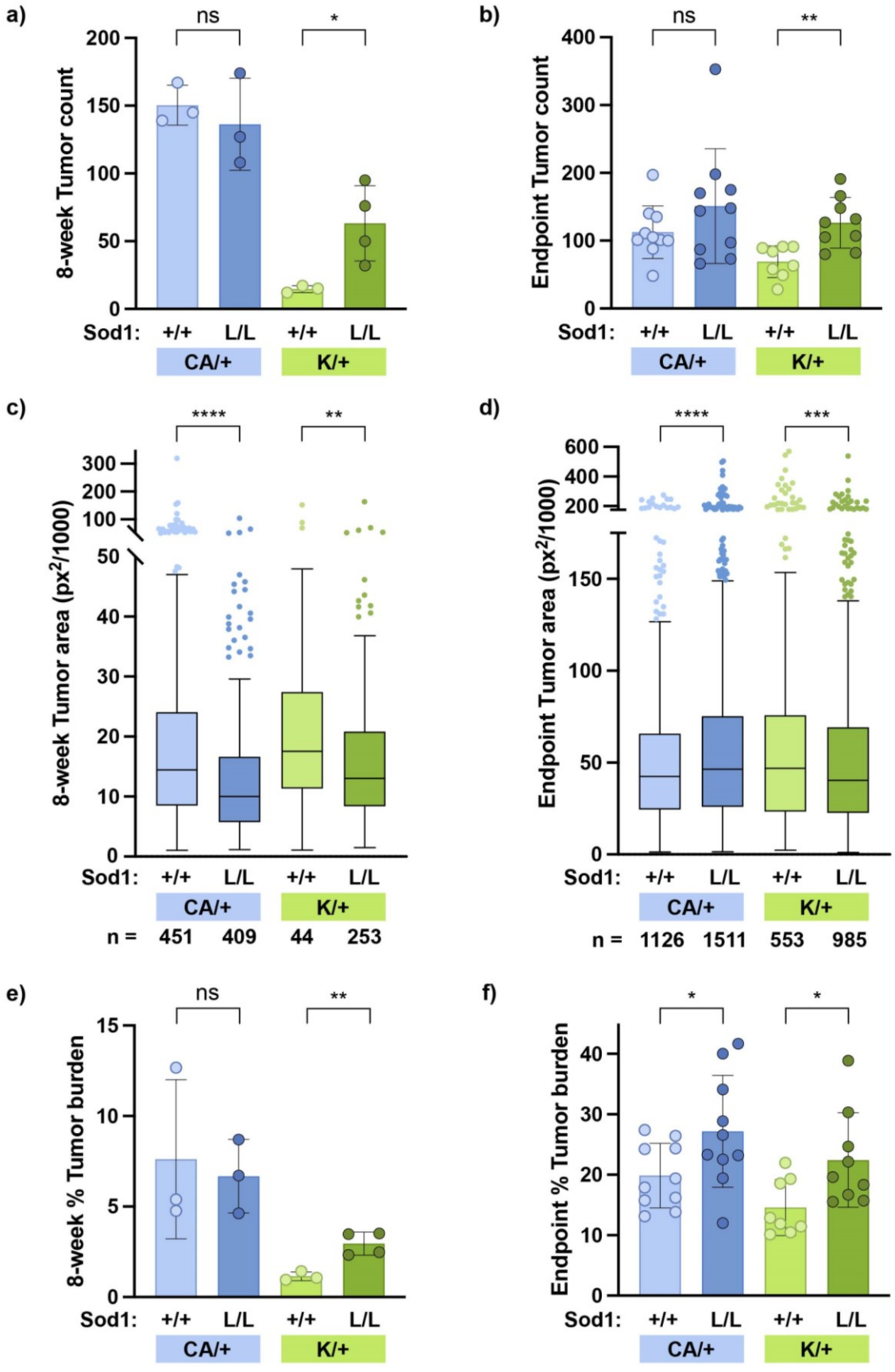
a)
ns
*
8-week Tumor count
200
150
100
50
0
Sod1: +/+ L/L +/+ L/L
CA/+
K/+
b)
ns
**
Endpoint Tumor count
400
300
200
100
0
Sod1: +/+ L/L +/+ L/L
CA/+
K/+
c)
****
**
8-week Tumor area (px²/1000)
300
200
100
50
40
30
20
10
0
Sod1: +/+ L/L +/+ L/L
CA/+
K/+
n = 451 409 44 253
d)
****
***
Endpoint Tumor area (px²/1000)
600
400
200
150
100
50
0
Sod1: +/+ L/L +/+ L/L
CA/+
K/+
n = 1126 1511 553 985
e)
ns
**
8-week % Tumor burden
15
10
5
0
Sod1: +/+ L/L +/+ L/L
CA/+
K/+
f)
*
*
Endpoint % Tumor burden
40
30
20
10
0
Sod1: +/+ L/L +/+ L/L
CA/+
K/+

Figure 3.2- Tumor count, area, and burden in BRAF- and KRAS-driven lung tumors with SOD1 loss

(a, b) Tumor count at (a) 8 weeks post-initiation, and (b) experimental endpoint, with each datapoint representing the number of tumors in a single lung section. Mean with standard deviation plotted. **(c, d)** Tukey box-and-whiskers plot of tumor area measurements, (c) 8 weeks post-initiation, and (d) at experimental endpoint. Each datapoint represents an individual tumor, with n indicating the number of analyzed tumors. Error bars designate 1.5 times the interquartile range. **(e, f)** Percent tumor burden at (e) 8 weeks post-initiation, and (f) at endpoint. Each datapoint represents the percent burden in one lung sample, with each sample originating from an individual mouse. Mean with standard deviation plotted.
[(ns, $P>0.05$); (∗, $P\leq0.05$); (∗∗, $P\leq0.01$); (∗∗∗, $P\leq0.001$); (∗∗∗∗, $P\leq0.0001$)]

3.3 Escapee Sod1 Expression

3.3.1 Sod1 ablation in tumors of Sod1$^{L/L}$ mice was not universal

Lung sections were stained with anti-Sod1 antibody to confirm that AdCre infection successfully initiated recombination of Sod1^{Lox} alleles, resulting in complete Sod1 loss in the tumors of Sod1$^{L/L}$ mice. Unexpectedly, Sod1 loss was not universal in the tumors of Sod1$^{L/L}$ mice. This realization came about when testing Sod1 antibodies in immunofluorescence analyses of Sod1$^{L/L}$ FFPE lung sections. Whereas no Sod1 fluorescence signal was apparent using the Abcam antibody, unexpected fluorescence using the Proteintech antibody suggested that not all tumors in Sod1$^{L/L}$ lungs were Sod1-null **(Figure S1c, left)**. Whereas most tumors did show the expected absence of Sod1 signal, others appeared to retain varying levels of Sod1 expression, as confirmed via immunohistochemical staining **(Figure S1c, right)**.

This result presented an issue of nomenclature, so Sod1-expressing tumors in Sod1$^{L/L}$ mice were termed 'escapees' of Cre recombination to distinguish them from true Sod1-null tumors in these mice. This nomenclature is also useful to distinguish Sod1-positive escapee tumors from the Sod1-positive tumors of Sod1$^{+/+}$ mice.

Using the Proteintech antibody, AT2 cells of the lung epithelium retained robust WT Sod1 expression, providing an internal control confirming the lack of Sod1 in the tumors of Sod1$^{L/L}$ mice **(Figure 3.3a)**. On average, 6.3% of Braf$^{CA/+}$ tumors and 2.7% of Kras$^{LSL/+}$ tumors in Sod1$^{L/L}$ mice were escapees ($p=0.004$) **(Figure 3.3b)**. Area analyses determined that escapees, regardless of driver oncogene, were smaller in area than both Sod1$^{+/+}$ and Sod1$^{-/-}$ tumors, though the rarity of these tumors prevented the acquisition of sufficient data to achieve statistical significance for this comparison **(Figure S2a**, purple bars**)**.

Tumor density also appeared to affect escapee growth, regardless of Braf or Kras genotype; escapees in lobes with few tumors, sparsely distributed with ample room for growth, grew to larger sizes than escapees in lobes with many densely-packed tumors. Sparse lobes allowed for some very large outlier escapees **(Figure 3.3c**; pink datapoints**)**, whereas escapees in dense lobes were smaller and more irregularly-shaped. This growth pattern in sparse versus dense lobes applies to lung tumors at large (Garnett and Dankort, unpublished), and is not unique to escapees; it may be that escapees' clearly-delineated borders simply make them an especially apparent case. Notably, however, escapees in tumor-dense lobes *never* outgrew their Sod1-null neighbors, whereas those in sparser lobes often matched or exceeded the growth of Sod1-null neighbors **(Figure 3.3c**; representative images**)**.

3.3.2 Sod1 retention in escapee tumors does not correlate with ROS reduction

While tumor metrics can quantify the effect of Sod1 loss on disease severity, evaluating ROS levels was of qualitative interest. This was achieved via immunohistochemical staining for ROS proxies: markers of DNA, lipid, and protein damage that act as indirect measures of ephemeral ROS.

To attain a well-rounded perspective on ROS levels, three different markers were employed. The first, 8-Hydroxy-2'-deoxyguanosine (8-oxoG), is a marker of DNA guanine oxidation commonly employed as a ROS proxy. Generated by hydroxyl radicals, this is the most common ROS-derived DNA lesion detected via immunostaining (Valavanidis et al., 2009). The second marker selected was 3-nitrotyrosine (3-NT), formed via peroxynitrite-mediated protein nitration which interrupts protein structure and inhibits function. 3-NT formation has also been implicated in other diseases involving oxidative stress, including diabetes and neurodegeneration (Bandookwala & Sengupta, 2020). The third marker chosen was 4-hydroxynonenal (4HNE), a

product of lipid peroxidation formed via oxidative insult to polyunsaturated fatty acids. Interestingly, 4HNE also readily reacts with proteins, inducing the formation of 4HNE-protein adducts (Castro et al., 2017). These are more likely to form under conditions of severe oxidative stress, where partially-unfolded proteins reveal hydrophobic regions easily cross-linked by 4HNE. 4HNE accumulates in various cancer types and hastens cancer progression by augmenting cellular dysfunction (Gasparovic et al., 2017). Sod2 intensity was also assessed to observe whether its expression increases upon Sod1 loss, suggesting a compensatory superoxide-neutralizing function (Papa, Hahn, et al., 2014).

In terms of experimental utility, escapee split images with adjacent Sod1-positive and Sod1-null ROIs eliminated the possibility of stain variation across slides. Interestingly, Sod1 expression seemed to have no directional effect on ROS levels, with no visual distinction between escapees and Sod1-null tumors apparent in any ROS IHC images **(Figure 3.3d)**. To confirm this, stain intensity was quantified in each region, normalizing Sod1-null regions to escapees. Values over 100% indicate elevated ROS in Sod1-null regions, as might be expected if Sod1 loss permits accumulation of oxidative damage. Neither Braf **(Figure 3.3e)** nor Kras **(Figure 3.3f)** tumors demonstrated ROS elevation in Sod1-null tumors. Sod2 elevation was likewise undetected.

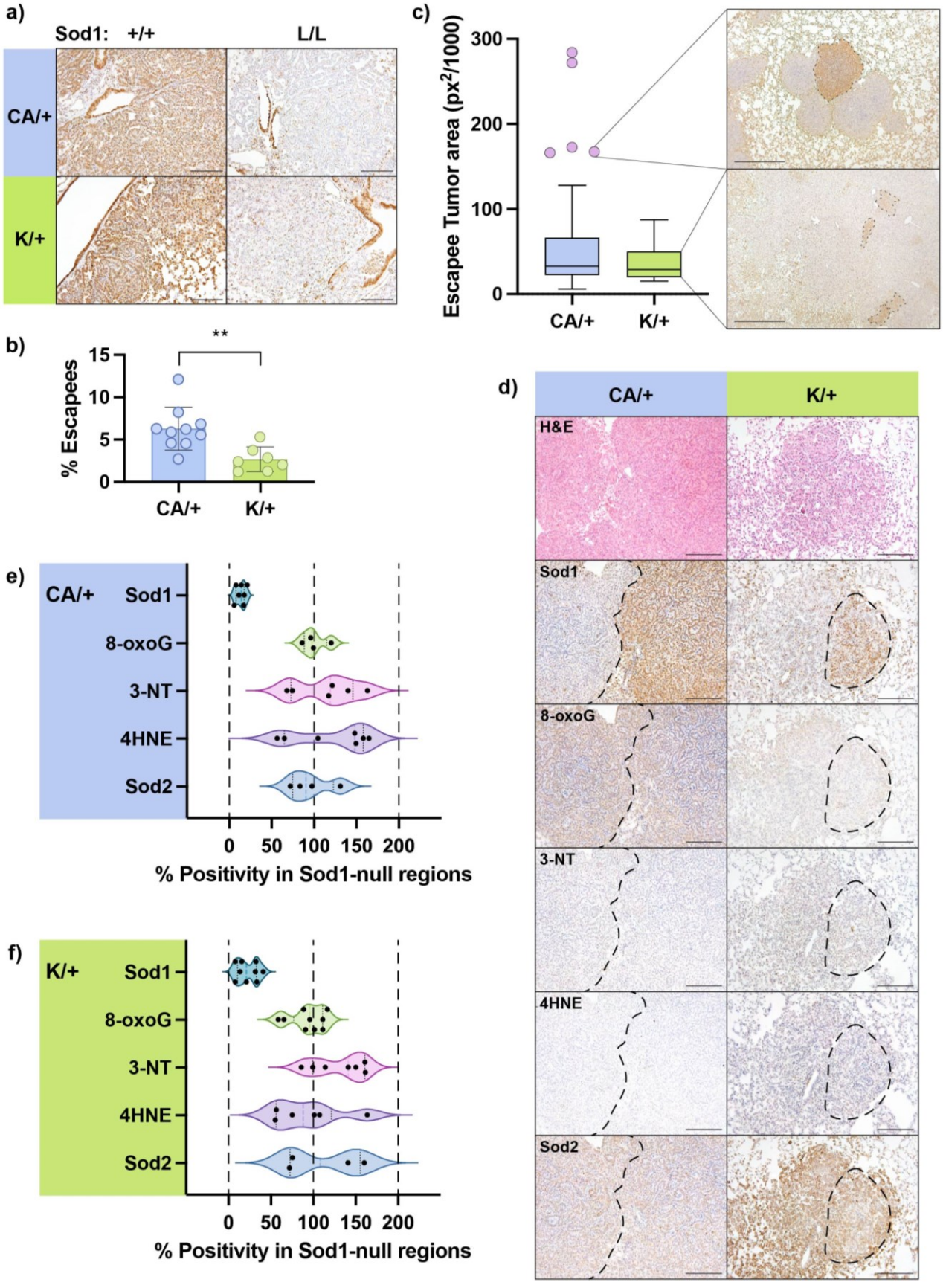
a)
Sod1: +/+
L/L
CA/+
K/+
b)
**
% Escapees
15
10
5
0
CA/+
K/+
c)
Escapee Tumor area (px²/1000)
300
200
100
0
CA/+
K/+
d)
CA/+
K/+
H&E
Sod1
8-oxoG
3-NT
4HNE
Sod2
e)
CA/+
Sod1
8-oxoG
3-NT
4HNE
Sod2
0
50
100
150
200
% Positivity in Sod1-null regions
f)
K/+
Sod1
8-oxoG
3-NT
4HNE
Sod2
0
50
100
150
200
% Positivity in Sod1-null regions

Figure 3.3- Identification and characterization of SOD1-expressing escapee tumors in BRAF- and KRAS-driven lung cancer models.

(a) Anti-Sod1 immunohistochemical staining of FFPE sections. Representative images of Sod1-WT (left) and Sod1-null (right) tumors in both Braf and Kras oncogenic backgrounds. Lack of Sod1 staining in Sod1-null tumors contrasts with richly-stained Sod1-positive AT2 airway cross sections. 200X magnification, scale bar = 200μm. **(b)** Quantification of escapee tumor count as a percentage of total tumors. Each datapoint represents the percent escapees in one lung section, as determined by IHC staining for Sod1 (∗∗, P≤0.01). **(c)** Tumor area quantification is displayed as a box-and-whisker plot with outliers identified using the Tukey method. Pink datapoints above the upper quartile represent outlier tumors beyond 1.5 times the interquartile range, in this case, the largest 5% of escapees. Sample images compare escapee size in sparse versus dense lobes; one large outlier $Braf^{CA/+}$ escapee (above), contrasts small, irregular $Kras^{LSL/+}$ escapees (below). 100X magnification, scale bar = 500μm. **(d)** Representative Braf (left) and Kras (right) split images with serial sections stained for Sod1, ROS markers 8-oxoG, 3-NT, and 4HNE, and mitochondrial antioxidant Sod2. Dashed lines delineate Sod1-null and escapee tumors. 200X magnification, scale bar = 200μm. **(e, f)** Quantification of ROS markers in (e) Braf and (f) Kras escapee split images. Each datapoint represents a ratio of marker positivity in one split image. Values above 100% indicate elevated marker positivity in Sod1-null tumors.

3.3.3 Escapees express highly variable levels of SOD1

Tumors in $Sod1^{+/+}$ sections of both oncogenes exhibit strong, uniform Sod1 staining throughout, confirming robust Sod1 expression in tumors of $Sod1^{+/+}$ mice **(Figure S1b)**. Examining escapees, however, suggested more complex Sod1 regulation is likely at play. Rather than a pattern of discrete stepwise Sod1 staining, as may be expected in the case of $Sod1^{L/L}$ (100% WT expression) and $Sod1^{L/-}$ (50% WT expression) genotypes, a wide range of Sod1 stain intensity is evident across $Sod1^{L/L}$ escapees. For example, the $Braf^{CA/+}$; $Sod1^{L/L}$ lung section in **Figure 3.3g** contains 375 tumors, 22 of which are escapees. While the cells within any one escapee tumor display uniform Sod1 expression, varying Sod1 expression levels are apparent when comparing different escapee tumors, as in the representative zoomed regions. $Kras^{LSL/+}$ escapees demonstrated this same trend **(Figure 3.3h)**. The homogeneity of Sod1 staining within escapees suggests that they are derived from a single original founder cell.

Sod1 intracellular localization also varied among escapees in an oncogene-dependent manner. Control tumors in $Sod1^{+/+}$ lung sections of both oncogenes showed ubiquitous Sod1 expression in both the cytoplasm and nucleus **(Figure S1b).** Interestingly, Sod1 localization in Braf escapees appeared to vary based on the strength of expression, with deeply stained escapees displaying Sod1 localization throughout the cell **(Figure 3.3g**, left**)**, and areas of weaker Sod1 expression appearing to concentrate exclusively in the cytoplasm, excluding the nuclei **(Figure 3.3g**, right**)**. In contrast, Kras escapees appear to retain predominantly nuclear Sod1 expression, regardless of the strength of Sod1 expression **(Figure 3.3h)**.

g)

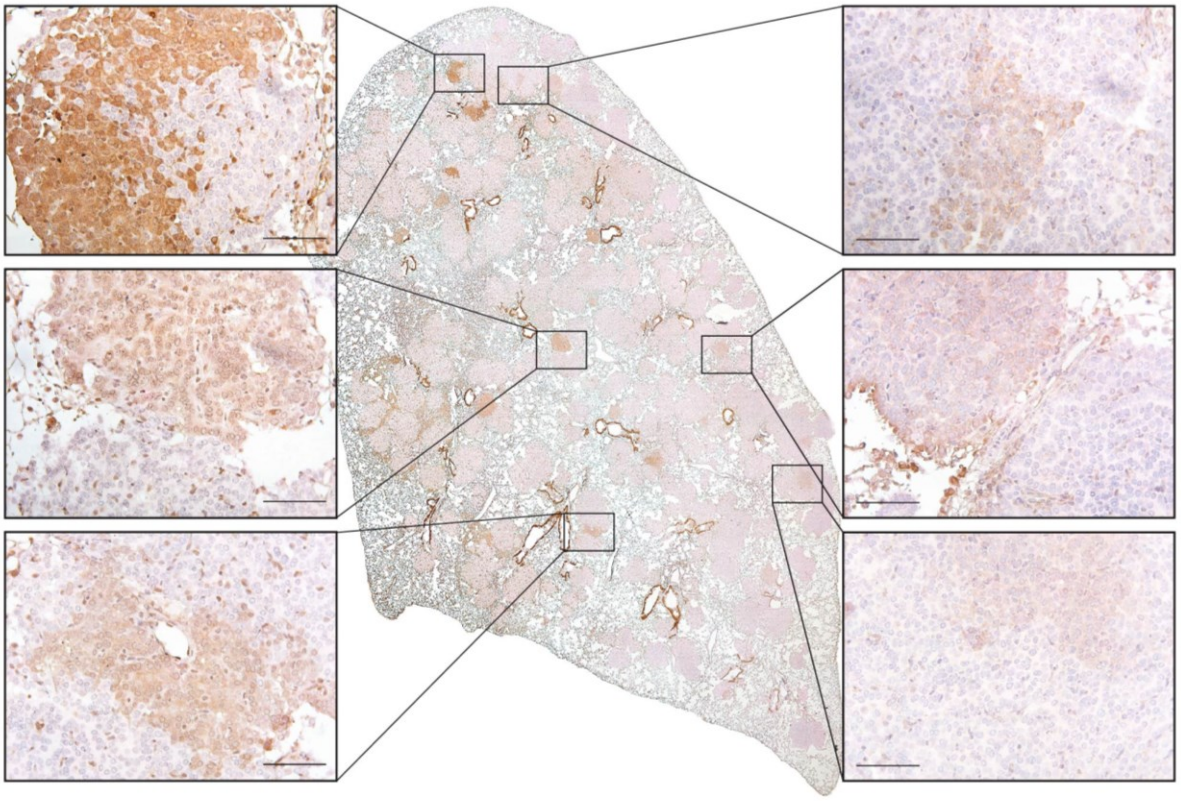

h)

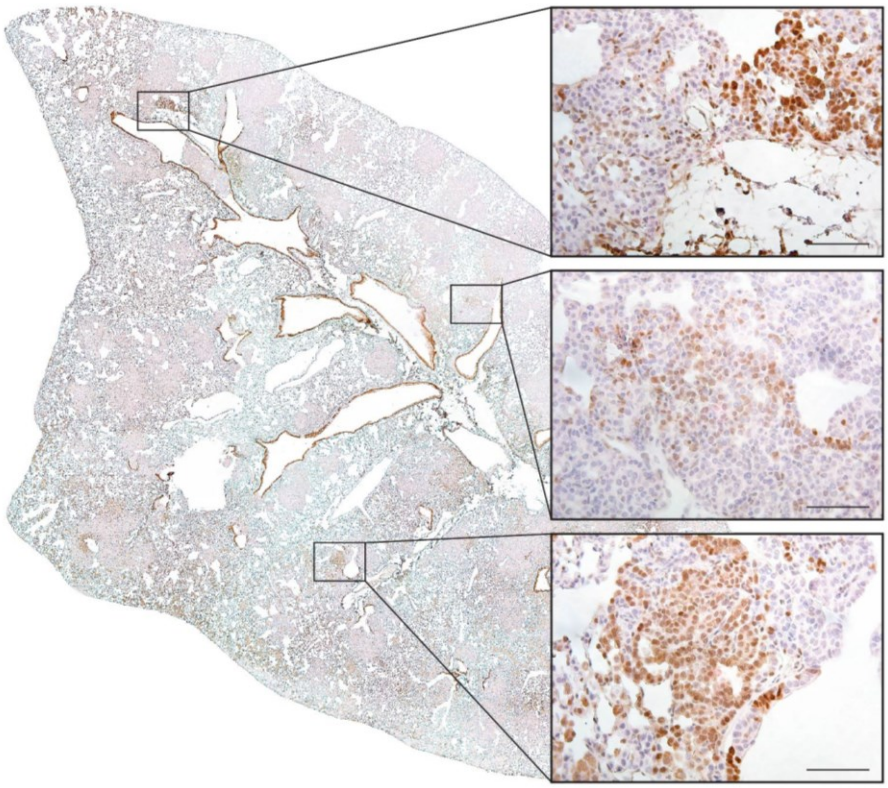

Figure 3.3 (continued)- Panoramic views of representative Braf and Kras lung sections

(g) Panoramic view of representative $Braf^{CA/+}$; $Sod1^{L/L}$ lung section, compiled from 50X magnification images. Highlighted regions indicate escapee tumors of differing Sod1 expression intensities. Escapees with deeper staining localize Sod1 in both the cytoplasm and nucleus (left), while escapees with weaker staining exclude Sod1 from the nucleus (right). Magnification 400X, scale bars = 100μm. **(h)** Panoramic view of representative $Kras^{LSL/+}$; $Sod1^{L/L}$ lung section. Regions of interest highlight nuclear Sod1 localization. Magnification 400X, scale bars = 100μm.

3.4 ROS Quantification

ROS elevation in Sod1$^{L/L}$ lungs is oncogene-dependent

Whereas no significant difference in ROS was noted in escapee split image analyses, more striking trends were observed when analyzing a number of tumors from their respective genotypes.

Analysis of relative 8-oxoG positivity indicated an increase in DNA lesions in Braf$^{CA/+}$; Sod1$^{+/+}$ tumors as compared to their Sod1$^{-/-}$ counterparts (p=0.0125). This trend was reversed in Kras tumors, where increased 8-oxoG positivity in Sod1$^{-/-}$ tumors was apparent (1.7 times that of Sod1$^{+/+}$ counterparts; p=0.0001) **(Figure 3.4a, b)**.

Braf tumors sustained very little detectable protein nitration, with the difference between Sod1$^{+/+}$ and Sod1$^{-/-}$ tumors negligible despite statistical significance (p=0.0304). Kras$^{LSL/+}$; Sod1$^{-/-}$ tumors, in contrast, show 1.8-fold higher 3-NT positivity than their Sod1$^{+/+}$ counterparts (p=0.0015) **(Figure 3.4c, d)**.

4HNE staining varied widely among tumors, irrespective of tumor genotype. 4HNE aggregates appeared as swaths of rich staining in isolated pockets within tumor tissue **(Figure 3.4e)**. Larger and higher-grade tumors exhibited more positivity than lower grade tumors in the same lung section. Tumors growing within airways also exhibited more 4HNE positivity than airway-external neighbors (**Figure 3.4e**, above), with Sod1 loss confirmed in both (**Figure 3.4e**, below). Such airway tumors likely experience increased oxygen exposure, predisposing them to oxidative stress. This pattern aligns neatly with noted 4HNE immunostaining in cancer-associated stromal cells, advanced tumors, and regions of necrosis (Gęgotek et al., 2016; Zarkovic et al., 2017). Staining may manifest both intra- and extracellularly, independent of tumor genotype (Nègre-Salvayre et al., 2017).

Limited analyses of phospho-ERK (pERK, a measure of MAPK pathway activation) demonstrated pERK enrichment in peripheral regions of Kras tumors of both Sod1 genotypes (**Figure 3.4f**, regions enclosed by dashed lines). This was consistent with a center-out growth pattern particular to Kras tumors, with Braf tumors more often exhibiting uniform distributions of low basal pERK signal.

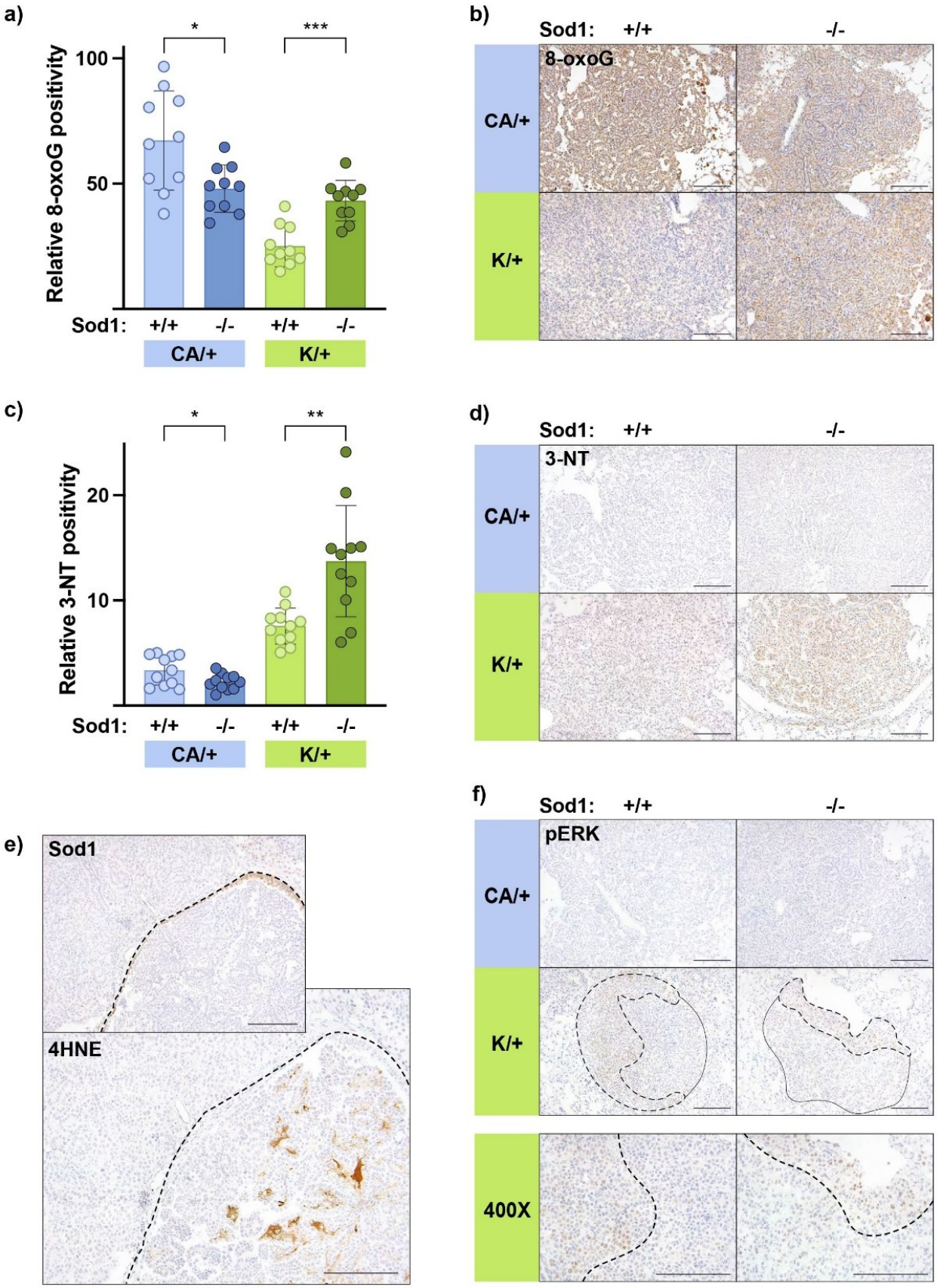
a)
Relative 8-oxoG positivity
100
50
*
***
Sod1: +/+ -/- +/+ -/-
CA/+
K/+
b)
Sod1: +/+ -/-
8-oxoG
CA/+
K/+
c)
Relative 3-NT positivity
20
10
*
**
Sod1: +/+ -/- +/+ -/-
CA/+
K/+
d)
Sod1: +/+ -/-
3-NT
CA/+
K/+
e)
Sod1
4HNE
f)
Sod1: +/+ -/-
pERK
CA/+
K/+
400X

Figure 3.4- Quantification of ROS and MAPK signaling in Sod1-null lung tumors.

FFPE lung sections were subjected to immunohistochemical staining. **(a)** Quantification of relative 8-oxoG positivity and **(b)** representative images across all four genotypes. 200X magnification, scale bar = 200μm. **(c)** Quantification of relative 3-NT positivity and **(d)** representative images across all four genotypes. 200X magnification, scale bar = 200μm. [(ns, $P>0.05$); (∗, $P\leq0.05$); (∗∗, $P\leq0.01$); (∗∗∗, $P\leq0.001$)] **(e)** Representative images indicating 4HNE positivity in a $Braf^{CA/+}$; $Sod1^{-/-}$ airway tumor adjacent to a tumor growing outside the airway. **(f)** Representative pERK staining in all four genotypes. Solid lines outline tumor boundaries; dashed lines highlight peripheral Kras tumor regions with elevated pERK staining. 200X magnification, scale bar = 200μm. 400X magnification to emphasize stain differential in Kras tumors, scale bar = 200μm.

3.5 Immune Involvement

Immune infiltrate is enriched in lungs with Kras^{G12D}-driven tumors

Given the significant and dramatic difference in the effect of Sod1 status on the survival of mice with Kras versus Braf tumors, and the insufficiency of tumor metrics in explaining this difference, the involvement of immune cells was investigated. Immune cells appear to have contradictory roles in tumor proliferation, sometimes targeting tumors for destruction, and sometimes promoting tumor growth by exacerbating ROS levels (Kotsafti et al., 2020). Indeed, immunohistochemical staining characterized immune cells as having extraordinarily high ROS positivity **(Figure 3.5a)**. Given the lung's role in gas exchange, a reduction in alveolar function due to intense immune infiltration could also impact respiratory function and organismal survival in a tumor-independent manner.

Panoramic images of Sod1-stained lung sections from approximately 50 mice were scored on a scale of 1-6, with a score of 6 indicating a lobe where immune cells predominate available alveolar spaces **(Figure 3.5b-i)**, and a score of 1 indicating no immune involvement **(Figure 3.5b-ii)**. The genotypes of all lobes were blinded before scoring, and the results were compiled **(Figure 3.5b-iii)**. Interestingly, immune involvement is independent of Sod1 expression, and instead varies based on the driver oncogene. Whereas lobes with Braf tumors were largely free of immune involvement, immune infiltrate was significantly higher in lobes with Kras tumors (**Figure 3.5b-iii**, purple bars). Differential immune involvement in Braf vs. Kras tumor models is thus a possible explanatory variable for the varied effects of Sod1 on survival, providing two distinct biological landscapes upon which Sod1 loss can act.

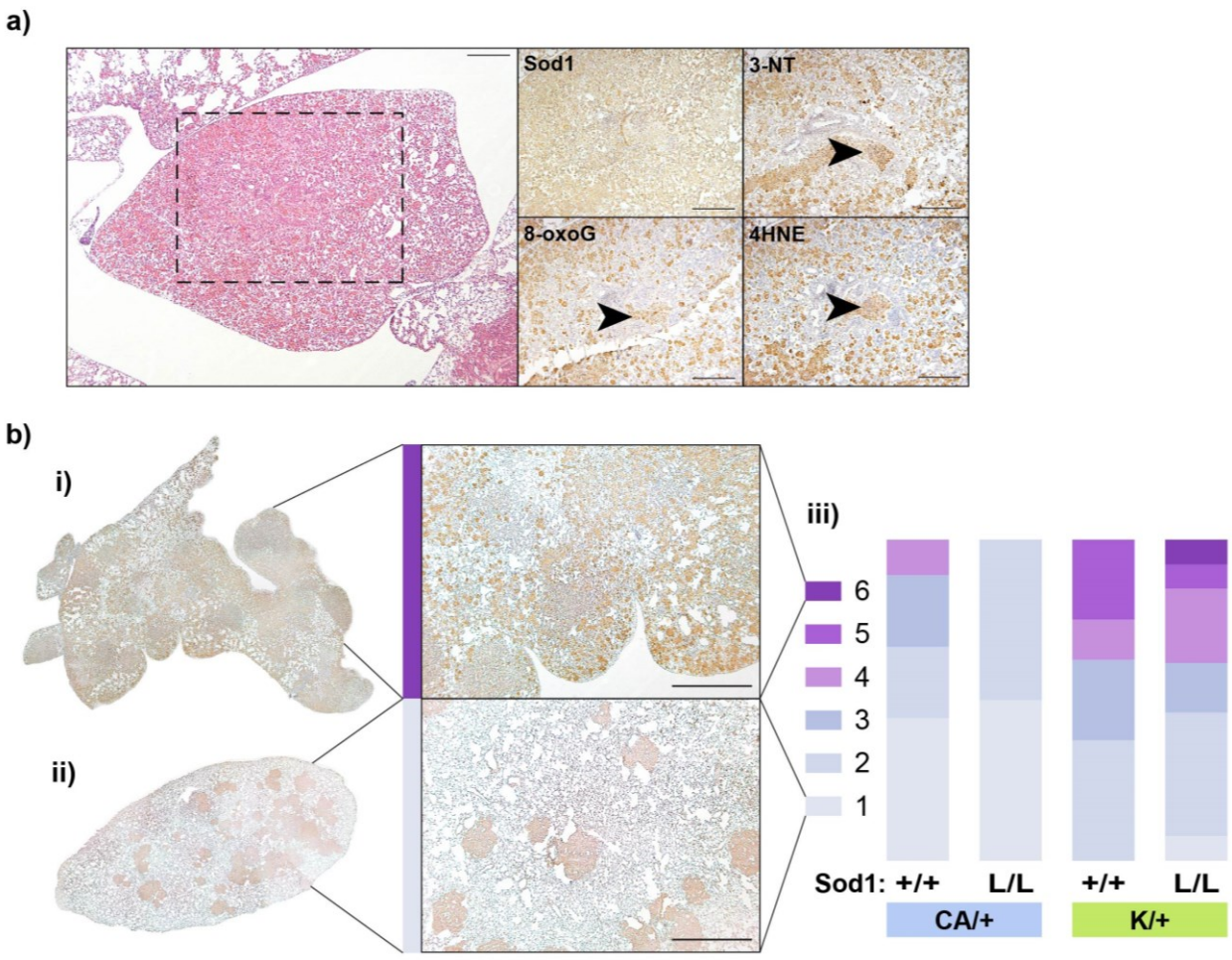

Figure 3.5- Increased Immune Infiltration and Oxidative Stress in lungs with Kras-driven tumors

(a) Representative lung section showing a region with high levels of immune infiltrate; H&E, 100X magnification, scale bar = 200µm. Sod1 immunohistochemical staining reveals high Sod1 expression in immune cell infiltrates. Staining for ROS markers 8-oxoG, 3-NT, and 4HNE demonstrate high ROS levels in immune infiltrate. Black arrowheads indicate regions of high marker positivity. 200X magnification, scale bar = 200µm. **(b)** Immune cell infiltrate analysis, scored on a scale of 1-6, showing variation in infiltrate levels across different genotypes. *(i)* Representative 8-oxoG IHC staining of a high infiltrate lobe, scored 6. 50X magnification zoom, scale bar = 500 µm. *(ii)* Representative 8-oxoG IHC staining of a low infiltrate lobe, scored 1. 50X magnification zoom, scale bar = 500 µm. *(iii)* Compiled data, n=8-13 per group. Lobes with low levels of infiltrate are designated in blue, high levels in purple.

3.6 *In vitro* Cell Culture

Sod1$^{L/L}$ tumor-derived cell lines retain Sod1 expression

Lung tumor cell lines derived from Braf- and Kras-driven tumors with p53 deletion (BP and KP cells, respectively) were previously developed for *in vitro* study. Of continued interest was the development of parallel cell lines modelling Sod1 deletion in these two backgrounds.

To generate these cell lines, Cre-activated p53 deletion was bred into Braf$^{CA/+}$; Sod1$^{L/L}$ and Kras$^{LSL/+}$; Sod1$^{L/L}$ mice, resulting in the Braf$^{CA/+}$; Sod1$^{L/L}$; p53$^{L/L}$ and Kras$^{LSL/+}$; Sod1$^{L/L}$; p53$^{L/L}$ genotypes (allowing creation of BPSod and KPSod cell lines, respectively). Mice were infected with AdCre at 8 weeks of age, stimulating tumor initiation, Sod1 loss, and p53 loss. Tumor progression was hastened as compared to p53-competent counterparts, with severe respiratory decline prompting lung collection at just 10-12 weeks post tumor initiation. Epithelial-derived cell populations were isolated and cloned for further analyses.

Cell clones underwent PCR genotyping to confirm their tumor provenance. Primer sets were selected to detect the wild-type, un-recombined mutant, and Cre-recombined mutant allele variants (Braf/Kras, Sod1, and p53) to assess the cells' genetic makeup. Among clones tested (Braf n=16, sourced from two mice; Kras n=17, one mouse), all retained one copy of the un-recombined Sod1^{Lox} allele, suggesting they were likely derived from escapee tumors **(Figure 3.6a, b)**. The exclusive survival of clones retaining the un-recombined Sod1 allele also suggests that some level of Sod1 expression is required for growth in culture (despite Sod1$^{-/-}$ tumors being clearly viable *in vivo*).

Acting on this assumption, Sod1 expression levels of two BPSod (1435-8, 1448-8) and two KPSod (303-4, 303-14) cell clones, all strongly positive for the Cre-recombined Sod1Δ allele, were assessed for Sod1 protein expression via immunoblot analysis **(Figure 3.6c).** Quantified results

showed dramatic variations in Sod1 protein expression among the clones tested; BP and KP cell lines provided WT Sod1 controls **(Figure 3.6d)**. Both BPSod clones exhibited reduced Sod1 expression as compared to BP controls, with clone 1435-8 having significantly reduced in Sod1 expression (47.22% mean Sod1 expression, $p<0.0001$; 1448-8, 73.54% mean Sod1 expression, $p=0.2099$). KPSod clone 303-4 expressed Sod1 at 128.4% KP levels, but this was not statistically significant ($p=0.4624$). KPSod clone 303-14 expressed Sod1 at 94.61% KP levels ($p=0.0465$). Analyses of cell growth confirmed reduced proliferative speed in the Sod1-deficient clones, and even slightly elevated growth in Kras clone 303-4 with increased Sod1 expression **(Figure 3.6e)**.

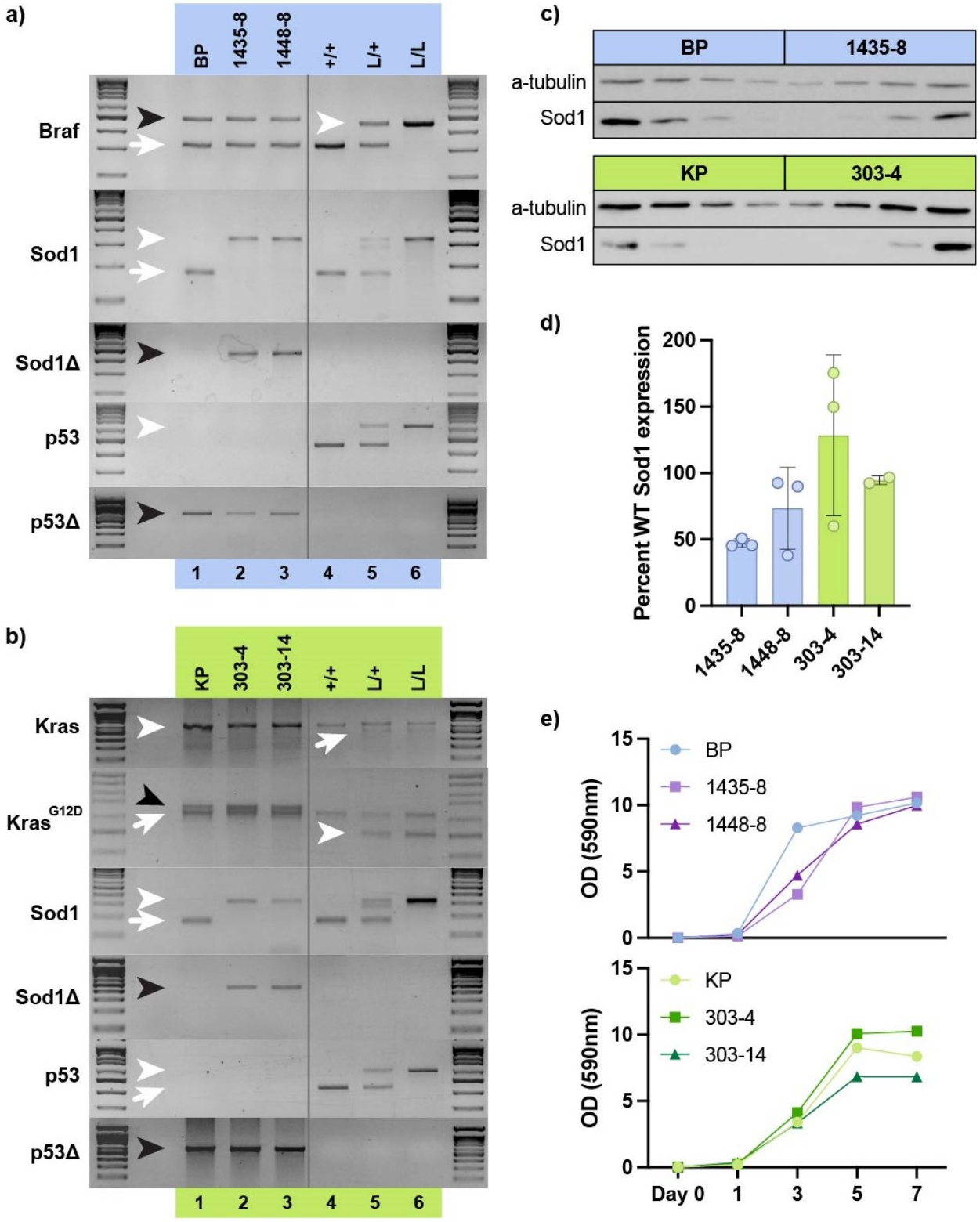
a)
BP
1435-8
1448-8
+/+
L/+
L/L
Braf
Sod1
Sod1Δ
p53
p53Δ
1 2 3 4 5 6
b)
KP
303-4
303-14
+/+
L/+
L/L
Kras
KrasG12D
Sod1
Sod1Δ
p53
p53Δ
1 2 3 4 5 6
c)
BP
1435-8
a-tubulin
Sod1
KP
303-4
a-tubulin
Sod1
d)
Percent WT Sod1 expression
200
150
100
50
0
1435-8
1448-8
303-4
303-14
e)
OD (590nm)
15
10
5
0
BP
1435-8
1448-8
KP
303-4
303-14
Day 0 1 3 5 7

Figure 3.6- Molecular characterization of BPSod and KPSod tumor cell lines

PCR genotyping of BPSod and KPSod clones. Primers are mixed to generate diagnostic bands for all possible Braf, Kras, Sod1, and p53 genotypes, distinguishing between WT, LoxP-flanked (floxed), and Cre-recombined allele variants. White arrows indicate WT alleles; white arrowheads indicate floxed alleles; black arrowheads indicate Cre-recombined (Δ) alleles. Both the floxed and recombined Braf alleles can be detected by the same primer set, with the $Braf^{V600E}$ allele indicated by the black arrowhead and the $Braf^{LoxP}$ allele indicated by the white arrowhead in the control lanes. The Kras, Sod1, and p53 alleles each require two primer sets to detect all allele variants. **(a)** Lane 1: BP control cell DNA. Lanes 2-3: BPSod clone cell DNA (1435-8, 1448-8). Lanes 4-6: FVB/N wild-type control, heterozygous floxed control, and homozygous floxed control tail DNA. Control BP cells (Lane 1) contain the mutant $Braf^{V600E}$, WT Sod1, and Cre-recombined p53 (p53Δ) alleles. Both BPSod clones (Lanes 2-3) demonstrate the presence of mutant $Braf^{V600E}$, $Sod1^{LoxP}$, Sod1Δ, and p53Δ. Notably, both $Sod1^{LoxP}$ and Sod1Δ are present in both clones. **(b)** Lane 1: KP control cell DNA. Lanes 2-3: KPSod clone cell DNA (303-4, 303-14). Lanes 4-6: FVB/N wild-type control, heterozygous floxed control, and homozygous floxed control tail DNA. Control KP cells (Lane 1) demonstrate the presence of the $Kras^{G12D}$, WT Sod1, and p53Δ alleles. Both KPSod clones (Lanes 2-3) demonstrate the presence of mutant $Kras^{G12D}$, $Sod1^{LoxP}$, Sod1Δ, and p53Δ. Notably, both the $Sod1^{LoxP}$ and Sod1Δ alleles are present in both clones. **(c)** Sample western blots with a-tubulin loading controls and Sod1-probed bands demonstrate altered Sod1 expression in BPSod and KPSod cell clones compared to WT controls. **(d)** Quantification of western blot data. Each datapoint represents a distinct cell lysate of the respective clone (n=3 lysates per clone). **(e)** Growth curve analyses of BP vs. BPSod clones (above) and KP vs. KPSod clones (below) over the course of 7 days. Cell growth plateaus in Days 5-7 as confluence is reached.

Chapter 4: Data Interpretation

4.1 Discussion and Future Directions

4.1.1 $Kras^{LSL/+}; p53^{-/-}$ murine LUAD models suggest tumors require Sod1 for growth

The dramatic survival differential in mice with oncogenic $Kras^{G12D}$ tumors of differing Sod1 status, and the lack of this differential in $Braf^{V600E}$ tumors, initiated the investigations of this work. This result was intriguing, in part, due to its apparent incongruence with the established literature regarding Sod1 ablation in a murine model of Kras-driven lung cancer.

Previous work by Wang et al. (2021) generated mice with AdFlp–initiated $Kras^{LSL/+}$; $p53^{-/-}$ lung tumors and tamoxifen-induced whole body Sod1 ablation. Lungs were collected at early (5 week) and late (14 week) timepoints after tumor initiation. Early timepoint samples showed a slightly higher tumor burden in $Sod1^{-/-}$ mice. Late timepoint samples, predominated by adenocarcinomas, showed the opposite result, with $Sod1^{-/-}$ mice exhibiting reduced tumor burden. IHC staining was also performed with antibodies recognizing γH2AX (a marker for DNA double strand breaks) and cleaved caspase 3 (CC3, a marker of apoptosis), neither of which differed significantly based on Sod1 expression (Brentnall et al., 2013; Mah et al., 2010). Taken as a whole, Wang et al. conclude that 1) Sod1 loss is initially pro-tumorigenic, but 2) stalls growth of late-stage adenocarcinomas, and 3) has no discernable effect on DNA damage or apoptosis. This effect on tumor growth parallels what would be expected if Sod1 loss raised ROS levels; whereas elevated ROS spurs early tumor initiation and growth, excessively elevated ROS has a cytotoxic or senescence-inducing antitumorigenic effect (Shah & Rogoff, 2021). Yet, as the authors concede, neither DNA damage nor apoptosis were elevated. Contextualizing this result within the research undertaken here begs an interesting question: Should Sod1 loss truly be detrimental to

long-term replicative competence, why is tumor burden so much higher and lifespan so much shorter in the model of Kras-driven, Sod1-null lung cancer newly described here?

4.1.2 p53 is critically involved in lung repair, LUAD restraint, and ROS mitigation

The most plausible explanation for these conflicting results is the genetic makeup of the mice, namely, the loss or retention of p53. Mutations in p53, a tumor suppressor gene involved in cell cycle arrest and apoptosis, are often observed in instances of Kras-driven LUAD (42%), with the combination linked to poorer prognoses than Kras mutation alone (Arbour et al., 2018; La Fleur et al., 2019).

Canonically, p53 is activated upon lung injury to protect AT2 airway stem cells as they differentiate into AT1 cells critical for gas exchange. As AT2 cells undergo intense morphological changes, stretching to become long and thin, they become especially vulnerable to DNA damage. As such, p53 and DNA damage response (DDR) signaling are promoted to protect genomic integrity (Kobayashi et al., 2020). p53 also transcriptionally activates a number of genes associated with this transitional state, with p53-deficient AT2 cells competent to enter the transitional state, but unable to complete AT1 differentiation (Kobayashi et al., 2020).

p53 performs an analogous role in tumorigenesis, activated in transitional cells to 1) promote the transcriptional profile of differentiated AT1 cells over the stem cell profile of AT2 cells, and 2) restrain AT2 cell hyperproliferation. Studies of Kras-driven LUAD have shown that even tumor cells exhibit AT1 transcriptional profiles, despite being derived from AT2 cells; this demonstrates the potency of p53 in restricting aberrant cell plasticity. p53 ablation results in the accumulation of transitional cells, a state associated with poor prognoses in both human LUAD and non-oncogenic lung diseases such as idiopathic pulmonary fibrosis (Kaiser et al., 2023).

As part of the DDR pathway, p53 can be stimulated indirectly via ROS-driven DNA oxidation or activated directly via ROS-driven oxidation of its sensitive cysteine residues (Seo et al., 2002). Pathways upstream of p53 are also ROS-sensitive, with protein kinases like JNK and p38MAPK also regulated by oxidative modifications (Shi & Dansen, 2020). Activated p53 then promotes negative regulation of ROS, elevating expression of genes involved in ROS detoxification and cell survival (Shi & Dansen, 2020). This effect is acute: siRNA inhibition of p53 in unstressed cells is sufficient to cause ROS increases akin to direct treatment with H_2O_2 (Sablina et al., 2005). *Given the pivotal role of p53 in reducing AT2 cell stemness in both lung injury and LUAD, and the parallel functions of p53 and Sod1 in maintaining redox balance, it is not surprising that altering p53 status gives rise to two distinct murine models of Kras-Sod1 NSCLC.*

4.1.3 p53 retention may promote the survival of Sod1-null Kras tumors

The early growth advantage of Sod1-null tumors, as evidenced by Wang et al. (2021), is recapitulated in the $Kras^{LSL/+}$; $p53^{+/+}$ model described here. Though individual tumors are larger in $Sod1^{+/+}$ samples, Sod1 loss provides a dramatic 4-fold boost in tumor initiation, which translates directly to increased tumor burden. Endpoint samples tell a similar story: tumor counts and burden are increased, and tumor area slightly decreased, in $Sod1^{L/L}$ samples. This contrasts starkly with the late timepoint samples of Wang et al. (2021), where Sod1 loss significantly reduces tumor burden. The difference between these two datasets likely stems from the loss or retention of p53, which restrains adenocarcinoma growth, initiates DDR, and mitigates effects of excess ROS (T. Chen et al., 2025; Cordani et al., 2020; Pitolli et al., 2019). Whereas robust p53 activation promotes senescence and apoptosis, moderate p53 activation is capable of promoting cell survival, activating programs of autophagy and immune escape, and even inhibiting apoptosis (Lees et al., 2021). Moderate p53 activation could thus explain concurrent increases in ROS and tumor growth

in Sod1-null Kras tumors: Sub-lethal ROS elevation, as evidenced by heightened 8-oxoG and 3-NT positivity, could stimulate protective p53 signaling, facilitating tumor cell survival and proliferation. Future research may confirm such a hypothesis by investigating endogenous p53 levels in adenomas versus adenocarcinomas of both genotypes.

4.1.4 Sod1 loss may promote the growth of Sod1-null Braf tumors

Sod1-null Braf tumors demonstrate a pattern of tumor growth and ROS levels distinguishing them from Sod1-null Kras tumors. Early Braf samples have no difference in tumor count or burden based on Sod1 status; only individual tumor areas suggest an early benefit to Sod1 retention. Endpoint samples show no significant difference in tumor count. Endpoint tumor area and burden suggest a slight growth advantage of Sod1 loss, as might be predicted by ROS-driven proliferation.

The most interesting results involve ROS quantification. Sod1-null Braf tumors appear to have *reduced* DNA oxidation and protein nitration, consistent with either a reduction in ROS, or increases in ROS-detoxifying mechanisms. While a novel result in this context, the phenomenon of reduced ROS in $Sod1^{-/-}$ conditions has been noted in several other models. *In vitro* mitochondrial assays paradoxically suggest that $Sod1^{-/-}$ mitochondria maintain stable ROS levels better than $Sod1^{+/+}$ counterparts, as H_2O_2 production is reduced, and accumulation of toxic radicals mitigated (Goldsteins et al., 2008). Sod1 as a mediator of peroxide signaling has also been suggested in yeast; whereas a small fraction of Sod1 is required for superoxide neutralization, the vast majority of cytoplasmic Sod1 thought to be involved in maintaining peroxide signaling homeostasis (Montllor-Albalate et al., 2019). Such a role may explain the advanced growth and diminished ROS positivity of $Braf^{CA/+}$; $Sod1^{-/-}$ tumors: Sod1 loss reduces H_2O_2 production, eliminating potential substrates for toxic ROS conversion, and yielding counterintuitive reductions in oxidative damage and increases in tumor size.

4.1.5 Sod1 nuclear exclusion in Braf escapees may suggest Sod1 misfolding

Extensive variation in escapee Sod1 expression levels prompted additional investigation of Sod1 IHC images. Should Sod1 expression be solely dependent on the number of active Sod1 loci, three levels of staining intensity would be expected: 1) a complete lack of Sod1 expression ($Sod1^{-/-}$), 2) approximately 50% expression ($Sod1^{-/+}$), and 3) full WT Sod1 expression ($Sod1^{+/+}$). This is not borne out by immunostaining results; instead, escapees exhibit a wide range of Sod1 stain intensity, suggesting layers of regulation beyond stepwise expression from one or two functional Sod1 loci. Additionally, Sod1 localization appeared to correlate with the strength of expression in Braf escapees. Whereas Sod1-WT Braf tumors show reliable nuclear Sod1 localization, Braf escapees appear to modulate Sod1 localization based on the strength of Sod1 expression.

Given the intrinsic Sod1/ROS connection, a pattern of reciprocal regulation was considered. *In vitro* studies have suggested that ROS levels regulate Sod1 localization, with oxidative insult stimulating Sod1 nuclear translocation and activation of genes involved in redox homeostasis (Tsang et al., 2014). Nuclear translocation can be stimulated by H_2O_2 treatment alone and is not modulated by superoxide concentration. This suggests that nuclear Sod1 functions primarily as a transcription factor, and not as a superoxide neutralizer.

Sod1 subcellular localization in Braf escapees is thus an interesting case study: escapees with intense Sod1 staining on par with WT levels show both nuclear and cytoplasmic localization, whereas those with weak Sod1 staining lack nuclear localization. These two patterns are recapitulated across Braf escapees. Nuclear staining, when present, was more intense than the hematoxylin counterstain, and concentrated reliably in the nucleoplasm. Staining was deemed cytoplasmic when the nucleoplasm was completely clear of DAB signal and analogous to nuclei

of adjacent Sod1-null tumors. As the hematoxylin counterstain reliably concentrated at the nuclear membrane, such nucleoplasmic Sod1 signal was not significantly masked. As the ROS levels of escapees and adjacent Sod1-null tumors were indistinguishable in split image analyses, altered ROS is not likely the cause of differential Sod1 localization. Given that nuclear Sod1 is primarily a transcription factor, why would this function be downregulated in weakly-expressing escapees?

One possible explanation of a lack of nuclear Sod1 might be erroneous folding of Sod1 protein. Partial unfolding of Sod1 reveals an otherwise-hidden nuclear export sequence (NES)-like sequence, which directs structurally-deformed Sod1 out of the nucleus (Xu et al., 2022; Zhong et al., 2017). Mutated SOD1, as in SOD1-ALS, has also been shown to prevent the nuclear translocation of WT Sod1, directly increasing DNA damage and contributing to ALS pathology (J. Li et al., 2019). Interestingly, this could also explain some escapees' low level of cytoplasmic Sod1 stain, as misfolded Sod1 would be preferentially targeted for proteasomal degradation, thus keeping overall levels low. One investigation inhibited the ubiquitin-proteasome system in patient-derived SOD1-ALS cell lines, and confirmed an accumulation of misfolded SOD1 in the cytoplasm (Keskin et al., 2016). Though selective *in vitro* culture of low-Sod1 escapee cells exhibiting nuclear Sod1 exclusion presents logistical challenges, their characterization would shed more light on the role of Sod1 in this NSCLC model. Alternately, escapees of differing Sod1 expression intensity and subcellular localization could be arranged in a tissue microarray, allowing more granular molecular characterization of DNA, RNA, and protein levels (Jawhar, 2009). This approach would utilize preexisting FFPE samples, circumventing the need for live cell culture and generating vastly more data.

More straightforward was the characterization of robust nuclear Sod1 expression in Kras escapees of all stain intensities; nuclear Sod1 localization has been shown to be critical for proliferation of Kras-driven NSCLC (X. Wang et al., 2021).

As an aside, Wang et al. (2021) also noted the presence of escapee tumors, but investigated neither differential Sod1 expression nor localization. Instead, escapees were simply grouped with $Sod1^{+/+}$ tumors for practicality. The data acquired from the current analysis would caution against grouping $Sod^{+/+}$ tumors and $Sod1^{L/L}$ escapees, given the apparent variation in Sod1 expression in escapees versus the robust, dual-locus expression of $Sod1^{+/+}$ tumors.

4.1.6 Escapee split image analysis suggests broadening the tumor microenvironment

Split image ROS analyses were expected to demonstrate a stark contrast between ROS levels of escapees and Sod1-null tumors. Rather than comparing results from different slides—necessarily introducing some level of stain variation—this analysis was based on two regions of the same image stained with identical conditions. Not only were there no significant ROS increases in Sod1-null regions, there were no discernable differences between the two regions of any split image analyzed. Given the possibility that technical or procedural limitations may obscure ROS differences in split image analyses, multiple tumors from each genotype were also subjected to ROS analyses. This provided much-needed perspective: though no ROS differences were evident in split images, $Kras^{LSL/+}$; $Sod1^{-/-}$ tumors *did* show a significant elevation in ROS *when analyzed in the context of a* $Sod1^{L/L}$ *lung section*. This suggests that tumor ROS levels are more strongly influenced by the Sod1 expression profile of the plurality of nearby tumors, rather than the internal composition of any one individual tumor. Indeed, when escapees were considered as a standalone category, values for 8-oxoG positivity match those of $Sod1^{-/-}$ tumors, rather than isogenic $Sod1^{+/+}$ tumors **(Figure S2b,** pink bars**)**. This comparison holds for both oncogenes.

Overall, it is posited that the realm of the 'tumor microenvironment' must encompass a greater region than simply a tumor's immediate surroundings, likely including secreted factors from other tumors and stromal cells, or even distant endocrine signaling. This concept has implications for similar murine oncological studies, stressing the importance of contextualizing research within a holistic, multisystem organism, and the potential pitfalls of too narrow a focus.

4.1.7 Immune involvement in Kras tumors is likely Kras-mediated

Broadening the TME would also support the inclusion of immune infiltrate as a dynamic tumor-external ROS-modulating entity. Macrophage secretion of pro-tumorigenic cytokines, and ROS-based biasing of T-cell differentiation have both been shown to influence tumor progression (Kennel & Greten, 2021; Kusano et al., 2019; Murray, 2017).

Increased immune involvement in Kras tumor models, regardless of Sod1 status, suggests a more complex, oncogene-based interplay between tumor tissue and immune cells. Oncogenic Kras mutation itself modulates expression of inflammatory factors: IL-6 activates pathways involved in ROS detoxification and cell survival (Hamarsheh et al., 2020; Y. Zhang, Yan, et al., 2013). IL-8 recruits endothelial cells and neutrophils. IL-17 supports angiogenesis and promotes Th17 differentiation and proliferation (Hamarsheh et al., 2020). CD47 promotes immune evasion by suppressing macrophage phagocytosis of cancer cells (Hu et al., 2023). This close relationship with the immune environment allows oncogenic Kras to uniquely prevent the proliferation of effective antitumor lymphocytes while encouraging inflammatory signaling to foster tumor growth.

Oncogenic $Braf^{V600E}$ has also been associated with upregulation of IL-6, to novel effect. Rather than bolstering tumor growth, IL-6-secreting $Braf^{V600E}$-mutant tumor cells undergo oncogene-induced senescence (OIS), which is reversed upon IL-6 depletion (Kuilman et al., 2008).

Generally, Braf immune system crosstalk is reduced as compared to oncogenic Kras. Patient data suggests that Braf-mutated lung tumors have similar immune profiles to Braf-WT lung tumors, with little apparent distinction between $Braf^{V600E}$ and non-V600E groups (H. Li et al., 2022). This reduction in relative importance of the immune landscape on the progression of Braf-driven lung tumors is mirrored by the relative absence of immune cells in Braf lungs, regardless of Sod1 status.

Given the importance of immune involvement in Kras-driven tumors, and the Sod1-dependent lifespan differential evidenced by Kras Kaplan-Meier analyses, the effect of Sod1 status on the immune environment may be of interest. Does tumor Sod1 status bias immune populations to favor one immune cell subtype over another? Within the context of Sod1-null tumors, do advanced tumors signal increased immune involvement, or does increased immune involvement generate more advanced tumors? Which tumor-derived secreted factors most affect the cellular makeup of the immune landscape? Also, in considering the more practical mechanical functions of the lung, to what degree does inflammation and immune infiltration impact the efficiency of gas exchange, and how potently does this effect organismal survival? Answering these questions will provide a clearer picture of the tumor microenvironment, underscoring the importance of the broader combination of immune and stromal cells, signaling components, and tissue remodeling inherent to cancer progression.

4.1.8 BPSod and KPSod cell lines demonstrate high Sod1 regulatory plasticity

The absence of true Sod1-null BPSod and KPSod cell lines mirrors *in vitro* results where Sod1 loss and cell death are inextricably linked (Blander et al., 2003; X. Wang et al., 2021; Watanabe et al., 2013). As all BPSod and KPSod clones genotyped positively for both the $Sod1^{Lox}$ and Sod1Δ alleles, it is not possible for Sod1 expression to have originated from more than one functional Sod1 gene. Whereas the Sod1 expression of Braf clone 1435-8 (~50% WT) is consistent

with expression from one Sod1 locus, the remaining 3 clones exhibit Sod1 expression exceeding 50% of WT levels, indicating the presence of significant upregulation of Sod1 expression. Not only does this suggest robust Sod1 haplosufficiency, it demonstrates that expression beyond WT levels is possible from a single locus, alluding to incredible transcriptional plasticity.

Additionally, Sod1 protein levels and cell growth rates show remarkable correlation. Supraphysiological Sod1 levels appear to correlate with heightened *in vitro* growth rate, linking Sod1 overexpression to amplified tumor growth and survival in an oncogene-independent manner (L. Gao et al., 2024). Similarly, parallel reductions of Sod1 protein levels and *in vitro* growth rate echo the induction of cell cycle arrest and apoptosis of Sod1-null cell lines (Glasauer et al., 2014; S. Liu et al., 2020b).

4.1.9 Critical implication: In vitro assays do not consistently recapitulate results from in vivo models of NSCLC

Impossible to ignore was the apparent incongruity between *in vitro* assays and *in vivo* experimental results. For example, $Sod1^{-/-}$ tumors driven by both oncogenes were capable of robust growth *in vivo*, yet consistently failed to thrive *in vitro* despite the oncogenic addition of p53 loss. This was also a clear point of differentiation between this current research and similar work represented in the literature: whereas *in vitro* and *in vivo* p53-null datasets generally aligned, results from *in vivo* p53-retaining mouse models and *in vitro* p53-null cells no longer pointed toward the same conclusions. Although this suggests that the *in vivo* model here described does have novel experimental utility, it is also no longer comparable to results from p53-null cell assays.

This difference must necessarily be taken into consideration. For example, measurements of ROS levels in Kras Sod1-null, p53-null tumor models done by Wang et al. (2021), were conducted exclusively *in vitro*, a system that does not appear sufficiently representative of *in situ* tumor

growth. This is consistent with the premise that the complex *in vivo* tumor microenvironment—comprised of hundreds of tumors, numerous tumor-supportive stromal cell types, immune infiltrate, and native lung cells, all constantly sending and responding to signals—is capable of supporting the growth and development of $Sod1^{-/-}$ tumors far beyond the capacity of *in vitro* conditions. To maintain physiological accuracy, *in vivo* conditions should be utilized whenever possible, especially for similar NSCLC models. Though painstaking, future research may aim to involve p53-retaining primary cells to more closely approximate the characteristics of these *in situ* tumors.

4.2 Implications

Overall, this work details tumor progression in unique models of Braf- and Kras-driven Sod1-null NSCLC characterized by p53 retention and robust *in vivo* growth despite Sod1 loss. This contrasts the literature based on p53-null models, which, both *in vitro* and *in vivo*, suggest an inevitable causal relationship between Sod1 loss and suppression of tumor growth.

Sod1-null Braf tumors are characterized by advanced growth, yet reduced oxidative damage, positing that WT Sod1 may paradoxically aggravate H_2O_2 toxicity in analogous $Sod1^{+/+}$ tumors. Sod1 localization in Braf escapees appears dependent on the magnitude of Sod1 expression, with low-expression escapees abolishing nuclear Sod1 localization, perhaps due to Sod1 misfolding. Reduced Sod1 protein expression in a BPSod cell line correlates with reduced growth rate.

Sod1-null Kras tumors are characterized by advanced growth *despite* increased oxidative damage, with p53 acting as a potential compensatory mechanism promoting survival during oxidative stress. Sod1 localization in escapee tumors is nuclear, a well-documented localization pattern in Kras-driven tumors. Heightened Sod1 expression in cultured KPSod cells correlates with elevated *in vitro* growth rate, and suggests a remarkable capacity for Sod1 upregulation from a single intact Sod1 locus.

Escapee analyses suggest the broadening of the tumor microenvironment to include not only directly proximate tissue, but long-range signaling from more distal regions of the lung. Whereas Braf samples are largely devoid of immune infiltrate, Kras samples exhibit extensive immune involvement, likely recruited by an altered cytokine profile characteristic of $Kras^{G12D}$ mutation.

Overall, this work suggests that Sod1 plays a critical role in Kras- and Braf-driven NSCLC, influencing organismal survival, modulating tumor growth, and displaying a capacity for remarkable regulatory plasticity, all of which may inspire additional investigations.

Appendix

Supplemental Figures

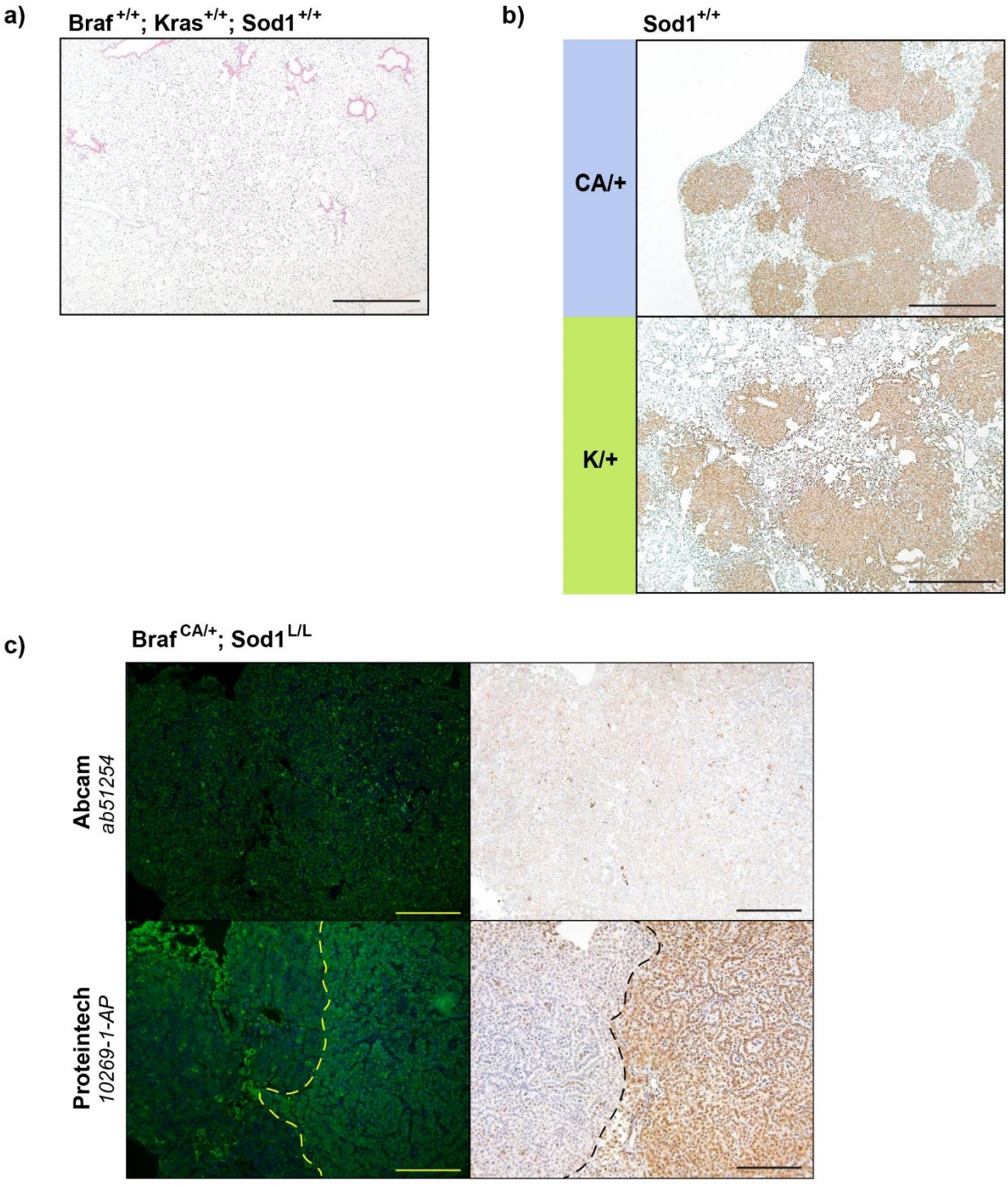

Figure S1- Confirmation of Sod1 expression in Sod1-WT tumors and escapees

(a) AdCre infection of a $Braf^{+/+}$; $Kras^{+/+}$; $Sod1^{+/+}$ wild-type mouse confirms an absence of tumors when no driver oncogenes are present. The virus has no off-target tumorigenic effects in the lungs. 50X magnification, scale bar = 1000µm. **(b)** $Braf^{CA/+}$ and $Kras^{LSL/+}$; $Sod1^{+/+}$ lung sections demonstrate uniform Sod1 staining across tumors of a lung section, with little variation. 50X magnification, scale bar = 1000µm. **(c)** Four serial sections stained with two Sod1 antibodies via immunofluorescence (left) and immunohistochemistry (right). Abcam *ab51254* does not suggest the presence of Sod1 stain in the escapee region via IF, nor via IHC. Proteintech *10269-1-AP* highlights a distinct delineation of Sod1-null (left of dashed line) and Sod1 escapee (right of dashed line) tumors via both IF and IHC. 200X magnification, scale bar = 200µm.

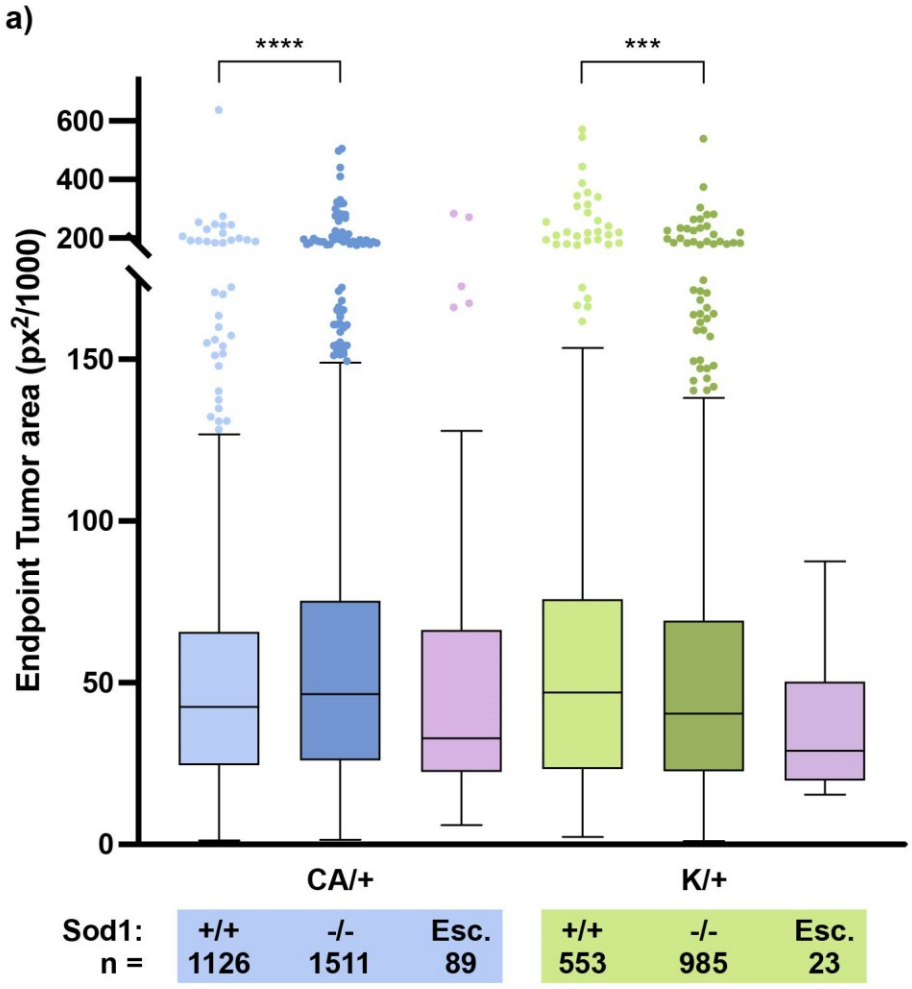
a)
****
***
600
400
200
150
100
50
0
Endpoint Tumor area (px²/1000)
CA/+
K/+
Sod1:
+/+
-/-
Esc.
+/+
-/-
Esc.
n =
1126
1511
89
553
985
23

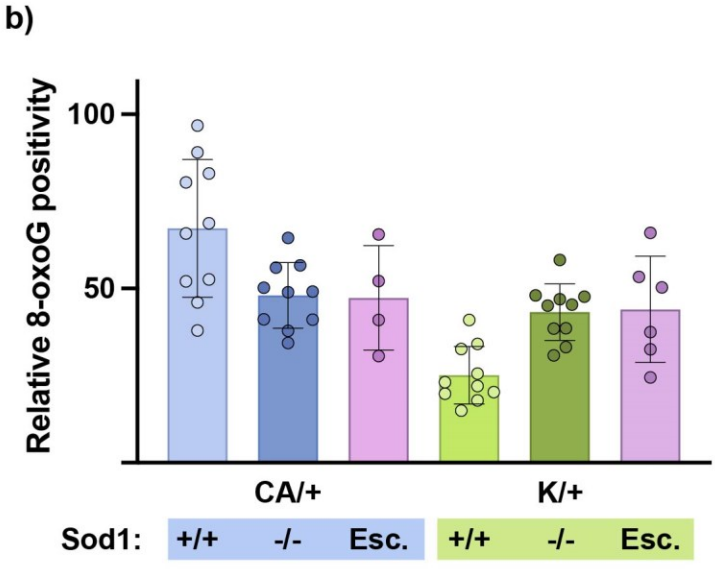
b)
100
50
Relative 8-oxoG positivity
CA/+
K/+
Sod1:
+/+
-/-
Esc.
+/+
-/-
Esc.

Figure S2- Escapee similarities to Sod1-WT, Sod1-null tumors

(a) Inclusion of escapees in measurements of individual tumor areas at endpoint. Escapees are insufficiently numerous to build a statistically robust dataset in comparison to the vast numbers of tumors available for non-escapee categories. **(b)** Expanded iteration of Figure 3.4a to include values measured in escapee tumors. 8-oxoG profiles of both $Braf^{CA/+}$ and $Kras^{LSL/+}$ escapees are analogous to $Sod1^{L/L}$ tumors, with which they share a tumor microenvironment, rather than $Sod1^{+/+}$ tumors, with which they share a genotype.

Supplemental Tables

Table 1: PCR Thermocycler parameters for genotyping mice and cultured cells

Time (min)	Temp. (°C)
05:00	94
Cycle A x 15 *Cycle B* x 20	
03:00	72
10:00	12

Time (min)	Temp. (°C)
Cycle A:	
00:30	94
00:30 (-1C/cycle)	65
01:30	72
Cycle B:	
00:30	94
00:30	55
01:30	72

Table 2: PCR Primer sequences and applications

Kras 1	GTCTTTCCCCAGCACAGTGC	Genotyping mice/cells
Kras 2	CTCTTGCCTACGCCACCAGCTC	Genotyping cells
Kras 3	AGCTAGCCACCATGGCTTGAGTAAGTCTGCA	Genotyping cells
DdKras 48	CTCTTGCCTACGCCACCAGC	Genotyping mice
DdKras 49	AGCTAGCCACCATGGCTTGA	Genotyping mice
Sod1 172	CTCCACAGGCAGTAGGACAA	Genotyping cells
Sod1 177	GTAGCATTTATTGAAGATGAAC	Genotyping mice
Sod1 185	GTGCTCTGAGAAGAGTCATA	Genotyping mice/cells
Braf 106	GGAAAGCCTGTCACGGGTC	Genotyping mice
Braf 107	CTTCCAAGCCTATGGGGG	Genotyping mice
p53 30	AAGGGGTATGAGGGACAAGG	Genotyping mice
p53 31	GAAGACAGAAAAGGGGAGGG	Genotyping mice/cells
P53 45	CACAAAAACAGGTTAAACCCAG	Genotyping cells

Table 3: Antibodies- working concentrations, sources, and catalogue numbers

4-HNE, Anti-4 Hydroxynonenal antibody [HNEJ-2]	IHC- 1:200	Abcam	ab48506
8-OHdG Polyclonal Antibody	IHC- 1:200	Bioss	bs-1278R
Alexa Fluor® 555 AffiniPure™ Donkey Anti-Rabbit IgG (H+L)	IF- 1:250	Jackson ImmunoResearch	711-565-152
alpha Tubulin Antibody (DM1A): sc-32293	WB- 1:500	Santa Cruz	sc-32293
DAPI	IF- 1:1000	Sigma	D9542
3-Nitrotyrosine Polyclonal Antibody	IHC- 1:200	Invitrogen	A-21285
SOD1 Polyclonal antibody	IF- 1:200 IHC- 1:200	Proteintech	10269-1-AP
Superoxide Dismutase 1 antibody	WB- 1:5,000 IF- 1:200 IHC- 1:200	Abcam	EP1727Y

Table 4: Materials- sources and catalogue numbers

ABC-HRP Kit, Peroxidase, VECTASTAIN® Elite® (Standard)	Vector	PK-6100
Acrylamide/Bis Solution, 30%	BioRad	1610158
Acrytol Mounting Media	Leica	3801720
Agarose, Low Melt Grade	BioShop	AGA101
Agarose, Molecular Biology Grade	FroggaBio	A87-500G
Albumin, Bovine Serum, Heat Shock Isolation, Fraction V	BioShop	ALB001.250
Autoradiography film, Blu-Lite, Western blotting, 8 x 10in	Diamed	DIAFILM810
Avertin (2,2,2-Tribromoethanol)	Sigma	T48402-5G
BCA Protein Assay Kit, Pierce™	ThermoFisher	23227
BLUelf Prestained Protein Ladder, 3.5-245 kDa	GeneDireX	PM008-0500
CaCl2, Calcium chloride	ACP	C0360-500G

Cell Culture treated dishes, 10cm	Fisher	12-556-002
Cell Strainer, Falcon™ 40µm	Fisher	08-771-1
Cell Strainer, Falcon™ 70µm	Fisher	08-771-2
DAB Substrate Kit	Biotium	30015
DMEM 1X with 4.5 g/L Glucose, L-Glutamine & Sodium Pyruvate	Wisent	319-005 CL
ECL Western blotting detection reagents, Cytiva	Sigma	GERPN2209
EDTA, Disodium salt, Dihydrate	BioBasic	EB0185
EGTA, Ultra Pure, min.98%	BioShop	EGT101
Eosin Y Solution, Alcoholic	Sigma	HT110180
FBS	Gibco	12483020
Formalin 10%, VWR®, Reagent Grade for histology, neutral buffered.	VWR	16004-126
Gel Documentation System, Axygen®	Axygen	GDBL-1000
Genomic DNA Purification Kit, Wizard®	Promega	A1120
Glycerol (Certified ACS)	Fisher	G33-4
Glycine	BioBasic	GB0235
H2O2, Hydrogen peroxide, 30%	ACP	H7000
HCl, Hydrochloric acid	ACP	H6100-500ML
Hematoxylin, Harris acidified Hystological/Cytological stains	Fisher	23-245678
HEPES, Biotechnology Grade. Min.99.5%	BioShop	HEP001
Kanamycin sulfate	Bio Basic	KB0286
Lung Dissociation Kit, mouse	Miltenyi Biotec	130-095-927
MgCl2, Magnesium chloride hexahydrate	Sigma	M2670
Microscope, Leica DM4000 B, Transmitted light/Fluorescence	Leica	Archived
Minimum Essential Medium, Eagle's	Sigma	M0268-1L

$Na_3C_6H_5O_7$, Sodium citrate	ACP	S2990-500g
$Na_4P_2O_7.10H_2O$, Sodium pyrophosphate, Decahydrate	BioShop	SPP310
NaCl, Sodium chloride, Reagent Grade, min 99%	BioShop	SOD002
Needle, 1/2 in. single use, sterile	BD	305111
PAP Pen, Regular, tip 1/5" diameter	Cedarlane	MU12-A
Penicillin-Streptomycin 100X	Wisent	450-201 ZL
ProLong™ Gold Antifade Mountant, Invitrogen™	Invitrogen	P36934
PVDF Membrane, Immun-Blot, 26cm x 3.3m	BioRad	1620177
RPMI 1640 1X with L-Glutamine & Sodium Bicarbonate	Wisent	350-000 CS
SDS, Sodium dodecyl sulfate, electrophoresis grade	BioShop	SDS001
Slides, Microscope, Fisherbrand™ Superfrost™ Plus	ThermoFisher	22-037-246
Syringe, Luer Slip Tip, sterile, single use, 1 mL	BD	309659
Taq DNA Polymerase	FroggaBio	MB101-0500
Tert-amyl alcohol (2-Methyl-2-butanol)	Sigma	152463-250ML
Thick Blot Filter Paper, 7.5 x 10cm	BioRad	1703932
Trans-Blot® SD Semi-Dry Transfer Cell	BioRad	1703848
TRIS, Tris(hydroxymethyl)aminomethane (Trometamol), ultrapure	VWR	97061-794
Triton™ X-100	Sigma-Aldrich	X100-100ML
Trypsin, 0.25%, 0.1 % EDTA, 1X, w/o $NaHCO_3$	Wisent	325-045 EL
Tubes, 15mL, 50mL Conical	Froggabio	TB15-500; TB50-500
Tubes, 5mL Screw-cap	Ultident	48-C2545
Xylene	BioBasic	XC9800
Zinc Formalin Fixative	Sigma	Z2902

Table 5: Solution compositions

Tris-ETDA Avertin diluent	1M Tris, 0.5M EDTA, 5M NaCl
1x PBS	8g NaCl, 0.20g KCl, 1.15g $Na_2HPO_4 \cdot 7H_2O$, 0.24g KH_2PO_4 Bring to 900mL with ddH2O and pH to 7.2 before bringing the volume to 1000mL with ddH2O
1x PBS-T	Prepare 1x PBS to 995mL ddH20 before adding 5mL 10% Tween-20
1x TBS	8.7g NaCl, 2.4g Tris-HCl Bring to 1000mL with ddH2O
1x TBS-T	Prepare 1x TBS to 995mL ddH20 before adding 5mL 10% Tween-20
PLCγ Lysis buffer	50mM Hepes [pH 7.5], 150mM NaCl, 10% glycerol, 1% TritonX-100, 1mM EGTA, 1.5mM MgCl2, 10mM $Na_4P_2O_7$
15% Separating polyacrylamide gel	7.5mL 30% Bis-acrylamide, 3.75mL Lower Tris, 105µL 10% APS, 36µL TEMED, 3.75mL ddH_2O
4% Stacking polyacrylamide gel	1.05mL 30% Bis-acrylamide, 1.875mL Upper Tris, 52.5µL 10% APS, 18µL TEMED, 4.5mL ddH_2O
Lower Tris	92g Tris, 10mL 20% SDS Bring to 500mL with ddH20; pH to 8.8
Upper Tris	6g Tris, 2mL 20% SDS Bring to 100mL with ddH2O; pH to 6.8
10X SDS running buffer	120g Tris, 577.2g glycine, 40g SDS Bring to 4L with ddH2O
Transfer buffer	9g Tris, 43.23g glycine, 500mL methanol Bring to 3L with ddH2O
4X Laemmli buffer	10mL Tris [1M, pH6.8], 4g SDS, 20mL glycerol, 0.1g Bromophenol blue, 10mL B mercaptoethanol Bring to 50mL with ddH2O
2X SDS loading buffer	25mL 4X Tris HCl/SDS pH6.8, 20mL 100% glycerol, 4g SDS, 1mg bromophenol blue Bring to 100mL with ddH2O Before use, add 60µL B mercaptoethanol for each 1mL of loading buffer.

Works Cited

Adderley, H., Blackhall, F. H., & Lindsay, C. R. (2019). KRAS-mutant non-small cell lung cancer: Converging small molecules and immune checkpoint inhibition. *eBioMedicine*, *41*, 711–716. https://doi.org/10.1016/j.ebiom.2019.02.049

Aggarwal, V., Tuli, H. S., Varol, A., Thakral, F., Yerer, M. B., Sak, K., Varol, M., Jain, A., Khan, Md. A., & Sethi, G. (2019). Role of Reactive Oxygen Species in Cancer Progression: Molecular Mechanisms and Recent Advancements. *Biomolecules*, *9*(11), 735. https://doi.org/10.3390/biom9110735

Aguirre, E., & Cadenas, S. (2010). GDP and carboxyatractylate inhibit 4-hydroxynonenal-activated proton conductance to differing degrees in mitochondria from skeletal muscle and heart. *Biochimica Et Biophysica Acta*, *1797*(10), 1716–1726. https://doi.org/10.1016/j.bbabio.2010.06.009

Ahmad, A., Dempsey, S. K., Daneva, Z., Azam, M., Li, N., Li, P.-L., & Ritter, J. K. (2018). Role of Nitric Oxide in the Cardiovascular and Renal Systems. *International Journal of Molecular Sciences*, *19*(9), 2605. https://doi.org/10.3390/ijms19092605

Ambruso, D. R., Cusack, N., & Thurman, G. (2004). NADPH oxidase activity of neutrophil specific granules: Requirements for cytosolic components and evidence of assembly during cell activation. *Molecular Genetics and Metabolism*, *81*(4), 313–321. https://doi.org/10.1016/j.ymgme.2004.01.009

Anderson, N. M., & Simon, M. C. (2020). The tumor microenvironment. *Current Biology*, *30*(16), R921–R925. https://doi.org/10.1016/j.cub.2020.06.081

Ansary, T. M., Hossain, Md. R., Kamiya, K., Komine, M., & Ohtsuki, M. (2021). Inflammatory Molecules Associated with Ultraviolet Radiation-Mediated Skin Aging. *International Journal of Molecular Sciences*, *22*(8), 3974. https://doi.org/10.3390/ijms22083974

Arbour, K. C., Jordan, E., Kim, H. R., Dienstag, J., Yu, H. A., Sanchez-Vega, F., Lito, P., Berger, M., Solit, D. B., Hellmann, M., Kris, M. G., Rudin, C. M., Ni, A., Arcila, M., Ladanyi, M., & Riely, G. J. (2018). Effects of co-occurring genomic alterations on outcomes

in patients with KRAS-mutant non-small cell lung cancer. *Clinical Cancer Research : An Official Journal of the American Association for Cancer Research*, *24*(2), 334–340. https://doi.org/10.1158/1078-0432.CCR-17-1841

Babior, B. M., Kipnes, R. S., & Curnutte, J. T. (1973). Biological Defense Mechanisms. THE PRODUCTION BY LEUKOCYTES OF SUPEROXIDE, A POTENTIAL BACTERICIDAL AGENT. *The Journal of Clinical Investigation*, *52*(3), 741–744. https://doi.org/10.1172/JCI107236

Bae, T., Hallis, S. P., & Kwak, M.-K. (2024). Hypoxia, oxidative stress, and the interplay of HIFs and NRF2 signaling in cancer. *Experimental & Molecular Medicine*, *56*(3), 501–514. https://doi.org/10.1038/s12276-024-01180-8

Bafana, A., Dutt, S., Kumar, A., Kumar, S., & Ahuja, P. S. (2011). The basic and applied aspects of superoxide dismutase. *Journal of Molecular Catalysis B: Enzymatic*, *68*(2), 129–138. https://doi.org/10.1016/j.molcatb.2010.11.007

Bahrampour, N., Shiraseb, F., Noori, S., Clark, C. C. T., & Mirzaei, K. (2022). Is there any putative mediatory role of inflammatory markers on the association between ultra-processed foods and resting metabolic rate? *Frontiers in Nutrition*, *9*, 932225. https://doi.org/10.3389/fnut.2022.932225

Bandookwala, M., & Sengupta, P. (2020). 3-Nitrotyrosine: A versatile oxidative stress biomarker for major neurodegenerative diseases. *The International Journal of Neuroscience*, *130*(10), 1047–1062. https://doi.org/10.1080/00207454.2020.1713776

Battelli, M. G., Polito, L., Bortolotti, M., & Bolognesi, A. (2016). Xanthine Oxidoreductase-Derived Reactive Species: Physiological and Pathological Effects. *Oxidative Medicine and Cellular Longevity*, *2016*(1), 3527579. https://doi.org/10.1155/2016/3527579

Beak, S. M., Lee, Y. S., & Kim, J.-A. (2004). NADPH oxidase and cyclooxygenase mediate the ultraviolet B-induced generation of reactive oxygen species and activation of nuclear factor-κB in HaCaT human keratinocytes. *Biochimie*, *86*(7), 425–429. https://doi.org/10.1016/j.biochi.2004.06.010

Bedard, K., & Krause, K.-H. (2007). The NOX Family of ROS-Generating NADPH Oxidases: Physiology and Pathophysiology. *Physiological Reviews*, *87*(1), 245–313. https://doi.org/10.1152/physrev.00044.2005

Benatar, M., Macklin, E. A., Malaspina, A., Rogers, M.-L., Hornstein, E., Lombardi, V., Renfrey, D., Shepheard, S., Magen, I., Cohen, Y., Granit, V., Statland, J. M., Heckmann, J. M., Rademakers, R., McHutchison, C. A., Petrucelli, L., McMillan, C. T., Wuu, J., Benatar, M., … So, Y. (2024). Prognostic clinical and biological markers for amyotrophic lateral sclerosis disease progression: Validation and implications for clinical trial design and analysis. *eBioMedicine*, *108*. https://doi.org/10.1016/j.ebiom.2024.105323

Berdyński, M., Miszta, P., Safranow, K., Andersen, P. M., Morita, M., Filipek, S., Żekanowski, C., & Kuźma-Kozakiewicz, M. (2022). SOD1 mutations associated with amyotrophic lateral sclerosis analysis of variant severity. *Scientific Reports*, *12*(1), 103. https://doi.org/10.1038/s41598-021-03891-8

Berman-Riu, M., Cunill, V., Clemente, A., López-Gómez, A., Pons, J., & Ferrer, J. M. (2024). Dysfunctional mitochondria, disrupted levels of reactive oxygen species, and autophagy in B cells from common variable immunodeficiency patients. *Frontiers in Immunology*, *15*. https://doi.org/10.3389/fimmu.2024.1362995

Berry, C. E., & Hare, J. M. (2004). Xanthine oxidoreductase and cardiovascular disease: Molecular mechanisms and pathophysiological implications. *The Journal of Physiology*, *555*(3), 589–606. https://doi.org/10.1113/jphysiol.2003.055913

Bhatti, J. S., Bhatti, G. K., & Reddy, P. H. (2017). Mitochondrial dysfunction and oxidative stress in metabolic disorders—A step towards mitochondria based therapeutic strategies. *Biochimica et Biophysica Acta (BBA) - Molecular Basis of Disease*, *1863*(5), 1066–1077. https://doi.org/10.1016/j.bbadis.2016.11.010

Blander, G., de Oliveira, R. M., Conboy, C. M., Haigis, M., & Guarente, L. (2003). Superoxide Dismutase 1 Knock-down Induces Senescence in Human Fibroblasts*. *Journal of Biological Chemistry*, *278*(40), 38966–38969. https://doi.org/10.1074/jbc.M307146200

Braicu, C., Buse, M., Busuioc, C., Drula, R., Gulei, D., Raduly, L., Rusu, A., Irimie, A., Atanasov, A. G., Slaby, O., Ionescu, C., & Berindan-Neagoe, I. (2019). A Comprehensive Review on MAPK: A Promising Therapeutic Target in Cancer. *Cancers*, *11*(10), 1618. https://doi.org/10.3390/cancers11101618

Brentnall, M., Rodriguez-Menocal, L., De Guevara, R. L., Cepero, E., & Boise, L. H. (2013). Caspase-9, caspase-3 and caspase-7 have distinct roles during intrinsic apoptosis. *BMC Cell Biology*, *14*(1), 32. https://doi.org/10.1186/1471-2121-14-32

Broxton, C. N., & Culotta, V. C. (2016). SOD Enzymes and Microbial Pathogens: Surviving the Oxidative Storm of Infection. *PLOS Pathogens*, *12*(1), e1005295. https://doi.org/10.1371/journal.ppat.1005295

Cairns, R. A., Harris, I. S., & Mak, T. W. (2011). Regulation of cancer cell metabolism. *Nature Reviews Cancer*, *11*(2), Article 2. https://doi.org/10.1038/nrc2981

Campisi, J., & d'Adda di Fagagna, F. (2007). Cellular senescence: When bad things happen to good cells. *Nature Reviews Molecular Cell Biology*, *8*(9), 729–740. https://doi.org/10.1038/nrm2233

Castro, J. P., Jung, T., Grune, T., & Siems, W. (2017). 4-Hydroxynonenal (HNE) modified proteins in metabolic diseases. *Free Radical Biology & Medicine*, *111*, 309–315. https://doi.org/10.1016/j.freeradbiomed.2016.10.497

Chang, C.-H., Qiu, J., O'Sullivan, D., Buck, M. D., Noguchi, T., Curtis, J. D., Chen, Q., Gindin, M., Gubin, M. M., van der Windt, G. J. W., Tonc, E., Schreiber, R. D., Pearce, E. J., & Pearce, E. L. (2015). Metabolic Competition in the Tumor Microenvironment Is a Driver of Cancer Progression. *Cell*, *162*(6), 1229–1241. https://doi.org/10.1016/j.cell.2015.08.016

Che, M., Wang, R., Li, X., Wang, H.-Y., & Zheng, X. F. S. (2016). Expanding roles of superoxide dismutases in cell regulation and cancer. *Drug Discovery Today*, *21*(1), Article 1. https://doi.org/10.1016/j.drudis.2015.10.001

Chen, H., Lu, M., Lyu, Q., Shi, L., Zhou, C., Li, M., Feng, S., Liang, X., Zhou, X., & Ren, L. (2024). Mitochondrial dynamics dysfunction: Unraveling the hidden link to depression.

Biomedicine & Pharmacotherapy, *175*, 116656. https://doi.org/10.1016/j.biopha.2024.116656

Chen, T., Ashwood, L. M., Kondrashova, O., Strasser, A., Kelly, G., & Sutherland, K. D. (2024). Breathing new insights into the role of mutant p53 in lung cancer. *Oncogene*, 1–15. https://doi.org/10.1038/s41388-024-03219-6

Chen, T., Ashwood, L. M., Kondrashova, O., Strasser, A., Kelly, G., & Sutherland, K. D. (2025). Breathing new insights into the role of mutant p53 in lung cancer. *Oncogene*, *44*(3), 115–129. https://doi.org/10.1038/s41388-024-03219-6

Chen, Z., Han, F., Du, Y., Shi, H., & Zhou, W. (2023). Hypoxic microenvironment in cancer: Molecular mechanisms and therapeutic interventions. *Signal Transduction and Targeted Therapy*, *8*(1), 1–23. https://doi.org/10.1038/s41392-023-01332-8

Cisowski, J., Sayin, V. I., Liu, M., Karlsson, C., & Bergo, M. O. (2016). Oncogene-induced senescence underlies the mutual exclusive nature of oncogenic KRAS and BRAF. *Oncogene*, *35*(10), Article 10. https://doi.org/10.1038/onc.2015.186

Cognet, G., & Muir, A. (2024). Identifying metabolic limitations in the tumor microenvironment. *Science Advances*, *10*(40), eadq7305. https://doi.org/10.1126/sciadv.adq7305

Coppola, S., Paparo, L., Trinchese, G., Rivieri, A. M., Masino, A., De Giovanni Di Santa Severina, A. F., Cerulo, M., Escolino, M., Turco, A., Esposito, C., Mollica, M. P., & Berni Canani, R. (2023). Increased dietary intake of ultraprocessed foods and mitochondrial metabolism alterations in pediatric obesity. *Scientific Reports*, *13*, 12609. https://doi.org/10.1038/s41598-023-39566-9

Cordani, M., Butera, G., Pacchiana, R., Masetto, F., Mullappilly, N., Riganti, C., & Donadelli, M. (2020). Mutant p53-Associated Molecular Mechanisms of ROS Regulation in Cancer Cells. *Biomolecules*, *10*(3), 361. https://doi.org/10.3390/biom10030361

Cowled, P., & Fitridge, R. (2011). Pathophysiology of Reperfusion Injury. In R. Fitridge & M. Thompson (Eds.), *Mechanisms of Vascular Disease: A Reference Book for Vascular Specialists*. University of Adelaide Press. http://www.ncbi.nlm.nih.gov/books/NBK534267/

Cruz-Garcia, D., Brouwers, N., Duran, J. M., Mora, G., Curwin, A. J., & Malhotra, V. (2017). A diacidic motif determines unconventional secretion of wild-type and ALS-linked mutant SOD1. *Journal of Cell Biology*, *216*(9), 2691–2700. https://doi.org/10.1083/jcb.201704056

Dankner, M., Rose, A. A. N., Rajkumar, S., Siegel, P. M., & Watson, I. R. (2018). Classifying BRAF alterations in cancer: New rational therapeutic strategies for actionable mutations. *Oncogene*, *37*(24), 3183–3199. https://doi.org/10.1038/s41388-018-0171-x

Dankort, D., Filenova, E., Collado, M., Serrano, M., Jones, K., & McMahon, M. (2007). A new mouse model to explore the initiation, progression, and therapy of BRAFV600E-induced lung tumors. *Genes & Development*, *21*(4), 379–384. https://doi.org/10.1101/gad.1516407

de Almeida, A. J. P. O., de Oliveira, J. C. P. L., da Silva Pontes, L. V., de Souza Júnior, J. F., Gonçalves, T. A. F., Dantas, S. H., de Almeida Feitosa, M. S., Silva, A. O., & de Medeiros, I. A. (2022). ROS: Basic Concepts, Sources, Cellular Signaling, and its Implications in Aging Pathways. *Oxidative Medicine and Cellular Longevity*, *2022*, 1225578. https://doi.org/10.1155/2022/1225578

de Jager, T. L., Cockrell, A. E., & Du Plessis, S. S. (2017). Ultraviolet Light Induced Generation of Reactive Oxygen Species. In S. I. Ahmad (Ed.), *Ultraviolet Light in Human Health, Diseases and Environment* (pp. 15–23). Springer International Publishing. https://doi.org/10.1007/978-3-319-56017-5_2

DeNicola, G. M., Karreth, F. A., Humpton, T. J., Gopinathan, A., Wei, C., Frese, K., Mangal, D., Yu, K. H., Yeo, C. J., Calhoun, E. S., Scrimieri, F., Winter, J. M., Hruban, R. H., Iacobuzio-Donahue, C., Kern, S. E., Blair, I. A., & Tuveson, D. A. (2011). Oncogene-induced Nrf2 transcription promotes ROS detoxification and tumorigenesis. *Nature*, *475*(7354), 106–109. https://doi.org/10.1038/nature10189

Desideri, E., Cavallo, A. L., & Baccarini, M. (2015). Alike but Different: RAF Paralogs and Their Signaling Outputs. *Cell*, *161*(5), 967–970. https://doi.org/10.1016/j.cell.2015.04.045

Echtay, K. S., Roussel, D., St-Pierre, J., Jekabsons, M. B., Cadenas, S., Stuart, J. A., Harper, J. A., Roebuck, S. J., Morrison, A., Pickering, S., Clapham, J. C., & Brand, M. D. (2002).

Superoxide activates mitochondrial uncoupling proteins. *Nature*, *415*(6867), 96–99. https://doi.org/10.1038/415096a

El Tekle, G., Bernasocchi, T., Unni, A. M., Bertoni, F., Rossi, D., Rubin, M. A., & Theurillat, J.-P. (2021). Co-occurrence and mutual exclusivity: What cross-cancer mutation patterns can tell us. *Trends in Cancer*, *7*(9), 823–836. https://doi.org/10.1016/j.trecan.2021.04.009

Eleutherio, E. C. A., Silva Magalhães, R. S., de Araújo Brasil, A., Monteiro Neto, J. R., & de Holanda Paranhos, L. (2021). SOD1, more than just an antioxidant. *Archives of Biochemistry and Biophysics*, *697*, 108701. https://doi.org/10.1016/j.abb.2020.108701

Eniafe, J., & Jiang, S. (2021). The functional roles of TCA cycle metabolites in cancer. *Oncogene*, *40*(19), 3351–3363. https://doi.org/10.1038/s41388-020-01639-8

Fasbender, A., Lee, J. H., Walters, R. W., Moninger, T. O., Zabner, J., & Welsh, M. J. (1998). Incorporation of adenovirus in calcium phosphate precipitates enhances gene transfer to airway epithelia in vitro and in vivo. *Journal of Clinical Investigation*, *102*(1), 184–193.

Ferrari, R. S., & Andrade, C. F. (2015). Oxidative Stress and Lung Ischemia-Reperfusion Injury. *Oxidative Medicine and Cellular Longevity*, *2015*(1), 590987. https://doi.org/10.1155/2015/590987

Finkel, T. (2011). Signal transduction by reactive oxygen species. *Journal of Cell Biology*, *194*(1), Article 1. https://doi.org/10.1083/jcb.201102095

Fischer, L. R., Igoudjil, A., Magrané, J., Li, Y., Hansen, J. M., Manfredi, G., & Glass, J. D. (2011). SOD1 targeted to the mitochondrial intermembrane space prevents motor neuropathy in the Sod1 knockout mouse. *Brain*, *134*(1), 196–209. https://doi.org/10.1093/brain/awq314

Frazier, T. H., DiBaise, J. K., & McClain, C. J. (2011). Gut Microbiota, Intestinal Permeability, Obesity-Induced Inflammation, and Liver Injury. *Journal of Parenteral and Enteral Nutrition*, *35*(5S), 14S-20S. https://doi.org/10.1177/0148607111413772

Friedmann Angeli, J. P., & Meierjohann, S. (2021). NRF2-dependent stress defense in tumor antioxidant control and immune evasion. *Pigment Cell & Melanoma Research*, *34*(2), 268–279. https://doi.org/10.1111/pcmr.12946

Gao, G., Liao, W., Ma, Q., Zhang, B., Chen, Y., & Wang, Y. (2020). KRAS G12D mutation predicts lower TMB and drives immune suppression in lung adenocarcinoma. *Lung Cancer*, *149*, 41–45. https://doi.org/10.1016/j.lungcan.2020.09.004

Gao, L., Wang, W., Ma, H., Yin, M., Yang, X., Han, R., Ohara, S., Kim, D., & Wang, G. (2024). Bioinformatics analysis reveals SOD1 is a prognostic factor in lung adenocarcinoma. *Translational Cancer Research*, *13*(10), 5522–5534. https://doi.org/10.21037/tcr-24-1400

García-Jiménez, C., & Goding, C. R. (2019). Starvation and pseudo-starvation as drivers of cancer metastasis through translation reprogramming. *Cell Metabolism*, *29*(2), 254–267. https://doi.org/10.1016/j.cmet.2018.11.018

Garnett, M. J., Rana, S., Paterson, H., Barford, D., & Marais, R. (2005). Wild-Type and Mutant B-RAF Activate C-RAF through Distinct Mechanisms Involving Heterodimerization. *Molecular Cell*, *20*(6), 963–969. https://doi.org/10.1016/j.molcel.2005.10.022

Gasparovic, A. C., Milkovic, L., Sunjic, S. B., & Zarkovic, N. (2017). Cancer growth regulation by 4-hydroxynonenal. *Free Radical Biology & Medicine*, *111*, 226–234. https://doi.org/10.1016/j.freeradbiomed.2017.01.030

Ge, M., Papagiannakopoulos, T., & Bar-Peled, L. (2024). Reductive stress in cancer: Coming out of the shadows. *Trends in Cancer*, *10*(2), 103–112. https://doi.org/10.1016/j.trecan.2023.10.002

Gęgotek, A., Nikliński, J., Žarković, N., Žarković, K., Waeg, G., Łuczaj, W., Charkiewicz, R., & Skrzydlewska, E. (2016). Lipid mediators involved in the oxidative stress and antioxidant defence of human lung cancer cells. *Redox Biology*, *9*, 210–219. https://doi.org/10.1016/j.redox.2016.08.010

Getzoff, E. D., Tainer, J. A., Weiner, P. K., Kollman, P. A., Richardson, J. S., & Richardson, D. C. (1983). Electrostatic recognition between superoxide and copper, zinc superoxide dismutase. *Nature*, *306*(5940), 287–290. https://doi.org/10.1038/306287a0

Gibbings, S., Elkins, N. D., Fitzgerald, H., Tiao, J., Weyman, M. E., Shibao, G., Fini, M. A., & Wright, R. M. (2011). Xanthine Oxidoreductase Promotes the Inflammatory State of Mononuclear Phagocytes through Effects on Chemokine Expression, Peroxisome Proliferator-activated Receptor-γ Sumoylation, and HIF-1α. *The Journal of Biological Chemistry*, *286*(2), 961–975. https://doi.org/10.1074/jbc.M110.150847

Glasauer, A., Sena, L. A., Diebold, L. P., Mazar, A. P., & Chandel, N. S. (2014). Targeting SOD1 reduces experimental non–small-cell lung cancer. *The Journal of Clinical Investigation*, *124*(1), Article 1. https://doi.org/10.1172/JCI71714

Glaviano, A., Foo, A. S. C., Lam, H. Y., Yap, K. C. H., Jacot, W., Jones, R. H., Eng, H., Nair, M. G., Makvandi, P., Geoerger, B., Kulke, M. H., Baird, R. D., Prabhu, J. S., Carbone, D., Pecoraro, C., Teh, D. B. L., Sethi, G., Cavalieri, V., Lin, K. H., … Kumar, A. P. (2023). PI3K/AKT/mTOR signaling transduction pathway and targeted therapies in cancer. *Molecular Cancer*, *22*(1), 138. https://doi.org/10.1186/s12943-023-01827-6

Goldsteins, G., Keksa-Goldsteine, V., Ahtoniemi, T., Jaronen, M., Arens, E., Åkerman, K., Chan, P. H., & Koistinaho, J. (2008). Deleterious Role of Superoxide Dismutase in the Mitochondrial Intermembrane Space*. *Journal of Biological Chemistry*, *283*(13), 8446–8452. https://doi.org/10.1074/jbc.M706111200

Gosset, P., Camu, W., Raoul, C., & Mezghrani, A. (2022). Prionoids in amyotrophic lateral sclerosis. *Brain Communications*, *4*(3), fcac145. https://doi.org/10.1093/braincomms/fcac145

Grad, L. I., Yerbury, J. J., Turner, B. J., Guest, W. C., Pokrishevsky, E., O'Neill, M. A., Yanai, A., Silverman, J. M., Zeineddine, R., Corcoran, L., Kumita, J. R., Luheshi, L. M., Yousefi, M., Coleman, B. M., Hill, A. F., Plotkin, S. S., Mackenzie, I. R., & Cashman, N. R. (2014). Intercellular propagated misfolding of wild-type Cu/Zn superoxide dismutase occurs via exosome-dependent and -independent mechanisms. *Proceedings of the National Academy of Sciences*, *111*(9), 3620–3625. https://doi.org/10.1073/pnas.1312245111

Gülow, K., Tümen, D., Heumann, P., Schmid, S., Kandulski, A., Müller, M., & Kunst, C. (2024). Unraveling the Role of Reactive Oxygen Species in T Lymphocyte Signaling. *International Journal of Molecular Sciences*, *25*(11), Article 11. https://doi.org/10.3390/ijms25116114

Guo, Y.-J., Pan, W.-W., Liu, S.-B., Shen, Z.-F., Xu, Y., & Hu, L.-L. (2020). ERK/MAPK signalling pathway and tumorigenesis (Review). *Experimental and Therapeutic Medicine*, *19*(3), 1997–2007. https://doi.org/10.3892/etm.2020.8454

Halliwell, B., & Gutteridge, J. M. C. (2015). Oxygen: Boon yet bane—introducing oxygen toxicity and reactive species. In B. Halliwell & J. M. C. Gutteridge (Eds.), *Free Radicals in Biology and Medicine* (p. 0). Oxford University Press. https://doi.org/10.1093/acprof:oso/9780198717478.003.0001

Hamarsheh, S., Groß, O., Brummer, T., & Zeiser, R. (2020). Immune modulatory effects of oncogenic KRAS in cancer. *Nature Communications*, *11*(1), 5439. https://doi.org/10.1038/s41467-020-19288-6

Harlan, T. S., Gow, R. V., Kornstädt, A., Alderson, P. W., & Lustig, R. H. (2023). The Metabolic Matrix: Re-engineering ultraprocessed foods to feed the gut, protect the liver, and support the brain. *Frontiers in Nutrition*, *10*, 1098453. https://doi.org/10.3389/fnut.2023.1098453

Heck, D. E., Vetrano, A. M., Mariano, T. M., & Laskin, J. D. (2003). UVB Light Stimulates Production of Reactive Oxygen Species: UNEXPECTED ROLE FOR CATALASE *. *Journal of Biological Chemistry*, *278*(25), 22432–22436. https://doi.org/10.1074/jbc.C300048200

Henry, T. R., & Wallace, K. B. (1995). The Role of Redox Cycling versus Arylation in Quinone-Induced Mitochondrial Dysfunction: A Mechanistic Approach in Classifying Reactive Toxicants. *SAR and QSAR in Environmental Research*, *4*(2–3), 97–108. https://doi.org/10.1080/10629369508029907

Hobbs, G. A., Der, C. J., & Rossman, K. L. (2016). RAS isoforms and mutations in cancer at a glance. *Journal of Cell Science*, *129*(7), 1287–1292. https://doi.org/10.1242/jcs.182873

Hohn, D. C., & Lehrer, R. I. (1975). NADPH oxidase deficiency in X-linked chronic granulomatous disease. *The Journal of Clinical Investigation*, *55*(4), 707–713. https://doi.org/10.1172/JCI107980

Hosonuma, M., & Yoshimura, K. (2023). Association between pH regulation of the tumor microenvironment and immunological state. *Frontiers in Oncology*, *13*, 1175563. https://doi.org/10.3389/fonc.2023.1175563

Hrycay, E. G., & Bandiera, S. M. (2015). Chapter Two—Involvement of Cytochrome P450 in Reactive Oxygen Species Formation and Cancer. In J. P. Hardwick (Ed.), *Advances in Pharmacology* (Vol. 74, pp. 35–84). Academic Press. https://doi.org/10.1016/bs.apha.2015.03.003

Hu, H., Cheng, R., Wang, Y., Wang, X., Wu, J., Kong, Y., Zhan, S., Zhou, Z., Zhu, H., Yu, R., Liang, G., Wang, Q., Zhu, X., Zhang, C.-Y., Yin, R., Yan, C., & Chen, X. (2023). Oncogenic KRAS signaling drives evasion of innate immune surveillance in lung adenocarcinoma by activating CD47. *The Journal of Clinical Investigation*, *133*(2), e153470. https://doi.org/10.1172/JCI153470

Huang, L., Guo, Z., Wang, F., & Fu, L. (2021). KRAS mutation: From undruggable to druggable in cancer. *Signal Transduction and Targeted Therapy*, *6*(1), 1–20. https://doi.org/10.1038/s41392-021-00780-4

Huang, M.-F., Lin, W.-L., & Ma, Y.-C. (2005). A study of reactive oxygen species in mainstream of cigaretteAbstract. *Indoor Air*, *15*(2), 135–140. https://doi.org/10.1111/j.1600-0668.2005.00330.x

Iuchi, Y., Roy, D., Okada, F., Kibe, N., Tsunoda, S., Suzuki, S., Takahashi, M., Yokoyama, H., Yoshitake, J., Kondo, S., & Fujii, J. (2010). Spontaneous skin damage and delayed wound healing in SOD1-deficient mice. *Molecular and Cellular Biochemistry*, *341*(1–2), 181–194. https://doi.org/10.1007/s11010-010-0449-y

Jawhar, N. M. T. (2009). Tissue Microarray: A rapidly evolving diagnostic and research tool. *Annals of Saudi Medicine*, *29*(2), 123–127. https://doi.org/10.4103/0256-4947.51806

Ji, H., Wang, Z., Perera, S. A., Li, D., Liang, M.-C., Zaghlul, S., McNamara, K., Chen, L., Albert, M., Sun, Y., Al-Hashem, R., Chirieac, L. R., Padera, R., Bronson, R. T., Thomas, R. K., Garraway, L. A., Jänne, P. A., Johnson, B. E., Chin, L., & Wong, K.-K. (2007). Mutations in BRAF and KRAS Converge on Activation of the Mitogen-Activated Protein Kinase Pathway in Lung Cancer Mouse Models. *Cancer Research*, *67*(10), Article 10. https://doi.org/10.1158/0008-5472.CAN-06-4592

Jiang, Q., Griffin, D. A., Barofsky, D. F., & Hurst, J. K. (1997). Intraphagosomal Chlorination Dynamics and Yields Determined Using Unique Fluorescent Bacterial Mimics. *Chemical Research in Toxicology*, *10*(10), 1080–1089. https://doi.org/10.1021/tx9700984

Jiang, S., Liu, H., & Li, C. (2021). Dietary Regulation of Oxidative Stress in Chronic Metabolic Diseases. *Foods*, *10*(8), Article 8. https://doi.org/10.3390/foods10081854

Kaiser, A. M., Gatto, A., Hanson, K. J., Zhao, R. L., Raj, N., Ozawa, M. G., Seoane, J. A., Bieging-Rolett, K. T., Wang, M., Li, I., Trope, W. L., Liou, D. Z., Shrager, J. B., Plevritis, S. K., Newman, A. M., Van Rechem, C., & Attardi, L. D. (2023). P53 governs an AT1 differentiation programme in lung cancer suppression. *Nature*, *619*(7971), 851–859. https://doi.org/10.1038/s41586-023-06253-8

Kealey, J., Düssmann, H., Llorente-Folch, I., Niewidok, N., Salvucci, M., Prehn, J. H. M., & D'Orsi, B. (2022). Effect of TP53 deficiency and KRAS signaling on the bioenergetics of colon cancer cells in response to different substrates: A single cell study. *Frontiers in Cell and Developmental Biology*, *10*, 893677. https://doi.org/10.3389/fcell.2022.893677

Keithley, E. M., Canto, C., Zheng, Q. Y., Wang, X., Fischel-Ghodsian, N., & Johnson, K. R. (2005). Cu/Zn superoxide dismutase and age-related hearing loss. *Hearing Research*, *209*(1), 76–85. https://doi.org/10.1016/j.heares.2005.06.009

Kennel, K. B., & Greten, F. R. (2021). Immune cell—Produced ROS and their impact on tumor growth and metastasis. *Redox Biology*, *42*, 101891. https://doi.org/10.1016/j.redox.2021.101891

Keskin, I., Forsgren, E., Lange, D. J., Weber, M., Birve, A., Synofzik, M., Gilthorpe, J. D., Andersen, P. M., & Marklund, S. L. (2016). Effects of Cellular Pathway Disturbances on Misfolded Superoxide Dismutase-1 in Fibroblasts Derived from ALS Patients. *PLOS ONE*, *11*(2), e0150133. https://doi.org/10.1371/journal.pone.0150133

Khalid, K., Apparow, S., Mushaddik, I. L., Anuar, A., Rizvi, S. A. A., & Habib, A. (2023). Effects of Ketogenic Diet on Reproductive Hormones in Women With Polycystic Ovary Syndrome. *Journal of the Endocrine Society*, *7*(10), bvad112. https://doi.org/10.1210/jendso/bvad112

Knaus, U. G. (2021). Oxidants in Physiological Processes. In H. H. H. W. Schmidt, P. Ghezzi, & A. Cuadrado (Eds.), *Reactive Oxygen Species: Network Pharmacology and Therapeutic Applications* (pp. 27–47). Springer International Publishing. https://doi.org/10.1007/164_2020_380

Knebel, A., Rahmsdorf, H. J., Ullrich, A., & Herrlich, P. (1996). Dephosphorylation of receptor tyrosine kinases as target of regulation by radiation, oxidants or alkylating agents. *The EMBO Journal*. https://www.embopress.org/doi/10.1002/j.1460-2075.1996.tb00916.x

Kobayashi, Y., Tata, A., Konkimalla, A., Katsura, H., Lee, R. F., Ou, J., Banovich, N. E., Kropski, J. A., & Tata, P. R. (2020). Persistence of a regeneration-associated, transitional alveolar epithelial cell state in pulmonary fibrosis. *Nature Cell Biology*, *22*(8), 934–946. https://doi.org/10.1038/s41556-020-0542-8

Kohan, R., Collin, A., Guizzardi, S., Tolosa de Talamoni, N., & Picotto, G. (2020). Reactive oxygen species in cancer: A paradox between pro- and anti-tumour activities. *Cancer Chemotherapy and Pharmacology*, *86*(1), 1–13. https://doi.org/10.1007/s00280-020-04103-2

Komaki, Y., Sugiura, H., Koarai, A., Tomaki, M., Ogawa, H., Akita, T., Hattori, T., & Ichinose, M. (2005). Cytokine-mediated xanthine oxidase upregulation in chronic obstructive pulmonary disease's airways. *Pulmonary Pharmacology & Therapeutics*, *18*(4), 297–302. https://doi.org/10.1016/j.pupt.2005.01.002

Kostrominova, T. Y. (2010). Advanced age-related denervation and fiber-type grouping in skeletal muscle of SOD1 knockout mice. *Free Radical Biology and Medicine*, *49*(10), 1582–1593. https://doi.org/10.1016/j.freeradbiomed.2010.08.022

Kotsafti, A., Scarpa, M., Castagliuolo, I., & Scarpa, M. (2020). Reactive Oxygen Species and Antitumor Immunity—From Surveillance to Evasion. *Cancers*, *12*(7), 1748. https://doi.org/10.3390/cancers12071748

Kuilman, T., Michaloglou, C., Vredeveld, L. C. W., Douma, S., Doorn, R. van, Desmet, C. J., Aarden, L. A., Mooi, W. J., & Peeper, D. S. (2008). Oncogene-Induced Senescence Relayed by an Interleukin-Dependent Inflammatory Network. *Cell*, *133*(6), 1019–1031. https://doi.org/10.1016/j.cell.2008.03.039

Kusano, T., Ehirchiou, D., Matsumura, T., Chobaz, V., Nasi, S., Castelblanco, M., So, A., Lavanchy, C., Acha-Orbea, H., Nishino, T., Okamoto, K., & Busso, N. (2019). Targeted knock-in mice expressing the oxidase-fixed form of xanthine oxidoreductase favor tumor growth. *Nature Communications*, *10*(1), 4904. https://doi.org/10.1038/s41467-019-12565-z

La Fleur, L., Falk-Sörqvist, E., Smeds, P., Berglund, A., Sundström, M., Mattsson, J. S., Brandén, E., Koyi, H., Isaksson, J., Brunnström, H., Nilsson, M., Micke, P., Moens, L., & Botling, J. (2019). Mutation patterns in a population-based non-small cell lung cancer cohort and prognostic impact of concomitant mutations in *KRAS* and *TP53* or *STK11*. *Lung Cancer*, *130*, 50–58. https://doi.org/10.1016/j.lungcan.2019.01.003

Lake, D., Corrêa, S. A. L., & Müller, J. (2016). Negative feedback regulation of the ERK1/2 MAPK pathway. *Cellular and Molecular Life Sciences*, *73*(23), Article 23. https://doi.org/10.1007/s00018-016-2297-8

Le Lay, S., Simard, G., Martinez, M. C., & Andriantsitohaina, R. (2014). Oxidative Stress and Metabolic Pathologies: From an Adipocentric Point of View. *Oxidative Medicine and Cellular Longevity*, *2014*(1), 908539. https://doi.org/10.1155/2014/908539

Lees, A., Sessler, T., & McDade, S. (2021). Dying to Survive—The p53 Paradox. *Cancers*, *13*(13), 3257. https://doi.org/10.3390/cancers13133257

Leonetti, A., Facchinetti, F., Rossi, G., Minari, R., Conti, A., Friboulet, L., Tiseo, M., & Planchard, D. (2018). BRAF in non-small cell lung cancer (NSCLC): Pickaxing another brick in the wall. *Cancer Treatment Reviews*, *66*, 82–94. https://doi.org/10.1016/j.ctrv.2018.04.006

Li, H., Yang, L., Wang, Y., Wang, L., Chen, G., Zhang, L., & Wang, D. (2023). Integrative analysis of TP53 mutations in lung adenocarcinoma for immunotherapies and prognosis. *BMC Bioinformatics*, *24*, 155. https://doi.org/10.1186/s12859-023-05268-2

Li, H., Zhang, Y., Xu, Y., Huang, Z., Cheng, G., Xie, M., Zhou, Z., Yu, Y., Xi, W., & Fan, Y. (2022). Tumor immune microenvironment and immunotherapy efficacy in BRAF mutation non-small-cell lung cancer. *Cell Death & Disease*, *13*(12), 1–10. https://doi.org/10.1038/s41419-022-05510-4

Li, J., Song, M., Moh, S., Kim, H., & Kim, D.-H. (2019). Cytoplasmic Restriction of Mutated SOD1 Impairs the DNA Repair Process in Spinal Cord Neurons. *Cells*, *8*(12), 1502. https://doi.org/10.3390/cells8121502

Li, X., Chen, Y., Zhao, J., Shi, J., Wang, M., Qiu, S., Hu, Y., Xu, Y., Cui, Y., Liu, C., & Liu, C. (2019). The Specific Inhibition of SOD1 Selectively Promotes Apoptosis of Cancer Cells via Regulation of the ROS Signaling Network. *Oxidative Medicine and Cellular Longevity*, *2019*, e9706792. https://doi.org/10.1155/2019/9706792

Liu, B., Chen, Y., & St. Clair, D. K. (2008). ROS and p53: Versatile partnership. *Free Radical Biology & Medicine*, *44*(8), Article 8. https://doi.org/10.1016/j.freeradbiomed.2008.01.011

Liu, S., Li, B., Xu, J., Hu, S., Zhan, N., Wang, H., Gao, C., Li, J., & Xu, X. (2020a). SOD1 Promotes Cell Proliferation and Metastasis in Non-small Cell Lung Cancer via an miR-409-3p/SOD1/SETDB1 Epigenetic Regulatory Feedforward Loop. *Frontiers in Cell and Developmental Biology*, *8*, 213. https://doi.org/10.3389/fcell.2020.00213

Liu, S., Li, B., Xu, J., Hu, S., Zhan, N., Wang, H., Gao, C., Li, J., & Xu, X. (2020b). SOD1 Promotes Cell Proliferation and Metastasis in Non-small Cell Lung Cancer via an miR-409-

3p/SOD1/SETDB1 Epigenetic Regulatory Feedforward Loop. *Frontiers in Cell and Developmental Biology*, *8*. https://doi.org/10.3389/fcell.2020.00213

Liu, S., Zhang, W., Zhang, L., Zou, H., Lu, K., Li, Q., Xia, H., Yan, S., & Ma, X. (2016). Genetic and functional analysis of two missense DUOX2 mutations in congenital hypothyroidism and goiter. *Oncotarget*, *9*(4), 4366–4374. https://doi.org/10.18632/oncotarget.10525

Liu, X., Davis, C. M., & Alkayed, N. J. (2018). P450 Eicosanoids and Reactive Oxygen Species Interplay in Brain Injury and Neuroprotection. *Antioxidants & Redox Signaling*, *28*(10), 987–1007. https://doi.org/10.1089/ars.2017.7056

Lobel, G. P., Jiang, Y., & Simon, M. C. (2023). Tumor microenvironmental nutrients, cellular responses, and cancer. *Cell Chemical Biology*, *30*(9), 1015–1032. https://doi.org/10.1016/j.chembiol.2023.08.011

Lobo, V., Patil, A., Phatak, A., & Chandra, N. (2010). Free radicals, antioxidants and functional foods: Impact on human health. *Pharmacognosy Reviews*, *4*(8), Article 8. https://doi.org/10.4103/0973-7847.70902

Locasale, J. W., & Cantley, L. C. (2011). Metabolic Flux and the Regulation of Mammalian Cell Growth. *Cell Metabolism*, *14*(4), 443–451. https://doi.org/10.1016/j.cmet.2011.07.014

Luchkova, A., Mata, A., & Cadenas, S. (2024). Nrf2 as a regulator of energy metabolism and mitochondrial function. *FEBS Letters*, *598*(17), 2092–2105. https://doi.org/10.1002/1873-3468.14993

Ludwig, D. S., Majzoub, J. A., Al-Zahrani, A., Dallal, G. E., Blanco, I., & Roberts, S. B. (1999). High Glycemic Index Foods, Overeating, and Obesity. *Pediatrics*, *103*(3), e26. https://doi.org/10.1542/peds.103.3.e26

Lynch, M., & Kuramitsu, H. (2000). Expression and role of superoxide dismutases (SOD) in pathogenic bacteria1. *Microbes and Infection*, *2*(10), 1245–1255. https://doi.org/10.1016/S1286-4579(00)01278-8

Mah, L.-J., El-Osta, A., & Karagiannis, T. C. (2010). γH2AX: A sensitive molecular marker of DNA damage and repair. *Leukemia*, *24*(4), 679–686. https://doi.org/10.1038/leu.2010.6

Marioli-Sapsakou, G.-K., & Kourti, M. (2021). Targeting Production of Reactive Oxygen Species as an Anticancer Strategy. *Anticancer Research*, *41*(12), 5881–5902. https://doi.org/10.21873/anticanres.15408

Martínez Leo, E. E., Peñafiel, A. M., Hernández Escalante, V. M., & Cabrera Araujo, Z. M. (2021). Ultra-processed diet, systemic oxidative stress, and breach of immunologic tolerance. *Nutrition*, *91–92*, 111419. https://doi.org/10.1016/j.nut.2021.111419

Martínez-Reyes, I., & Chandel, N. S. (2020). Mitochondrial TCA cycle metabolites control physiology and disease. *Nature Communications*, *11*(1), 102. https://doi.org/10.1038/s41467-019-13668-3

Martínez-Reyes, I., & Chandel, N. S. (2021). Cancer metabolism: Looking forward. *Nature Reviews Cancer*, *21*(10), Article 10. https://doi.org/10.1038/s41568-021-00378-6

Matzuk, M. M., Dionne, L., Guo, Q., Kumar, T. R., & Lebovitz, R. M. (1998). Ovarian Function in Superoxide Dismutase 1 and 2 Knockout Mice. *Endocrinology*, *139*(9), 4008–4011. https://doi.org/10.1210/endo.139.9.6289

McCubrey, J. A., Steelman, L. S., Chappell, W. H., Abrams, S. L., Wong, E. W. T., Chang, F., Lehmann, B., Terrian, D. M., Milella, M., Tafuri, A., Stivala, F., Libra, M., Basecke, J., Evangelisti, C., Martelli, A. M., & Franklin, R. A. (2007). Roles of the Raf/MEK/ERK pathway in cell growth, malignant transformation and drug resistance. *Biochimica et Biophysica Acta (BBA) - Molecular Cell Research*, *1773*(8), 1263–1284. https://doi.org/10.1016/j.bbamcr.2006.10.001

McFadden, S. L., Ding, D., Reaume, A. G., Flood, D. G., & Salvi, R. J. (1999). Age-related cochlear hair cell loss is enhanced in mice lacking copper/zinc superoxide dismutase. *Neurobiology of Aging*, *20*(1), 1–8. https://doi.org/10.1016/S0197-4580(99)00018-4

Miazek, K., Beton, K., Śliwińska, A., & Brożek-Płuska, B. (2022). The Effect of β-Carotene, Tocopherols and Ascorbic Acid as Anti-Oxidant Molecules on Human and Animal In

Vitro/In Vivo Studies: A Review of Research Design and Analytical Techniques Used. *Biomolecules*, *12*(8), Article 8. https://doi.org/10.3390/biom12081087

Milani, P., Gagliardi, S., Cova, E., & Cereda, C. (2011). SOD1 Transcriptional and Posttranscriptional Regulation and Its Potential Implications in ALS. *Neurology Research International*, *2011*, 458427. https://doi.org/10.1155/2011/458427

Mitra, A., & Mandal, A. K. (2018). Conjugation of para-benzoquinone of Cigarette Smoke with Human Hemoglobin Leads to Unstable Tetramer and Reduced Cooperative Oxygen Binding. *Journal of the American Society for Mass Spectrometry*, *29*(10), 2048–2058. https://doi.org/10.1007/s13361-018-2011-1

Moldovan, L., Irani, K., Moldovan, N. I., Finkel, T., & Goldschmidt-Clermont, P. J. (1999). The Actin Cytoskeleton Reorganization Induced by Rac1 Requires the Production of Superoxide. *Antioxidants & Redox Signaling*, *1*(1), 29–43. https://doi.org/10.1089/ars.1999.1.1-29

Molina, J. R., Yang, P., Cassivi, S. D., Schild, S. E., & Adjei, A. A. (2008). Non–Small Cell Lung Cancer: Epidemiology, Risk Factors, Treatment, and Survivorship. *Mayo Clinic Proceedings. Mayo Clinic*, *83*(5), Article 5.

Montllor-Albalate, C., Colin, A. E., Chandrasekharan, B., Bolaji, N., Andersen, J. L., Wayne Outten, F., & Reddi, A. R. (2019). Extra-mitochondrial Cu/Zn superoxide dismutase (Sod1) is dispensable for protection against oxidative stress but mediates peroxide signaling in *Saccharomyces cerevisiae*. *Redox Biology*, *21*, 101064. https://doi.org/10.1016/j.redox.2018.11.022

Morikawa, D., Nojiri, H., Saita, Y., Kobayashi, K., Watanabe, K., Ozawa, Y., Koike, M., Asou, Y., Takaku, T., Kaneko, K., & Shimizu, T. (2013). Cytoplasmic reactive oxygen species and SOD1 regulate bone mass during mechanical unloading. *Journal of Bone and Mineral Research*, *28*(11), 2368–2380. https://doi.org/10.1002/jbmr.1981

Motataianu, A., Serban, G., Barcutean, L., & Balasa, R. (2022). Oxidative Stress in Amyotrophic Lateral Sclerosis: Synergy of Genetic and Environmental Factors. *International Journal of Molecular Sciences*, *23*(16), 9339. https://doi.org/10.3390/ijms23169339

Murakami, K., Inagaki, J., Saito, M., Ikeda, Y., Tsuda, C., Noda, Y., Kawakami, S., Shirasawa, T., & Shimizu, T. (2009). Skin atrophy in cytoplasmic SOD-deficient mice and its complete recovery using a vitamin C derivative. *Biochemical and Biophysical Research Communications*, *382*(2), 457–461. https://doi.org/10.1016/j.bbrc.2009.03.053

Murray, P. J. (2017). Macrophage Polarization. *Annual Review of Physiology*, *79*(Volume 79, 2017), 541–566. https://doi.org/10.1146/annurev-physiol-022516-034339

Muscogiuri, G., Salmon, A. B., Aguayo-Mazzucato, C., Li, M., Balas, B., Guardado-Mendoza, R., Giaccari, A., Reddick, R. L., Reyna, S. M., Weir, G., DeFronzo, R. A., Van Remmen, H., & Musi, N. (2013). Genetic Disruption of SOD1 Gene Causes Glucose Intolerance and Impairs β-Cell Function. *Diabetes*, *62*(12), 4201–4207. https://doi.org/10.2337/db13-0314

Nègre-Salvayre, A., Garoby-Salom, S., Swiader, A., Rouahi, M., Pucelle, M., & Salvayre, R. (2017). Proatherogenic effects of 4-hydroxynonenal. *Free Radical Biology and Medicine*, *111*, 127–139. https://doi.org/10.1016/j.freeradbiomed.2016.12.038

Noblanc, A., Klaassen, A., & Robaire, B. (2020). The Exacerbation of Aging and Oxidative Stress in the Epididymis of Sod1 Null Mice. *Antioxidants*, *9*(2), Article 2. https://doi.org/10.3390/antiox9020151

Node, K., Kitakaze, M., Yoshikawa, H., Kosaka, H., & Hori, M. (1997). Reduced plasma concentrations of nitrogen oxide in individuals with essential hypertension. *Hypertension (Dallas, Tex.: 1979)*, *30*(3 Pt 1), 405–408. https://doi.org/10.1161/01.hyp.30.3.405

Noguera-Troise, I., Daly, C., Papadopoulos, N. J., Coetzee, S., Boland, P., Gale, N. W., Chieh Lin, H., Yancopoulos, G. D., & Thurston, G. (2006). Blockade of Dll4 inhibits tumour growth by promoting non-productive angiogenesis. *Nature*, *444*(7122), 1032–1037. https://doi.org/10.1038/nature05355

Nolfi-Donegan, D., Braganza, A., & Shiva, S. (2020). Mitochondrial electron transport chain: Oxidative phosphorylation, oxidant production, and methods of measurement. *Redox Biology*, *37*, 101674. https://doi.org/10.1016/j.redox.2020.101674

O'Hearn, M., Lauren, B. N., Wong, J. B., Kim, D. D., & Mozaffarian, D. (2022). Trends and Disparities in Cardiometabolic Health Among U.S. Adults, 1999-2018. *Journal of the American College of Cardiology*, *80*(2), 138–151. https://doi.org/10.1016/j.jacc.2022.04.046

Osta, B. E., Behera, M., Kim, S., Berry, L. D., Sica, G., Pillai, R. N., Owonikoko, T. K., Kris, M. G., Johnson, B. E., Kwiatkowski, D. J., Sholl, L. M., Aisner, D. L., Bunn, P. A., Khuri, F. R., & Ramalingam, S. S. (2019). Characteristics and Outcomes of Patients With Metastatic KRAS-Mutant Lung Adenocarcinomas: The Lung Cancer Mutation Consortium Experience. *Journal of Thoracic Oncology*, *14*(5), 876–889. https://doi.org/10.1016/j.jtho.2019.01.020

Palma, F. R., He, C., Danes, J. M., Paviani, V., Coelho, D. R., Gantner, B. N., & Bonini, M. G. (2020). Mitochondrial Superoxide Dismutase: What the Established, the Intriguing, and the Novel Reveal About a Key Cellular Redox Switch. *Antioxidants & Redox Signaling*, *32*(10), 701–714. https://doi.org/10.1089/ars.2019.7962

Papa, L., Hahn, M., Marsh, E. L., Evans, B. S., & Germain, D. (2014). SOD2 to SOD1 Switch in Breast Cancer *. *Journal of Biological Chemistry*, *289*(9), 5412–5416. https://doi.org/10.1074/jbc.C113.526475

Papa, L., Manfredi, G., & Germain, D. (2014). SOD1, an unexpected novel target for cancer therapy. *Genes & Cancer*, *5*(1–2), Article 1–2.

Pardo, C. A., Xu, Z., Borchelt, D. R., Price, D. L., Sisodia, S. S., & Cleveland, D. W. (1995). Superoxide dismutase is an abundant component in cell bodies, dendrites, and axons of motor neurons and in a subset of other neurons. *Proceedings of the National Academy of Sciences*, *92*(4), 954–958. https://doi.org/10.1073/pnas.92.4.954

Park, H. R., & Yang, E. J. (2021). Oxidative Stress as a Therapeutic Target in Amyotrophic Lateral Sclerosis: Opportunities and Limitations. *Diagnostics*, *11*(9), Article 9. https://doi.org/10.3390/diagnostics11091546

Peng, H.-Y., Lucavs, J., Ballard, D., Das, J. K., Kumar, A., Wang, L., Ren, Y., Xiong, X., & Song, J. (2021). Metabolic Reprogramming and Reactive Oxygen Species in T Cell

Immunity. *Frontiers in Immunology*, *12*, 652687. https://doi.org/10.3389/fimmu.2021.652687

Petti, C., Molla, A., Vegetti, C., Ferrone, S., Anichini, A., & Sensi, M. (2006). Coexpression of NRASQ61R and BRAFV600E in Human Melanoma Cells Activates Senescence and Increases Susceptibility to Cell-Mediated Cytotoxicity. *Cancer Research*, *66*(13), 6503–6511. https://doi.org/10.1158/0008-5472.CAN-05-4671

Pitolli, C., Wang, Y., Candi, E., Shi, Y., Melino, G., & Amelio, I. (2019). p53-Mediated Tumor Suppression: DNA-Damage Response and Alternative Mechanisms. *Cancers*, *11*(12), 1983. https://doi.org/10.3390/cancers11121983

Rani, V., Deep, G., Singh, R. K., Palle, K., & Yadav, U. C. S. (2016). Oxidative stress and metabolic disorders: Pathogenesis and therapeutic strategies. *Life Sciences*, *148*, 183–193. https://doi.org/10.1016/j.lfs.2016.02.002

Rathaus, M., & Bernheim, J. (2002). Oxygen species in the microvascular environment: Regulation of vascular tone and the development of hypertension. *Nephrology, Dialysis, Transplantation: Official Publication of the European Dialysis and Transplant Association - European Renal Association*, *17*(2), 216–221. https://doi.org/10.1093/ndt/17.2.216

Reddi, A. R., & Culotta, V. C. (2013). SOD1 Integrates Signals from Oxygen and Glucose to Repress Respiration. *Cell*, *152*(1), Article 1. https://doi.org/10.1016/j.cell.2012.11.046

Rodgman, A., & Perfetti, T. A. (2008). *The Chemical Components of Tobacco and Tobacco Smoke*. CRC Press. https://doi.org/10.1201/9781420078848

Rodríguez, A. G., Rodríguez, J. Z., Barreto, A., Sanabria-Barrera, S., Iglesias, J., & Morales, L. (2023). Impact of Acute High Glucose on Mitochondrial Function in a Model of Endothelial Cells: Role of PDGF-C. *International Journal of Molecular Sciences*, *24*(5), 4394. https://doi.org/10.3390/ijms24054394

Sablina, A. A., Budanov, A. V., Ilyinskaya, G. V., Agapova, L. S., Kravchenko, J. E., & Chumakov, P. M. (2005). The antioxidant function of the p53 tumor suppressor. *Nature Medicine*, *11*(12), 1306–1313. https://doi.org/10.1038/nm1320

Sahin, I. H., & Klostergaard, J. (2021). BRAF Mutations as Actionable Targets: A Paradigm Shift in the Management of Colorectal Cancer and Novel Avenues. *JCO Oncology Practice*, *17*(12), 723–730. https://doi.org/10.1200/OP.21.00160

Salmeen, A., Park, B. O., & Meyer, T. (2010). The NADPH oxidases NOX4 and DUOX2 regulate cell cycle entry via a p53-dependent pathway. *Oncogene*, *29*(31), 4473–4484. https://doi.org/10.1038/onc.2010.200

Sarnyai, Z., & Palmer, C. M. (2020). Ketogenic Therapy in Serious Mental Illness: Emerging Evidence. *International Journal of Neuropsychopharmacology*, *23*(7), 434–439. https://doi.org/10.1093/ijnp/pyaa036

Selvaratnam, J. S., & Robaire, B. (2016). Effects of Aging and Oxidative Stress on Spermatozoa of Superoxide-Dismutase 1- and Catalase-Null Mice1. *Biology of Reproduction*, *95*(3), 60, 1–13. https://doi.org/10.1095/biolreprod.116.141671

Semenza, G. L. (2020). The Genomics and Genetics of Oxygen Homeostasis. *Annual Review of Genomics and Human Genetics*, *21*(Volume 21, 2020), 183–204. https://doi.org/10.1146/annurev-genom-111119-073356

Sensi, M., Nicolini, G., Petti, C., Bersani, I., Lozupone, F., Molla, A., Vegetti, C., Nonaka, D., Mortarini, R., Parmiani, G., Fais, S., & Anichini, A. (2006). Mutually exclusive NRASQ61R and BRAFV600E mutations at the single-cell level in the same human melanoma. *Oncogene*, *25*(24), 3357–3364. https://doi.org/10.1038/sj.onc.1209379

Seo, Y. R., Kelley, M. R., & Smith, M. L. (2002). Selenomethionine regulation of p53 by a ref1-dependent redox mechanism. *Proceedings of the National Academy of Sciences*, *99*(22), 14548–14553. https://doi.org/10.1073/pnas.212319799

Sethi, S., Wakeham, D., Ketter, T., Hooshmand, F., Bjornstad, J., Richards, B., Westman, E., Krauss, R. M., & Saslow, L. (2024). Ketogenic Diet Intervention on Metabolic and Psychiatric Health in Bipolar and Schizophrenia: A Pilot Trial. *Psychiatry Research*, *335*, 115866. https://doi.org/10.1016/j.psychres.2024.115866

Shah, M. A., & Rogoff, H. A. (2021). Implications of reactive oxygen species on cancer formation and its treatment. *Seminars in Oncology*, *48*(3), 238–245. https://doi.org/10.1053/j.seminoncol.2021.05.002

Shai, A., Dankort, D., Juan, J., Green, S., & McMahon, M. (2015). TP53 Silencing Bypasses Growth Arrest of BRAFV600E-Induced Lung Tumor Cells in a Two-Switch Model of Lung Tumorigenesis. *Cancer Research*, *75*(15), 3167–3180. https://doi.org/10.1158/0008-5472.CAN-14-3701

Sheng, K.-C., Pietersz, G. A., Tang, C. K., Ramsland, P. A., & Apostolopoulos, V. (2010). Reactive oxygen species level defines two functionally distinctive stages of inflammatory dendritic cell development from mouse bone marrow. *Journal of Immunology (Baltimore, Md.: 1950)*, *184*(6), 2863–2872. https://doi.org/10.4049/jimmunol.0903458

Shi, T., & Dansen, T. B. (2020). Reactive Oxygen Species Induced p53 Activation: DNA Damage, Redox Signaling, or Both? *Antioxidants & Redox Signaling*, *33*(12), 839–859. https://doi.org/10.1089/ars.2020.8074

Shibuya, S., Watanabe, K., Ozawa, Y., & Shimizu, T. (2021). Xanthine Oxidoreductase-Mediated Superoxide Production Is Not Involved in the Age-Related Pathologies in Sod1-Deficient Mice. *International Journal of Molecular Sciences*, *22*(7), Article 7. https://doi.org/10.3390/ijms22073542

Shu, P., Liang, H., Zhang, J., Lin, Y., Chen, W., & Zhang, D. (2023). Reactive oxygen species formation and its effect on CD4+ T cell-mediated inflammation. *Frontiers in Immunology*, *14*. https://doi.org/10.3389/fimmu.2023.1199233

Simon, N. G., Turner, M. R., Vucic, S., Al-Chalabi, A., Shefner, J., Lomen-Hoerth, C., & Kiernan, M. C. (2014). Quantifying Disease Progression in Amyotrophic Lateral Sclerosis. *Annals of Neurology*, *76*(5), 643–657. https://doi.org/10.1002/ana.24273

Siraki, A. G., Chan, T. S., & O'Brien, P. J. (2004). Application of Quantitative Structure-Toxicity Relationships for the Comparison of the Cytotoxicity of 14 p-Benzoquinone

Congeners in Primary Cultured Rat Hepatocytes Versus PC12 Cells. *Toxicological Sciences*, *81*(1), 148–159. https://doi.org/10.1093/toxsci/kfh182

Skulachev, V. P. (1996). Role of uncoupled and non-coupled oxidations in maintenance of safely low levels of oxygen and its one-electron reductants. *Quarterly Reviews of Biophysics*, *29*(2), 169–202. https://doi.org/10.1017/S0033583500005795

Śmiech, M., Leszczyński, P., Kono, H., Wardell, C., & Taniguchi, H. (2020). Emerging BRAF Mutations in Cancer Progression and Their Possible Effects on Transcriptional Networks. *Genes*, *11*(11), Article 11. https://doi.org/10.3390/genes11111342

Somwar, R., Erdjument-Bromage, H., Larsson, E., Shum, D., Lockwood, W. W., Yang, G., Sander, C., Ouerfelli, O., Tempst, P. J., Djaballah, H., & Varmus, H. E. (2011). Superoxide dismutase 1 (SOD1) is a target for a small molecule identified in a screen for inhibitors of the growth of lung adenocarcinoma cell lines. *Proceedings of the National Academy of Sciences*, *108*(39), Article 39. https://doi.org/10.1073/pnas.1113554108

Starkov, A. A. (1997). "Mild" Uncoupling of Mitochondria. *Bioscience Reports*, *17*(3), 273–279. https://doi.org/10.1023/A:1027380527769

Sturtz, L. A., Diekert, K., Jensen, L. T., Lill, R., & Culotta, V. C. (2001). A Fraction of Yeast Cu,Zn-Superoxide Dismutase and Its Metallochaperone, CCS, Localize to the Intermembrane Space of Mitochondria: A PHYSIOLOGICAL ROLE FOR SOD1 IN GUARDING AGAINST MITOCHONDRIAL OXIDATIVE DAMAGE *. *Journal of Biological Chemistry*, *276*(41), 38084–38089. https://doi.org/10.1074/jbc.M105296200

Sullivan, L. B., & Chandel, N. (2014). Mitochondrial metabolism in TCA cycle mutant cancer cells. *Cell Cycle*, *13*(3), 347–348. https://doi.org/10.4161/cc.27513

Sundaresan, M., Yu, Z.-X., Ferrans, V. J., Irani, K., & Finkel, T. (1995). Requirement for Generation of H2O2 for Platelet-Derived Growth Factor Signal Transduction. *Science*, *270*(5234), Article 5234. https://doi.org/10.1126/science.270.5234.296

Tang, Y., Pu, X., Yuan, X., Pang, Z., Li, F., & Wang, X. (2024). Targeting KRASG12D mutation in non-small cell lung cancer: Molecular mechanisms and therapeutic potential. *Cancer Gene Therapy*, *31*(7), 961–969. https://doi.org/10.1038/s41417-024-00778-4

Tao, S., Wang, S., Moghaddam, S. J., Ooi, A., Chapman, E., Wong, P. K., & Zhang, D. D. (2014). Oncogenic KRAS confers chemoresistance by upregulating NRF2. *Cancer Research*, *74*(24), 7430–7441. https://doi.org/10.1158/0008-5472.CAN-14-1439

Thomas, D. C. (2017). The phagocyte respiratory burst: Historical perspectives and recent advances. *Immunology Letters*, *192*, 88–96. https://doi.org/10.1016/j.imlet.2017.08.016

Trist, B. G., Hilton, J. B., Hare, D. J., Crouch, P. J., & Double, K. L. (2021). Superoxide Dismutase 1 in Health and Disease: How a Frontline Antioxidant Becomes Neurotoxic. *Angewandte Chemie International Edition*, *60*(17), 9215–9246. https://doi.org/10.1002/anie.202000451

Truett, G. e., Heeger, P., Mynatt, R. l., Truett, A. a., Walker, J. a., & Warman, M. l. (2000). Preparation of PCR-Quality Mouse Genomic DNA with Hot Sodium Hydroxide and Tris (HotSHOT). *BioTechniques*, *29*(1), 52–54. https://doi.org/10.2144/00291bm09

Tsang, C. K., Chen, M., Cheng, X., Qi, Y., Chen, Y., Das, I., Li, X., Vallat, B., Fu, L.-W., Qian, C.-N., Wang, H.-Y., White, E., Burley, S. K., & Zheng, X. F. S. (2018). SOD1 Phosphorylation by mTORC1 Couples Nutrient Sensing and Redox Regulation. *Molecular Cell*, *70*(3), Article 3. https://doi.org/10.1016/j.molcel.2018.03.029

Tsang, C. K., Liu, Y., Thomas, J., Zhang, Y., & Zheng, X. F. S. (2014). Superoxide dismutase 1 acts as a nuclear transcription factor to regulate oxidative stress resistance. *Nature Communications*, *5*(1), 3446. https://doi.org/10.1038/ncomms4446

Tsushima, Y., Nachawi, N., Pantalone, K. M., Griebeler, M. L., & Alwahab, U. A. (2024). Ketogenic diet improves fertility in patients with polycystic ovary syndrome: A brief report. *Frontiers in Nutrition*, *11*. https://doi.org/10.3389/fnut.2024.1395977

Unni, A. M., Lockwood, W. W., Zejnullahu, K., Lee-Lin, S.-Q., & Varmus, H. (2015). Evidence that synthetic lethality underlies the mutual exclusivity of oncogenic KRAS and EGFR mutations in lung adenocarcinoma. *eLife*, *4*, e06907. https://doi.org/10.7554/eLife.06907

Valavanidis, A., Vlachogianni, T., & Fiotakis, C. (2009). 8-hydroxy-2′ -deoxyguanosine (8-OHdG): A Critical Biomarker of Oxidative Stress and Carcinogenesis. *Journal of Environmental Science and Health, Part C*, *27*(2), 120–139. https://doi.org/10.1080/10590500902885684

Valencia, A., & Kochevar, I. E. (2008). Nox1-Based NADPH Oxidase Is the Major Source of UVA-Induced Reactive Oxygen Species in Human Keratinocytes. *Journal of Investigative Dermatology*, *128*(1), 214–222. https://doi.org/10.1038/sj.jid.5700960

Vaziri-Gohar, A., Cassel, J., Mohammed, F. S., Zarei, M., Hue, J. J., Hajihassani, O., Graor, H. J., Srikanth, Y. V. V., Karim, S. A., Abbas, A., Prendergast, E., Chen, V., Katayama, E. S., Dukleska, K., Khokhar, I., Andren, A., Zhang, L., Wu, C., Erokwu, B., … Winter, J. M. (2022). Limited nutrient availability in the tumor microenvironment renders pancreatic tumors sensitive to allosteric IDH1 inhibitors. *Nature Cancer*, *3*(7), 852–865. https://doi.org/10.1038/s43018-022-00393-y

Wahl, S. G. F., Dai, H. Y., Emdal, E. F., Berg, T., Halvorsen, T. O., Ottestad, A. L., Lund-Iversen, M., Brustugun, O. T., Førde, D., Paulsen, E.-E., Donnem, T., Andersen, S., Grønberg, B. H., & Richardsen, E. (2021). The Prognostic Effect of KRAS Mutations in Non-Small Cell Lung Carcinoma Revisited: A Norwegian Multicentre Study. *Cancers*, *13*(17), 4294. https://doi.org/10.3390/cancers13174294

Wang, W., Liu, H., & Li, G. (2022). What's the difference between lung adenocarcinoma and lung squamous cell carcinoma? Evidence from a retrospective analysis in a cohort of Chinese patients. *Frontiers in Endocrinology*, *13*. https://www.frontiersin.org/articles/10.3389/fendo.2022.947443

Wang, X., Zhang, H., Sapio, R., Yang, J., Wong, J., Zhang, X., Guo, J. Y., Pine, S., Van Remmen, H., Li, H., White, E., Liu, C., Kiledjian, M., Pestov, D. G., & Steven Zheng, X. F.

(2021). SOD1 regulates ribosome biogenesis in KRAS mutant non-small cell lung cancer. *Nature Communications*, *12*(1), Article 1. https://doi.org/10.1038/s41467-021-22480-x

Wang, Y., Qi, H., Liu, Y., Duan, C., Liu, X., Xia, T., Chen, D., Piao, H., & Liu, H.-X. (2021). The double-edged roles of ROS in cancer prevention and therapy. *Theranostics*, *11*(10), 4839–4857. https://doi.org/10.7150/thno.56747

Warburg, O., Wind, F., & Negelein, E. (1927). THE METABOLISM OF TUMORS IN THE BODY. *The Journal of General Physiology*, *8*(6), 519–530.

Watanabe, K., Shibuya, S., Koyama, H., Ozawa, Y., Toda, T., Yokote, K., & Shimizu, T. (2013). Sod1 Loss Induces Intrinsic Superoxide Accumulation Leading to p53-Mediated Growth Arrest and Apoptosis. *International Journal of Molecular Sciences*, *14*(6), 10998–11010. https://doi.org/10.3390/ijms140610998

Watanabe, K., Shibuya, S., Ozawa, Y., Toda, T., & Shimizu, T. (2021). Pathological Relationship between Intracellular Superoxide Metabolism and p53 Signaling in Mice. *International Journal of Molecular Sciences*, *22*(7), Article 7. https://doi.org/10.3390/ijms22073548

Wei, Y., Jia, S., Ding, Y., Xia, S., & Giunta, S. (2023). Balanced basal-levels of ROS (redox-biology), and very-low-levels of pro-inflammatory cytokines (cold-inflammaging), as signaling molecules can prevent or slow-down overt-inflammaging, and the aging-associated decline of adaptive-homeostasis. *Experimental Gerontology*, *172*, 112067. https://doi.org/10.1016/j.exger.2022.112067

Weinberg, F., Ramnath, N., & Nagrath, D. (2019). Reactive Oxygen Species in the Tumor Microenvironment: An Overview. *Cancers*, *11*(8), 1191. https://doi.org/10.3390/cancers11081191

Whitley, M. J., Tran, T. H., Rigby, M., Yi, M., Dharmaiah, S., Waybright, T. J., Ramakrishnan, N., Perkins, S., Taylor, T., Messing, S., Esposito, D., Nissley, D. V., McCormick, F., Stephen, A. G., Turbyville, T., Cornilescu, G., & Simanshu, D. K. (2024). Comparative

analysis of KRAS4a and KRAS4b splice variants reveals distinctive structural and functional properties. *Science Advances*, *10*(7), eadj4137. https://doi.org/10.1126/sciadv.adj4137

Williamson, T. L., & Cleveland, D. W. (1999). Slowing of axonal transport is a very early event in the toxicity of ALS–linked SOD1 mutants to motor neurons. *Nature Neuroscience*, *2*(1), 50–56. https://doi.org/10.1038/4553

Woo, H. A., Yim, S. H., Shin, D. H., Kang, D., Yu, D.-Y., & Rhee, S. G. (2010). Inactivation of Peroxiredoxin I by Phosphorylation Allows Localized H2O2 Accumulation for Cell Signaling. *Cell*, *140*(4), 517–528. https://doi.org/10.1016/j.cell.2010.01.009

Wright, R. M., Ginger, L. A., Kosila, N., Elkins, N. D., Essary, B., McManaman, J. L., & Repine, J. E. (2004). Mononuclear Phagocyte Xanthine Oxidoreductase Contributes to Cytokine-Induced Acute Lung Injury. *American Journal of Respiratory Cell and Molecular Biology*, *30*(4), 479–490. https://doi.org/10.1165/rcmb.2003-0309OC

Xiang, H., Ramil, C. P., Hai, J., Zhang, C., Wang, H., Watkins, A. A., Afshar, R., Georgiev, P., Sze, M. A., Song, X. S., Curran, P. J., Cheng, M., Miller, J. R., Sun, D., Loboda, A., Jia, Y., Moy, L. Y., Chi, A., & Brandish, P. E. (2020). Cancer-Associated Fibroblasts Promote Immunosuppression by Inducing ROS-Generating Monocytic MDSCs in Lung Squamous Cell Carcinoma. *Cancer Immunology Research*, *8*(4), 436–450. https://doi.org/10.1158/2326-6066.CIR-19-0507

Xie, M., Xu, X., & Fan, Y. (2021). KRAS-Mutant Non-Small Cell Lung Cancer: An Emerging Promisingly Treatable Subgroup. *Frontiers in Oncology*, *11*. https://www.frontiersin.org/articles/10.3389/fonc.2021.672612

Xu, J., Su, X., Burley, S. K., & Zheng, X. F. S. (2022). Nuclear SOD1 in Growth Control, Oxidative Stress Response, Amyotrophic Lateral Sclerosis, and Cancer. *Antioxidants*, *11*(2), Article 2. https://doi.org/10.3390/antiox11020427

Yang, H., Villani, R. M., Wang, H., Simpson, M. J., Roberts, M. S., Tang, M., & Liang, X. (2018). The role of cellular reactive oxygen species in cancer chemotherapy. *Journal of*

Experimental & Clinical Cancer Research, *37*(1), 266. https://doi.org/10.1186/s13046-018-0909-x

Yarosz, E. L., & Chang, C.-H. (2018). The Role of Reactive Oxygen Species in Regulating T Cell-mediated Immunity and Disease. *Immune Network*, *18*(1), e14. https://doi.org/10.4110/in.2018.18.e14

Yu, Y., Liu, S., Yang, L., Song, P., Liu, Z., Liu, X., Yan, X., & Dong, Q. (2024). Roles of reactive oxygen species in inflammation and cancer. *MedComm*, *5*(4), e519. https://doi.org/10.1002/mco2.519

Zarkovic, K., Jakovcevic, A., & Zarkovic, N. (2017). Contribution of the HNE-immunohistochemistry to modern pathological concepts of major human diseases. *Free Radical Biology and Medicine*, *111*, 110–126. https://doi.org/10.1016/j.freeradbiomed.2016.12.009

Zelko, I. N., Mariani, T. J., & Folz, R. J. (2002). Superoxide dismutase multigene family: A comparison of the CuZn-SOD (SOD1), Mn-SOD (SOD2), and EC-SOD (SOD3) gene structures, evolution, and expression. *Free Radical Biology and Medicine*, *33*(3), 337–349. https://doi.org/10.1016/S0891-5849(02)00905-X

Zhang, C., Wang, X., Du, J., Gu, Z., & Zhao, Y. (2021). Reactive Oxygen Species-Regulating Strategies Based on Nanomaterials for Disease Treatment. *Advanced Science*, *8*(3), 2002797. https://doi.org/10.1002/advs.202002797

Zhang, H., Wang, L., & Chu, Y. (2019). Reactive oxygen species: The signal regulator of B cell. *Free Radical Biology and Medicine*, *142*, 16–22. https://doi.org/10.1016/j.freeradbiomed.2019.06.004

Zhang, Y., Choksi, S., Chen, K., Pobezinskaya, Y., Linnoila, I., & Liu, Z.-G. (2013). ROS play a critical role in the differentiation of alternatively activated macrophages and the occurrence of tumor-associated macrophages. *Cell Research*, *23*(7), 898–914. https://doi.org/10.1038/cr.2013.75

Zhang, Y., Ikeno, Y., Bokov, A., Gelfond, J., Jaramillo, C., Zhang, H.-M., Liu, Y., Qi, W., Hubbard, G., Richardson, A., & Van Remmen, H. (2013). Dietary restriction attenuates the accelerated aging phenotype of *Sod1−/−* mice. *Free Radical Biology and Medicine*, *60*, 300–306. https://doi.org/10.1016/j.freeradbiomed.2013.02.026

Zhang, Y., Unnikrishnan, A., Deepa, S. S., Liu, Y., Li, Y., Ikeno, Y., Sosnowska, D., Van Remmen, H., & Richardson, A. (2017). A new role for oxidative stress in aging: The accelerated aging phenotype in *Sod1−/−* mice is correlated to increased cellular senescence. *Redox Biology*, *11*, 30–37. https://doi.org/10.1016/j.redox.2016.10.014

Zhang, Y., Yan, W., Collins, M. A., Bednar, F., Rakshit, S., Zetter, B. R., Stanger, B. Z., Chung, I., Rhim, A. D., & di Magliano, M. P. (2013). Interleukin-6 Is Required for Pancreatic Cancer Progression by Promoting MAPK Signaling Activation and Oxidative Stress Resistance. *Cancer Research*, *73*(20), 6359–6374. https://doi.org/10.1158/0008-5472.CAN-13-1558-T

Zhao, R.-Z., Jiang, S., Zhang, L., & Yu, Z.-B. (2019). Mitochondrial electron transport chain, ROS generation and uncoupling (Review). *International Journal of Molecular Medicine*, *44*(1), 3–15. https://doi.org/10.3892/ijmm.2019.4188

Zhong, Y., Wang, J., Henderson, M. J., Yang, P., Hagen, B. M., Siddique, T., Vogel, B. E., Deng, H.-X., & Fang, S. (2017). Nuclear export of misfolded SOD1 mediated by a normally buried NES-like sequence reduces proteotoxicity in the nucleus. *eLife*, *6*, e23759. https://doi.org/10.7554/eLife.23759

Zhou, D., Duan, Z., Li, Z., Ge, F., Wei, R., & Kong, L. (2022). The significance of glycolysis in tumor progression and its relationship with the tumor microenvironment. *Frontiers in Pharmacology*, *13*, 1091779. https://doi.org/10.3389/fphar.2022.1091779

Zimna, A., & Kurpisz, M. (2015). Hypoxia-Inducible Factor-1 in Physiological and Pathophysiological Angiogenesis: Applications and Therapies. *BioMed Research International*, *2015*, 549412. https://doi.org/10.1155/2015/549412

Zong, W.-X., Rabinowitz, J. D., & White, E. (2016). Mitochondria and Cancer. *Molecular Cell*, *61*(5), 667–676. https://doi.org/10.1016/j.molcel.2016.02.011

Zong, Y., Li, H., Liao, P., Chen, L., Pan, Y., Zheng, Y., Zhang, C., Liu, D., Zheng, M., & Gao, J. (2024). Mitochondrial dysfunction: Mechanisms and advances in therapy. *Signal Transduction and Targeted Therapy*, *9*(1), 1–29. https://doi.org/10.1038/s41392-024-01839-8

Zorova, L. D., Popkov, V. A., Plotnikov, E. Y., Silachev, D. N., Pevzner, I. B., Jankauskas, S. S., Babenko, V. A., Zorov, S. D., Balakireva, A. V., Juhaszova, M., Sollott, S. J., & Zorov, D. B. (2018). Mitochondrial membrane potential. *Analytical Biochemistry*, *552*, 50–59. https://doi.org/10.1016/j.ab.2017.07.009